Materials Today Bio 13 (2022) 100197

Contents lists available at ScienceDirect

Materials Today Bio

journal homepage: www.journals.elsevier.com/materials-today-bio

# Recent advances in multifunctional nanomaterials for photothermal-enhanced Fenton-based chemodynamic tumor therapy

Panchanathan Manivasagan [a,b], Ara Joe [b], Hyo-Won Han [b], Thavasyappan Thambi [c], Manickam Selvaraj [d], Kumarappan Chidambaram [e], Jungbae Kim [a,f,**], Eue-Soon Jang [b,*]

[a] Department of Chemical and Biological Engineering and R&E Center for Chemical and Biological Engineering (BK21 FOUR), Korea University, Seoul, 02841, Republic of Korea
[b] Department of Applied Chemistry, Kumoh National Institute of Technology, Daehak-ro 61, Gumi, Gyeongbuk, 39177, Republic of Korea
[c] School of Chemical Engineering, Theranostic Macromolecules Research Center, Sungkyunkwan University, Suwon, 16419, Republic of Korea
[d] Department of Chemistry, Faculty of Science, King Khalid University, Abha, 61413, Saudi Arabia
[e] Department of Pharmacology & Toxicology, School of Pharmacy, King Khalid University, Abha, 62529, Saudi Arabia
[f] Department of Chemical and Biological Engineering, Korea University, Seoul, 02841, Republic of Korea

ARTICLE INFO

*Keywords:*
Nanomaterials
Fenton reaction
Chemodynamic therapy
Photothermal therapy
Combination therapy

ABSTRACT

Photothermal (PT)-enhanced Fenton-based chemodynamic therapy (CDT) has attracted a significant amount of research attention over the last five years as a highly effective, safe, and tumor-specific nanomedicine-based therapy. CDT is a new emerging nanocatalyst-based therapeutic strategy for the *in situ* treatment of tumors via the Fenton reaction or Fenton-like reaction, which has got fast progress in recent years because of its high specificity and activation by endogenous substances. A variety of multifunctional nanomaterials such as metal-, metal oxide-, and metal-sulfide-based nanocatalysts have been designed and constructed to trigger the *in situ* Fenton or Fenton-like reaction within the tumor microenvironment (TME) to generate highly cytotoxic hydroxyl radicals (•OH), which is highly efficient for the killing of tumor cells. However, research is still required to enhance the curative outcomes and minimize its side effects. Specifically, the therapeutic efficiency of certain CDTs is still hindered by the TME, including low levels of endogenous hydrogen peroxide ($H_2O_2$), overexpression of reduced glutathione (GSH), and low catalytic efficacy of Fenton or Fenton-like reactions (pH 5.6–6.8), which makes it difficult to completely cure cancer using monotherapy. For this reason, photothermal therapy (PTT) has been utilized in combination with CDT to enhance therapeutic efficacy. More interestingly, tumor heating during PTT not only causes damage to the tumor cells but can also accelerate the generation of •OH via the Fenton and Fenton-like reactions, thus enhancing the CDT efficacy, providing more effective cancer treatment when compared with monotherapy. Currently, synergistic PT-enhanced CDT using multifunctional nanomaterials with both PT and chemodynamic properties has made enormous progress in cancer theranostics. However, there has been no comprehensive review on this subject published to date. In this review, we first summarize the recent progress in PT-enhanced Fenton-based CDT for cancer treatment. We then discuss the potential and challenges in the future development of PT-enhanced Fenton-based nanocatalytic tumor therapy for clinical application.

## 1. Introduction

Cancer remains a major threat to human health worldwide because of the intense physical pain, high cytotoxicity, toxic side effects, and poor therapeutic efficiency associated with traditional therapeutic strategies, such as surgery, chemotherapy (CHT), and radiotherapy [1–14]. Numerous studies have attempted to explore new therapeutic strategies, such as photothermal therapy (PTT), chemodynamic therapy (CDT), photodynamic therapy (PDT), sonodynamic therapy (SDT), immunotherapy (IMT), and starvation therapy (ST), with high efficacy and reduced side effects [15–21]. New therapeutic strategies have been successfully used as an interesting alternative to traditional therapeutic

* Corresponding author. Department of Applied Chemistry, Kumoh National Institute of Technology, Daehak-ro 61, Gumi, Gyeongbuk, 39177, Republic of Korea.
** Corresponding author. Department of Chemical and Biological Engineering and R&E Center for Chemical and Biological Engineering (BK21 FOUR), Korea University, Seoul, 02841, Republic of Korea.
*E-mail addresses:* jbkim3@korea.ac.kr (J. Kim), euesoon@kumoh.ac.kr (E.-S. Jang).

https://doi.org/10.1016/j.mtbio.2021.100197
Received 30 September 2021; Received in revised form 27 December 2021; Accepted 28 December 2021
Available online 4 January 2022
2590-0064/© 2021 Published by Elsevier Ltd. This is an open access article under the CC BY-NC-ND license (http://creativecommons.org/licenses/by-nc-nd/4.0/).

strategies, and they are integrated with diagnostic imaging techniques, which are promising for cancer diagnosis and treatment [22,23]. However, monotherapy (e.g., PTT, CDT, PDT, SDT, IMT, or ST alone) cannot maximize the therapeutic efficiency because it is insufficient to effectively eliminate all of the tumor tissue, especially for large tumors [24]. Therefore, there are still many challenges to be overcome for the development of new strategies in the preclinical and clinical research of tumors to move away from monotherapy to combination cancer therapy (e.g., PT-enhanced CDT) to improve the therapeutic efficacy [25–28].

CDT is an emerging nanocatalyst-based therapeutic strategy for tumor-specific therapy that has been developed over the last five years [29–31]. It is well known that CDT is highly selective for tumors and can greatly reduce side effects in normal tissues because it can induce tumor cell death through protein, DNA, and lipid damage upon the decomposition of $H_2O_2$ to generate highly toxic reactive oxygen species (ROS) such as •OH via intratumoral metal ion (e.g., $Fe^{2+}$, $Cu^{2+}$, $Co^{2+}$, etc.)-mediated Fenton or Fenton-like reactions [32–34]. Compared with other therapeutic modalities, CDT is initiated by endogenous stimuli, which is exceedingly selective and logical, as well as highly sensitive to the concentration of catalytic ions and the Fenton or Fenton-like reaction in the TME (e.g. $H_2O_2$, GSH, and pH value) [35]. In addition, CDT has several unique advantages, such as high tumor specificity, stimulus activation, lower systemic toxicity, and the ability to regulate the TME, for cancer treatment [36,37]. Despite its potential, the use of CDT alone is limited by issues such as the low content of endogenous $H_2O_2$ within the tumor, low catalytic efficacy of the Fenton or Fenton-like reactions in the mildly acidic TME (pH 5.6–6.8), and the overexpression of reduced glutathione (GSH) in the TME, which reduces •OH productivity and the therapeutic efficiency of CDT [38–40]. In particular, the neutral pH and mildly acidic pH (pH 5.6–6.8) of the TME are always weakened and non-beneficial for the Fenton reaction, which is only effective under relatively strong acidic conditions (pH 3.0–5.0) [41,42]. However, the low generation rate of the •OH in the mildly acidic TME limits the therapeutic efficacy of CDT [24,25,28,43]. Thus, increasing the production of •OH in the mildly acidic TMEs is critical for the further development of CDT.

Combination cancer therapy has emerged and achieved satisfactory therapeutic effects, which can produce significant synergistic effects and minimize adverse effects [24,44,45]. PT-based combination cancer therapies, such as PT-enhanced CDT [46–48], PT-enhanced PDT [49,50], and chemo-PT-enhanced PDT [26,51], have received a significant amount of research attention because of their outstanding super-additive effect. Among these, synergistic PT-enhanced CDT has recently emerged as a promising therapeutic strategy for cancer therapy due to its high selectivity, low toxicity, and negligible invasiveness [52–55]. In addition, PT-enhanced CDT has been utilized in combination with CHT, PDT, SDT, IMT, and ST to increase tumor treatment performance [56]. It has been recognized that the integration of more therapeutic modalities such as PT-enhanced CDT with CHT, PDT, SDT, IMT, and ST, and diagnostic imaging techniques into one nanoplatform will further enhance the tumor suppression effect because of their synergistic effects [53,56].

Based on the basic principle that evaluated temperature can accelerate the reaction rate of Fenton or Fenton-like reactions, increasing the temperature in the tumor area will be an efficient strategy to enhance the efficacy of the Fenton or Fenton-like reactions with an increased yield of •OH, which has been generally employed because of its practicability and simplicity [24,27,41,42,48,57–59]. As previously reported tumor-heating strategies, PTT is a new type of cancer treatment strategy that converts near-infrared (NIR) light energy (700–1300 nm) into heat to kill cancer cells [60–62]. PTT has several advantages: the NIR wavelength is located in the "biological transparency window," which is minimally absorbed by biological tissue, blood, or water; PTT is minimally invasive, highly selective, has a high spatial resolution, deep penetration, and low toxicity, which utilizes PT conversion to generate local heating for the ablation of tumors [29,30,63]. More interestingly, the PT effect on the tumor area not only causes damage to the tumor cells but can also accelerate the formation of ROS, such as •OH, thus enhancing the CDT efficacy, providing more effective cancer treatment [64]. Therefore, a reasonable combination of PTT with other therapeutic modalities (CDT) using multifunctional nanomaterials is highly desirable toward enhancing therapeutic efficiency [52,65–68]. In addition, there is also an urgent need to develop multifunctional nanomaterials with both PT and chemodynamic properties for PT-enhanced CDT, which can help toward the development of highly effective combination cancer therapies [24,33,69].

To date, a variety of multifunctional nanomaterials, such as metal-, metal oxide-, and metal sulfide-based nanomaterials, have been widely studied for PT-enhanced CDT because of their strong NIR absorption, photothermal conversion efficiency (PCE) properties, biocompatibility, and chemodynamic properties [47,70–72]. In addition, a variety of multifunctional nanomaterials with diagnostic imaging properties have been widely used to improve imaging quality, which has excellent NIR absorption properties, magnetic properties, and other unique physicochemical properties, leading to more efficient and promising applications in diagnostic imaging [45,73]. Therefore, combination cancer therapy allows precise diagnosis and highly efficient tumor therapy, which has the potential to overcome the aforementioned drawbacks. In this review, we summarize the recent progress in multifunctional nanomaterials for PT-enhanced Fenton-based nanocatalytic tumor therapy.

## 2. Fenton or Fenton-like reaction in PT-enhanced CDT

Recently, various metal-based nanomaterials have been developed for CDT such as Fe, Cu, Co, Mn, Cr, Ag, etc [56]. CDT is generally based on Fenton or Fenton-like reactions and is used to trigger the *in situ* Fenton or Fenton-like reaction within the TME to produce a large amount of toxic •OH to kill cancer cells, and is a promising anticancer therapy with high specificity and minimal invasiveness [74–78]. Up to now, a lot of iron (Fe)-based nanocatalysts (e.g., Fe, $Fe_3O_4$, $FeS_2$, etc.) with different nanostructures or formulations have been developed as a Fenton agent for CDT, which represent highly efficient Fenton reagents that trigger the intratumoral Fenton chemical reaction, resulting in extremely high nanocatalytic efficacy as well as high biocompatibility [74,77,78]. The specific Fenton reaction is commonly based on $Fe^{2+}$ or $Fe^{3+}$, which can produce •OH by catalyzing the decomposition of $H_2O_2$, resulting in the destruction of proteins, lipids, and DNA, allowing efficient tumor-specific treatment without producing significant side effects in healthy cells [74, 79–85]. The relevant equations (Eqs. (1) and (2)) are shown below:

$$Fe^{2+}+H_2O_2 \rightarrow Fe^{3+}+•OH + OH^- \quad (1)$$

$$Fe^{3+}+H_2O_2 \rightarrow Fe^{2+}+•OOH + OH^+ \quad (2)$$

Apart from Fe-based nanocatalysts, other metal-based nanocatalysts based on Cu, Co, Mn, Cr, and Ag have also been developed as Fenton-like agents for CDT, which (e.g., $Cu^+$, $Co^{2+}$, $Mn^{2+}$, $Cr^{3+}$, and $Ag^+$) can also catalyze the *in situ* decomposition of acidic $H_2O_2$ into highly toxic •OH via Fenton-like reactions leading to the specific destruction of tumor cells [33,86–92]. For example, $Cu^+$ or $Cu^{2+}$ can also act as a Fenton-like catalyst for CDT, which can more easily react with $H_2O_2$ to generate •OH in the TME [33]. The copper (Cu)-based catalytic reactions are shown in Equations (3) and (4).

$$Cu^+ + H_2O_2 \rightarrow Cu^{2+} + •OH + OH^- \quad (3)$$

$$Cu^{2+} + H_2O_2 \rightarrow Cu^+ + •OOH + H^+ \quad (4)$$

Fenton or Fenton-like reactions catalyzed by metal-based nanocatalysts commonly require mild acidic pH conditions (pH 3.0–5.0) for higher reaction rates. However, the pH of the TME is in the range of 5.6–6.8, which leads to the low catalytic efficacy of the Fenton or Fenton-like reactions [74,79,81]. In addition, the low concentration of $H_2O_2$ in the TME (<100 μM) generates low concentrations of •OH, which also hinders the effect of CDT [93,94]. Based on the basic principle that

increasing the tumor tissue temperature by PTT can expedite the reaction rate of the Fenton or Fenton-like reactions, it can potentially produce a sufficient amount of the toxic •OH to induce tumor cell death [84,85]. In particular, the mildly acidic TME (pH 5.6–6.8) has a significantly less effective role in the Fenton reaction without PT treatment [95,96]. Therefore, PT-enhanced Fenton-based nanocatalytic tumor therapy can effectively enhance the reaction kinetics of the classical Fenton reaction [93,94]. Numerous nanomaterials are capable of catalyzing the Fenton reaction with NIR laser irradiation for the PT-enhanced Fenton reaction in CDT against cancer [97,98].

## 3. Multifunctional nanomaterials for PT-enhanced CDT

In recent years, numerous nanomaterials, such as metal (Fe, Cu, Au, etc.)-, metal oxide ($WO_3$, $MoO_\chi$, $MnO_2$, etc.)- and metal sulfide ($Cu_{2-x}S$, $CoS_2$, $MoS_2$, etc.)-based nanomaterials with both PT and chemodynamic properties, have been developed for PT-enhanced CDT due to their excellent biocompatibility (Table 1) [27,48,87,99–101]. Multifunctional nanomaterial-based contrast agents have been widely used to improve imaging quality, and contrast agents have excellent near-infrared (NIR) absorption properties, magnetic properties, and other unique physicochemical properties, leading to more efficient and promising applications in multimodal imaging, such as photoacoustic imaging (PAI), fluorescence imaging (FLI), magnetic resonance imaging (MRI), and computed tomography (CT) [45,73,102]. During CDT, Fenton or Fenton-like reactions can be triggered by various metal-based nanocatalysts [36,56,103]. Numerous nanomaterials have been used to catalyze the decomposition of $H_2O_2$ to produce •OH, which destroys tumors by triggering intratumoral Fenton or Fenton-like reactions during CDT [104–106]. However, the mildly acidic TME decreases the •OH productivity [107,108]. Thus, there is an urgent need to improve the speed of •OH production in the mildly acidic TME [109]. Most importantly, the tumor-heating effect of PTT may accelerate the generation of •OH, thus enhancing the efficacy of CDT [110–115]. The combination of PT-enhanced CDT is highly desirable for generating a synergistic combination cancer therapy because the heat accelerates Fenton chemistry [110].

**Table 1**
Summary of multifunctional nanomaterials for PT-enhanced CDT.

| Nanomaterials | Composition | Size (nm) | % PCE ($\eta$) | Irradiation conditions | Temp (°C) | Cell line/animal model | Treatment/imaging | Ref |
|---|---|---|---|---|---|---|---|---|
| Fe-based nanomaterials | $FeS_2$-PEG | 180–200 nm | 28.6% | 808 nm, 1.5 W/cm$^2$, 5 min | 50 | MCF-7, and 4T1 cells; 4T1 tumor-bearing mouse | *In vitro* and *in vivo* PTT-CDT/MRI | [27] |
| | $Fe_3O_4$@PPy@GOD NCs | 163.5 nm | 35.1 and 66.4% | 808 nm or 1064, 1.0 W/cm$^2$, 15 min | 59 | L929, 4T1, HeLa, and HUVEC cell lines; 4T1 tumor-bearing mice | *In vitro* and *in vivo* PTT-CDT/PAI/MRI | [59] |
| | PSAF NCs | 69.5 nm | 19.21% | 808 nm, 2.0 W/cm$^2$, 10 min | 45 | 4T1 cell line; 4T1 tumor-bearing mice | *In vitro* and *in vivo* PTT-CDT | [116] |
| | BSA-$CuFeS_2$ NPs | 4.9 ± 0.9 nm | 38.8% | 808 nm, 1.5 W/cm$^2$, 5 min | 63 | 4T1 cell line; 4T1 tumor-bearing mice | *In vitro* and *in vivo* PTT-CDT/FLI/MRI | [109] |
| | PMFG | 12–20 nm | – | 808 nm, 0.8 W/cm$^2$, 5 min | 45 | MCF-7 cell line | *In vitro* PTT-CDT | [25] |
| | $Nb_2C$-IO-$CaO_2$ | 150 nm | 32.1% | 1064 nm, 1.5 W/cm$^2$, 10 min | 54.4 | HUVEC and 4T1 cell lines; 4T1 tumor-bearing mice | *In vitro* and *in vivo* PTT-CDT | [117] |
| | AFP NPs | 242.3 nm | – | 808 nm, 1.0 W/cm$^2$, 10 min | 47.7 | 4T1 cell line; 4T1 tumor-bearing mice | *In vitro* and *in vivo* PTT-CDT/PAI | [118] |
| | γ-$Fe_2O_3$-GOx-DMSN NCs | 130 nm | 49.8% | 808 nm, 1.0 W/cm$^2$, 5 min | 50 | HeLa and U14 cell lines; U14 tumor-bearing mice | *In vitro* and *in vivo* PTT-CDT/MRI | [119] |
| | FP NRs | 180 nm | 56.6% | 1064 nm, 0.5 W/cm$^2$, 10 min | 55.7 | HeLa, L929, and U14 cell lines; U14 tumor-bearing mice | *In vitro* and *in vivo* SDT-PTT-CDT/PAI/MRI | [48] |
| | EA-Fe@BSA NPs | 13.84 ± 2.53 | 31.9% | 808 nm, 1.0 W/cm$^2$, 15 min | 41 | HCT116 and HUCEC cell lines; HCT116 tumor-bearing mice | *In vitro* and *in vivo* PTT-CDT/MRI | [110] |
| | BSO–$FeS_2$ NPs | 7.27 ± 1.43 nm | 49.5% | 808 nm, 1.0 W/cm$^2$, 5 min | 45 | 4T1 cell line; 4T1 tumor-bearing mice | *In vitro* and *in vivo* PTT-CDT/PDT/PAI | [120] |
| | RLR NPs | 200 nm | 26.8%, | 808 nm, 1.5 W/cm$^2$, 5 min | 49 | MDA-MB-231 cell line; MDA-MB-231 tumor-bearing mice | *In vitro* and *in vivo* chemo-PTT-CDT/MRI/FLI | [121] |
| | $FeS_2$@RBCs | 185.2 nm | 30.2% | 1064 nm, 1.0 W/cm$^2$, 5 min | 25.3 | 4T1 cell line; 4T1 tumor-bearing mice | *In vitro* and *in vivo* PTT-CDT/MRI/FLI | [122] |
| | Fe-POM | 12.9 nm | 51.4% | 1060 nm, 1.0 W/cm$^2$, 10 min | 50 | HUVEC and HeLa cell lines; HeLa tumor-bearing mice | *In vitro* and *in vivo* PTT-CDT/PAI | [123] |
| | PB@FePt-HA-g-PEG | 150 nm | 28.14% | 808 nm, 1.5 W/cm$^2$, 10 min | 68.3 | L02 and MCF-7 cell lines; MCF-7 tumor-bearing mice | *In vitro* and *in vivo* PTT-CDT/MRI/CT | [124] |
| | FMO | 450 nm | 48.5% | 808 nm, 0.7 W/cm$^2$, 5 min | 50 | HeLa, and L929 cell lines; HeLa tumor-bearing mice | *In vitro* and *in vivo* PTT-CDT/MRI | [125] |
| | CFMG hydrogel | – | – | 808 nm, 1.0 W/cm$^2$, 5 min | 49.5 | A375 and C2C12 cell lines; A375 tumor-bearing mice | *In vitro* and *in vivo* PTT-CDT | [126] |
| | FeO/$MoS_2$-BSA | 150 nm | 56% | 1064 nm, 0.75 W/cm$^2$, 5 min | 52 | HeLa and U14 cell lines; U14 tumor-bearing mice | *In vitro* and *in vivo* PTT-CDT/MRI | [127] |
| | F-BS NCs | 80 nm | 23.46% | 808 nm, 1.2 W/cm$^2$, 5 min | 59.1 | L929 and HeLa cell lines; HeLa tumor-bearing mice | *In vitro* and *in vivo* PTT-CDT/PAI | [128] |
| | Fe(III)-GA/GOx@ZIF-Azo | 3 nm | 65.3% | 808 nm, 1.54 W/cm$^2$, 10 min | 46 | MCF-7 cell line; MCF-7 tumor-bearing mice | *In vitro* and *in vivo* PTT-CDT/FLI | [129] |
| Cu-based nanomaterials | CP NCS | 22 nm | 27% | 1064 nm, 0.75 W/cm$^2$, 5 min | 51 | L929, HeLa, and U14 cell lines; U14-tumor-bearing mice | *In vitro* and *in vivo* PTT-CDT/MRI/PAI | [130] |
| | PEG-$Cu_2Se$ HNCs | 86.89 ± 19.93 nm | 50.89% | 1064 nm, 0.75 W/cm$^2$, 5 min | 58.4 | HUVEC and 4T1 cell lines; 4T1 tumor-bearing mice | *In vitro* and *in vivo* PTT-CDT/PAI | [41] |

(*continued on next page*)

**Table 1** (*continued*)

| Nanomaterials | Composition | Size (nm) | % PCE ($\eta$) | Irradiation conditions | Temp (°C) | Cell line/animal model | Treatment/imaging | Ref |
|---|---|---|---|---|---|---|---|---|
| | SC@G NSs | 60.94 nm | 46.3% | 1064 nm, 1.0 W/cm$^2$, 5 min | 47.5 | 293T and 4T1 cell lines; 4T1 tumor-bearing mice | *In vitro* and *in vivo* PTT-CDT/PAI | [131] |
| | PDA@Cu/ZIF-8 NPs | 50 nm | – | 808 nm, 1.0 W/cm$^2$, 10 min | 70 | MCF-7, A549, and MDA-MB-231 cell lines; MCF-7 tumor-bearing mice | *In vitro* and *in vivo* PTT-CDT | [72] |
| | CuO@AuCu-TPP | 255 nm | 37.9% | 808 nm, 1.0 W/cm$^2$, 5 min | 51.6 | HeLa cell line; HeLa tumor-bearing mice | *In vitro* and *in vivo* PTT-CDT/PAI/CT | [132] |
| | $Cu_9S_8$ NPs | ~18.05 nm | – | 808 nm, 0.5 W/cm$^2$, 5 min | 43 | 4T1 and HUVEC cell lines; 4T1 tumor-bearing mice | *In vitro* and *in vivo* PTT-CDT/PAI | [64] |
| | CuO@CNSs-DOX | 15 nm | 10.14% | 808 nm, 2.0 W/cm$^2$, 10 min | 60.3 | 4T1 cell line; 4T1 tumor-bearing mice | *In vitro* and *in vivo* Chemo-PTT-CDT/PAI | [133] |
| | MCBR | 130 nm | 24.6% | 808 nm, 1.5 W/cm$^2$, 5 min | 75 | CT26 cell line; CT26 tumor-bearing mice | *In vitro* and *in vivo* PTT-CDT/IMT/CT/MRI | [47] |
| | PEG-CMS@GOx | 5.88 nm | 63.27% | 1064 nm, 0.48 W/cm$^2$, 5 min | 52 | HeLa, L929, and U14 cell lines; U14 tumor-bearing mice | *In vitro* and *in vivo* PTT-CDT/PDT/IMT/PAI | [134] |
| | PFN | 22 nm | 30.17% | 1064 nm, 1.0 W/cm$^2$, 5 min | 55 | Panc02 cell line; Panc02 tumor-bearing mice | *In vitro* and *in vivo* PTT-CDT/MRI | [135] |
| Gold-based nanomaterials | CAANSs | 52 nm | – | 808 nm, 2.4 W/cm$^2$, 10 min | 68.4 | HeLa cell line | *In vitro* chemo-PTT | [136] |
| | Au@HCNs | 275 ± 0.355 nm | 26.8% | 808 nm, 2.0 W/cm$^2$, 10 min | 52.9 | CT26 cell line; CT26 tumor-bearing mice | *In vitro* and *in vivo* PTT-CDT | [137] |
| | Au@$MnO_2$ | 25 nm | 23.6% | 808 nm, 1.0 W/cm$^2$, 15 min | 42 | 4T1 cell line; 4T1 tumor-bearing mice | *In vitro* and *in vivo* PTT-CDT/PAI/MRI | [43] |
| | $Au_2$Pt-PEG-Ce6 | 42 ± 3 nm | 31.5 | 808 nm, 1.0 W/cm$^2$, 5 min; 650 nm, 0.259 W/cm$^2$, 5 min | 58.7 | HeLa, L929, and U14 cell lines; U14 tumor-bearing mice | *In vitro* and *in vivo* PTT/PDT/CDT/CT/PAI | [138] |
| Metal oxide-based nanomaterials | $WO_{3-x}$@$\gamma$-PGA NPs | 5.73 ± 0.93 nm | 25.8% | 1064 nm, 0.5 W/cm$^2$, 5 min | 46 | HUVEC and 4T1 cell lines; 4T1 tumor-bearing mice | *In vitro* and *in vivo* PTT-CDT/PAI | [24] |
| | DCDMs | 123 nm | 51.5% | 808 nm, 1.0 W/cm$^2$, 10 min | 58.7 | L929, HeLa, and U14 cell lines; U14 tumor-bearing mice | *In vitro* and *in vivo* PTT-CDT/FLI/CT/MRI | [139] |
| | HMCMs | 80 nm | 23.5% | 808 nm, 1.0 W/cm$^2$, 8 min | 54 | MCF-7, MDA-MB-231, and MGC-803 cell lines; MCF-7 tumor-bearing mice | *In vitro* and *in vivo* PTT-CDT/FLI | [46] |
| Metal sulfide-based nanomaterials | $CoS_2$ NCs | 19.79 ± 5.2 nm | 60.4% | 808 nm, 1.0 W/cm$^2$, 10 min | 55.4 | 4T1 and HUEVC cell lines; 4T1 tumor-bearing mice | *In vitro* and *in vivo* PTT-CDT/PAI | [42] |

### 3.1. Iron-based nanomaterials for PT-enhanced CDT

Iron (Fe)-based nanomaterials have been widely used in versatile biomedical applications, such as drug delivery, tissue engineering, PTT, PDT, CDT, SDT, ST, and multimodal imaging [140–145]. Some formulations of iron-based nanomaterials have been approved by the United States (US) Food and drug administration (FDA) for use in humans as therapeutics for iron deficiency, drug carriers for cancer therapy, and as contrast agents in MRI [81,146–149]. Recently, iron-based nanomaterials have attracted a lot of attention as antiferromagnetic pyrite Fenton nanocatalysts for cancer therapy [81]. For example, Tang et al. first reported the use of antiferromagnetic pyrite polyethylene glycol ($FeS_2$-PEG) nanocubes for self-enhanced MRI and PT-enhanced CDT (Fig. 1a). Iron pyrite ($FeS_2$) ion has been successfully used in a new era of cancer treatment because it can catalyze the production of ROS. PEG is a synthetic and biocompatible polymer that has been used in various applications, such as PEGylation, drug delivery, cancer therapy, and wound healing. $FeS_2$ nanocubes were modified with SH-PEG to enhance their biocompatibility and solubility. More interestingly, the localized heat generated by $FeS_2$-PEG via the PT effect, which accelerates the intratumoral Fenton reaction to efficiently generate •OH to kill tumor cells, implies that the synergistic effect of PTT and CDT into a single nanomaterial can be used as a "one-for-all" formulation. $FeS_2$-PEG is cube-shaped with an average diameter of 180–200 nm. The PCE ($\eta$) values of $FeS_2$-PEG and $FeS_2$@$Fe_\chi O$-PEG are 28.6 and 29.5%, respectively. The *in vitro* PT-enhanced CDT effect of $FeS_2$-PEG shows that the heat generated by the PT effect can accelerate and enhance the amount of •OH formed, suggesting that increased temperature can simultaneously induce ionization and improve the production of •OH. 4T1 tumor-xenografted mice were intratumorally injected with $FeS_2$-PEG. The tumor-bearing mice treated with $FeS_2$-PEG and laser irradiation were almost completely inhibited, implying the potential of $FeS_2$-PEG as a PTT/CDT agent for cancer therapy. The $T_1$-and $T_2$-weighted magnetic resonance (MR) signal intensities showed a significant increase of 56.38 and 2.49%, respectively, which resulted in the synergism of the self-enhanced MRI-guided PT-enhanced CDT (Fig. 1b) [27].

As a representative $FeS_2$-based Fenton nanocatalyst in CDT, She et al. designed red blood cell membrane (RBC)-coated $FeS_2$ for effective PT-enhanced CDT using an FDA-approved 1064 nm laser at 1.0 W/cm$^2$ (Fig. 2a). $FeS_2$ was synthesized by a facile solvothermal reaction and $FeS_2$ was surface-modified with DSPE-PEG2000 to improve the water solubility ($FeS_2$-PEG). RBC was finally coated on the surface of $FeS_2$-PEG to form $FeS_2$@RBCs. $FeS_2$ has a cubic shape with an average diameter of 100–120 nm. The hydrodynamic size of $FeS_2$@RBCs slightly increases from 168.3 nm ($FeS_2$-PEG) to 185.2 nm, and their zeta potential of $FeS_2$@RBCs was −10.3 mV because of the negative charge of RBCs. The PCE ($\eta$) of $FeS_2$@RBCs was 30.2%. The synergetic effect of PT-enhanced CDT using $FeS_2$@RBCs has been widely demonstrated *in vitro* and *in vivo*. The *in vitro* PT-enhanced CDT effect of $FeS_2$@RBCs has been evaluated in 4T1 cells under laser irradiation, which showed a stronger inhibition rate of 4T1 cells when exposed to 1064 nm laser irradiation, suggesting the good synergistic PT-enhanced CDT antitumor effect upon 1064 nm laser

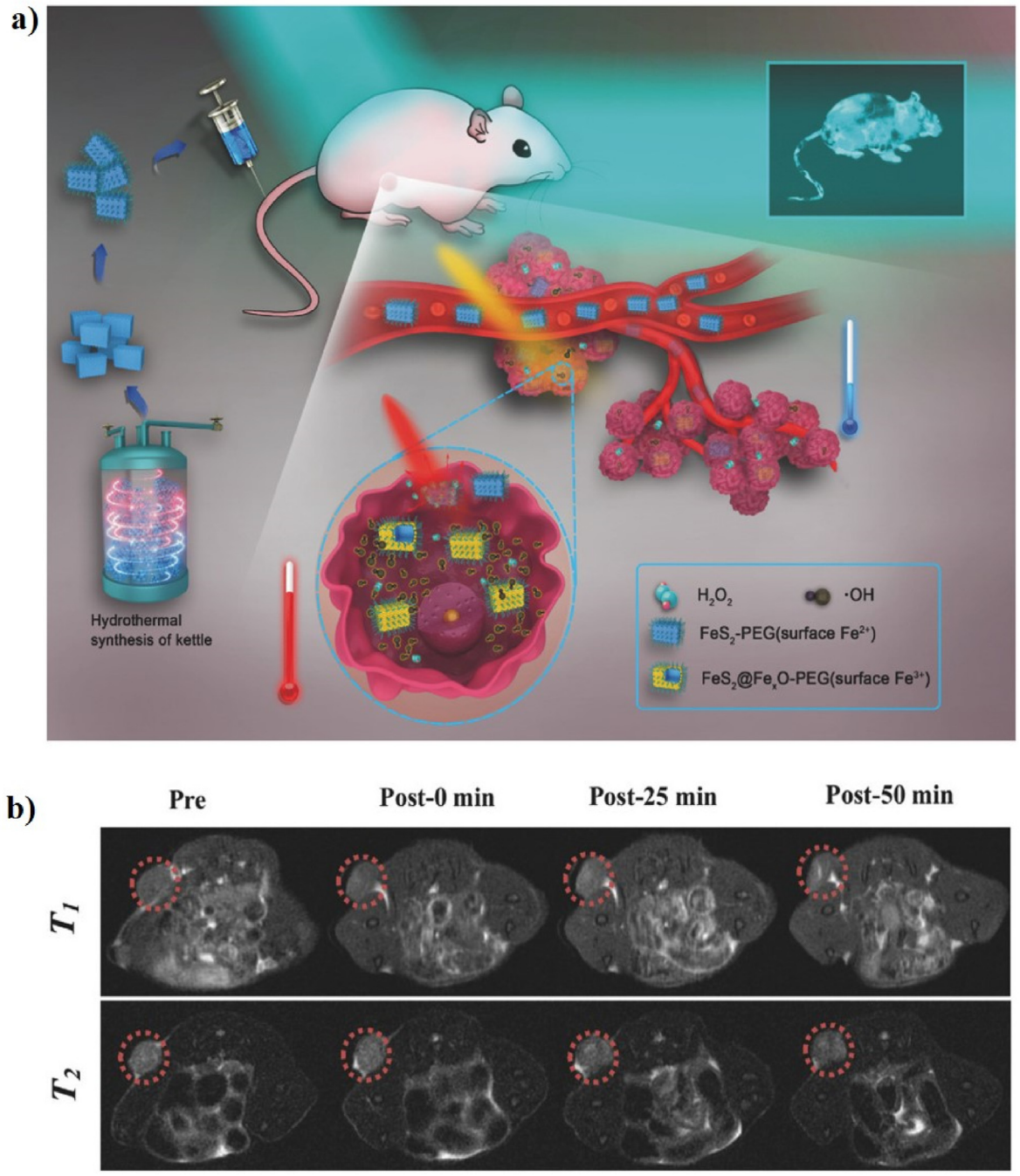


**Fig. 1.** (a) A schematic illustration of the preparation of $FeS_2$-PEG for self-enhanced MRI and PT-enhanced CDT. (b) *In vivo* $T_1$-and $T_2$-weighted MR images of tumor-bearing mice after intratumoral injection with $FeS_2$-PEG (the red dotted circles). Reprinted with permission of Ref. [27]. Copyright 2017 Wiley.

irradiation. CDT relies on the Fe ($FeS_2$@RBCs)-mediated Fenton reaction to induce cancer cell ferroptosis by catalyzing the decomposition of $H_2O_2$ into highly toxic •OH, which is only produced only in the TME without damaging healthy cells due to the high amount of $H_2O_2$ present in the tumor area. PT heating in the TME can significantly improve the Fenton reactivity and produce a high amount of •OH, which can effectively inhibit tumor growth with a clinically approved 1064 nm laser. In addition, $FeS_2$@RBCs can be used for diagnosis and MRI-guided PTT/CDT. 4T1 tumor-bearing mice were intravenously and intratumorally injected with $FeS_2$@RBCs to explore the MRI signal change in the TME, which shows the TME-enhanced capability of $FeS_2$@RBCs as an MRI contrast agent for imaging-guided therapy (Fig. 2b, c). Furthermore, 4T1 tumor-bearing mice were intravenously injected with the cyanine5 amine dye (Cy5)-modified $FeS_2$@RBCs for *in vivo* FLI. The Cy5-$FeS_2$@RBCs exhibit strong fluorescent signals in the TME 6 h post-injection, indicating that $FeS_2$@RBCs have superior accumulation at the tumor site, which is more beneficial for PT-enhanced CDT (Fig. 2d, e) [122].

Currently, several ultra-small Fe-based nanomaterials have been developed as a multifunctional theranostic platform, which has a pH-independent Fenton reaction property to produce •OH and photothermal conversion efficiency for PT-enhanced CDT [109]. The ultra-small nanomaterials can be passed through the kidneys, allowing them to be eliminated more quickly from the body and increase long-term biosafety [150,151]. For example, Chen et al. synthesized ultra-small bovine serum albumin (BSA)-modified chalcopyrite NPs

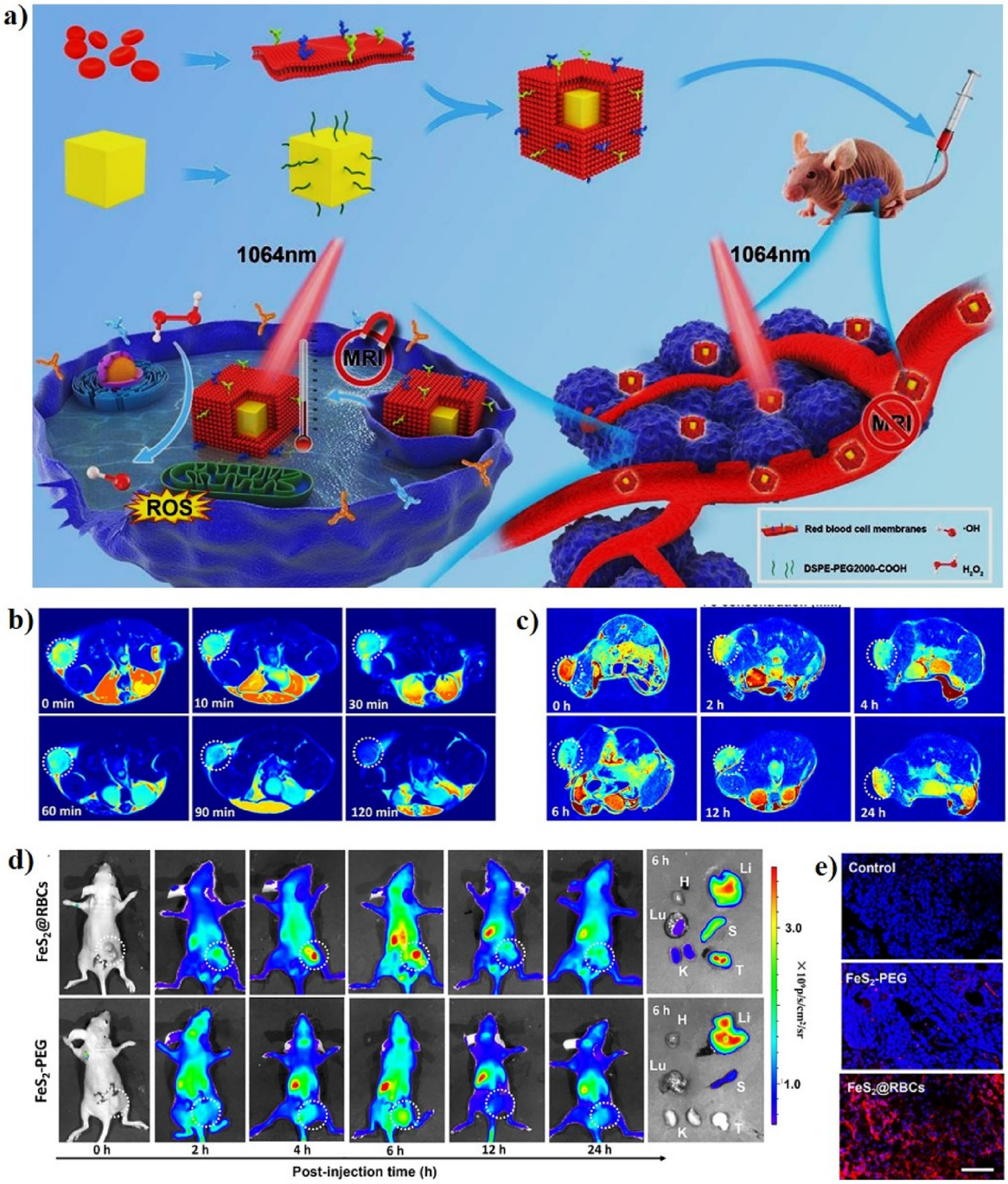


**Fig. 2.** (a) A schematic illustration of the preparation of $FeS_2$@RBCs for PT-enhanced CDT. *In vivo* $T_2$-weighted MR images of tumor-bearing mice at various time points before and after intratumoral (b) and intravenous (c) injection of $FeS_2$@RBCs. (d) *In vivo* FLI of tumor-bearing mice at various time points before and after intravenous injection of Cy5-modified $FeS_2$@RBCs and *ex vivo* FLI images of the tumors and main organs collected from the treated mice 6 h post-injection. (e) Confocal images of tumor tissues 6 h post-injection. DAPI and Cy5 are shown in blue and red, respectively. Reprinted with permission of Ref. [122]. Copyright 2020 Elsevier Ltd.

(BSA-$CuFeS_2$ NPs) for PT-enhanced CDT (Fig. 3). BSA is a protein that has been utilized as a stabilizer to bind Fe and Cu ions due to the high affinity of carboxyl groups and surfactants. $Na_2S{\cdot}9H_2O$ was then added to BSA-containing solutions to change the black color, implying the formation of BSA-$CuFeS_2$ NPs. The particles of BSA-$CuFeS_2$ NPs were mono-dispersed with an average size of $4.9 \pm 0.9$ nm. The PCE ($\eta$) value of the BSA-$CuFeS_2$ NPs reached 38.8%, indicating their potential as PTT agents. BSA-$CuFeS_2$ NPs exhibit pH-independent Fenton properties, which can produce a large amount of •OH in the weakly acidic TME. Subsequently, the heat generated by BSA-$CuFeS_2$ NPs can enhance the •OH-generating efficacy, which is a synergistic effect in favor of efficient tumor growth inhibition. The FLI of 4T1 tumor-bearing mice was intravenously injected with BSA-$CuFeS_2$ NPs at different time points. The fluorescence signal of the tumor area at 30 min post-injection increased 8.8-fold when compared with that in the control group, suggesting a high passive accumulation of BSA-$CuFeS_2$ NPs at the tumor site. MR imaging showed a dramatic dark effect at the tumor site and the tumor MR signal rapidly decreased to 43.2%, indicating that the BSA-$CuFeS_2$ NPs can serve as highly efficient MRI contrast agents to guide tumor ablation *in vivo*. More interestingly, the tumor treated with PTT/CDT was almost

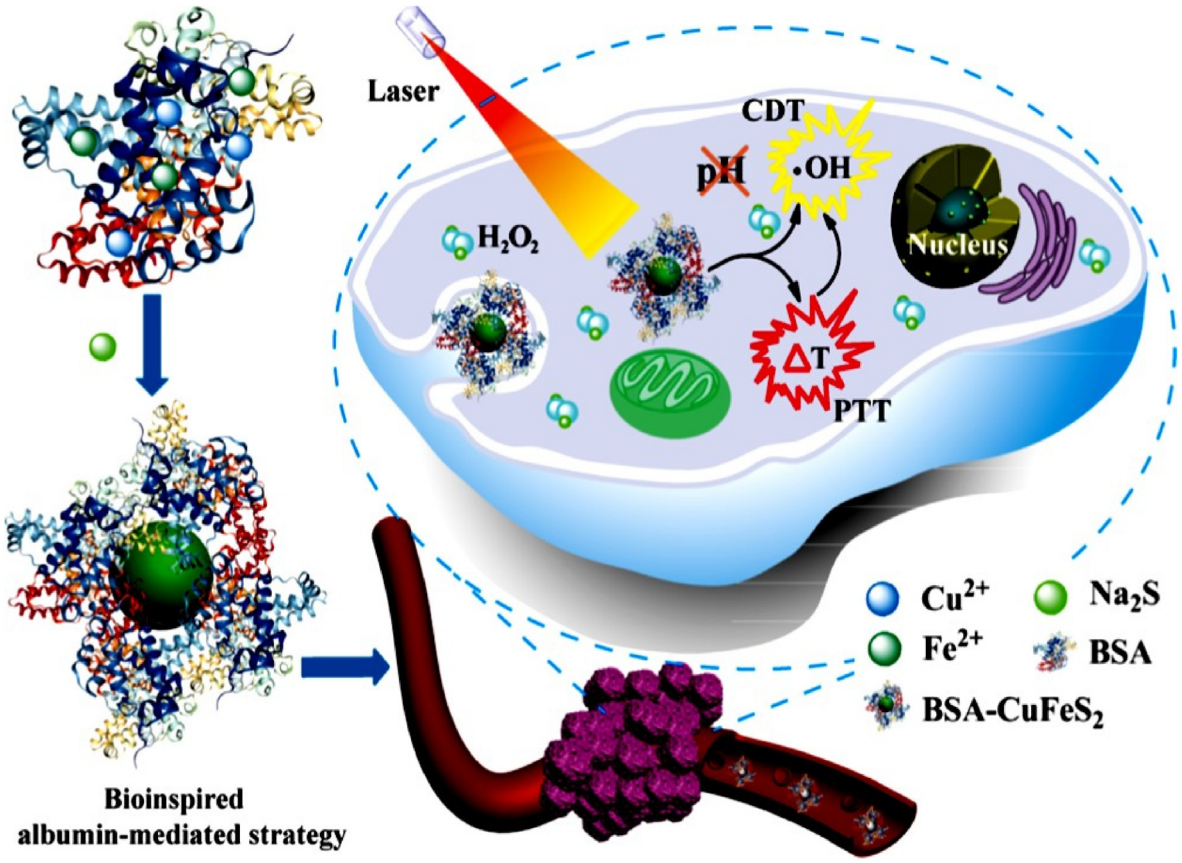


**Fig. 3.** A schematic representation of the fabrication of BSA-$CuFeS_2$ NPs for PT-enhanced CDT. Reprinted with permission of Ref. [109]. Copyright 2019 American Chemical Society.

completely inhibited post-injection of the BSA-$CuFeS_2$ NPs, suggesting that the BSA-$CuFeS_2$ NPs exhibit the MRI-guided synergistic PT-enhanced CDT for highly efficient tumor ablation [109].

Another study was designed the ultra-small Fe-based nanomaterials for PT-enhanced CDT. In 2002, Tian et al. constructed ultra-small ellagic acid (EA)-Fe BSA (EA-Fe@BSA) NPs as a CDT agent for PTT to synergistically enhance CDT (Fig. 4a). EA-Fe@BSA was prepared via the simple assembly of EA, Fe(III), and BSA for endogenous hydrogen sulfide ($H_2S$) and PT-enhanced CDT efficiency. The EA-Fe@BSA NPs show a monodispersed spherical morphology with an average diameter of 13.84 ± 2.53 nm and the PCE ($\eta$) of EA-Fe@BSA NPs before and after reaction with sodium hydrosulfide (NaHS) was ~31.9 and 31.2%, respectively. The *in vitro* therapeutic efficacy of the EA-Fe@BSA NPs accelerates the production of •OH upon the addition of NaHS and increases the temperature by the heat generated via PT. NaHS was chosen to induce endogenous $H_2S$ to explore the $H_2S$-stimulated CDT efficacy, which induced a greater conversion of Fe(III) in the EA-Fe@BSA NPs to Fe(II) and enhanced the CDT efficacy. The EA-Fe@BSA NPs exhibit obvious $T_1$-weighted MRI both *in vitro* and *in vivo*, indicating their potential application as MRI contrast agents (Fig. 4b–f). More importantly, the PT heating effect of the EA-Fe@BSA NPs also accelerated the production of •OH via Fenton reactions in the tumor area. Even though $H_2S$-enhanced CDT alone cannot inhibit the tumor, the synergy of $H_2S$-enhanced CDT and PT-enhanced CDT almost completely inhibits and destroys the tumor, demonstrating outstanding enhanced CDT efficacy upon $H_2S$ and PTT acceleration [110].

Iron oxide nanomaterials have broad potential in theranostic applications because of their excellent biocompatibility, photothermal conversion efficiency, and magnetic properties, which can be used as Fenton nanocatalysts for cancer therapy [152,153]. Similarly, Gao et al. reported the use of iron oxide (IO)-loaded niobium carbide ($Nb_2C$) MXene nanosheets ($Nb_2C$-IO) conjugated with calcium peroxide ($CaO_2$) NPs to form two-dimensional (2D) composite nanosheets ($Nb_2C$-IO-$CaO_2$) for PT-enhanced CDT (Fig. 5a, b). The $Nb_2C$ and $CaO_2$ NPs have average hydrodynamic sizes of 150 and 8 nm, respectively, and the zeta potential of $Nb_2C$-IO-$CaO_2$ is −5.3 mV. The PCE ($\eta$) of $Nb_2C$-IO-$CaO_2$ nanosheets, which act as potent and durable PT agents for PT-enhanced CDT, was 32.1%, which was higher than that of commonly reported photothermal agents, such as $Fe_3O_4$@CuS NPs (19.2%) [154] and $Fe_3O_4$ nanoclusters (20.8%) [155]. $Nb_2C$-IO-$CaO_2$ employs $CaO_2$ as a potent $H_2O_2$ supplier to sustain the IO NP-mediated catalytic Fenton reaction to produce a high amount of •OH to induce tumor cell death. In addition, the $Nb_2C$ nanosheets also serve as PT agents to convert NIR light into heat, which can greatly improve the intratumoral •OH yield *via* Fenton reactions, leading to a more satisfactory therapeutic effect. $Nb_2C$-IO-$CaO_2$ exhibits significantly higher cytotoxicity after laser irradiation, and the maximum apoptosis was 93.3% in 4T1 cells, resulting in PT-enhanced ROS generation by the Fenton reaction produced by $Nb_2C$-IO-$CaO_2$ with self-supplied $H_2O_2$. The *in vivo* synergistic PT-enhanced CDT efficiency of $Nb_2C$-IO-$CaO_2$ was evaluated and the tumor temperature of mice injected with $Nb_2C$-IO-$CaO_2$ rapidly increased to 54.4 °C upon laser irradiation at 1064 nm, leading to the complete inhibition of tumor growth, implying that $Nb_2C$-IO-$CaO_2$ has promising potential as a tumor therapeutic agent for PT-enhanced CDT [117].

Also, iron oxide-based Fenton nanocatalysts have excellent catalytic ability to generate •OH. For instance, Zhang et al. synthesized a novel iron oxide (FeO)/molybdenum disulfide ($MoS_2$) modified with BSA (FeO/$MoS_2$-BSA) for PT-enhanced CDT (Fig. 6a). 2D $MoS_2$ nanosheets

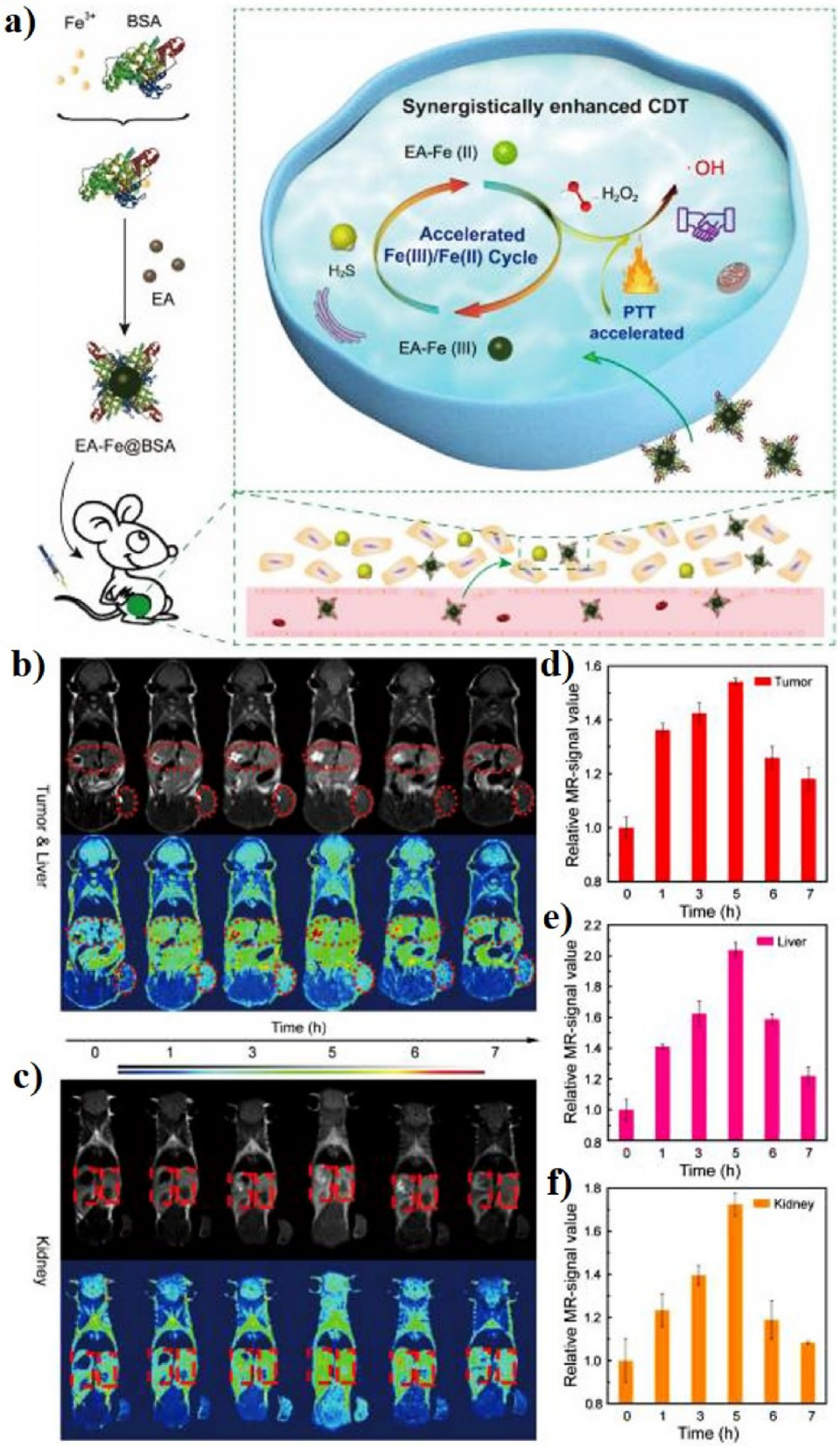


**Fig. 4.** (a) Schematic illustration of the synthesis of EA-Fe@BSA NPs for PT-enhanced CDT. *In vivo* MR images of the tumor and liver (b), and kidney (c) after intravenous injection of EA-Fe@BSA NPs. The corresponding MR signal intensities of the tumor (d), liver (e), and kidney (f) images. Reprinted with permission of Ref. [110]. Copyright 2020 IVYSPRING International Publisher.

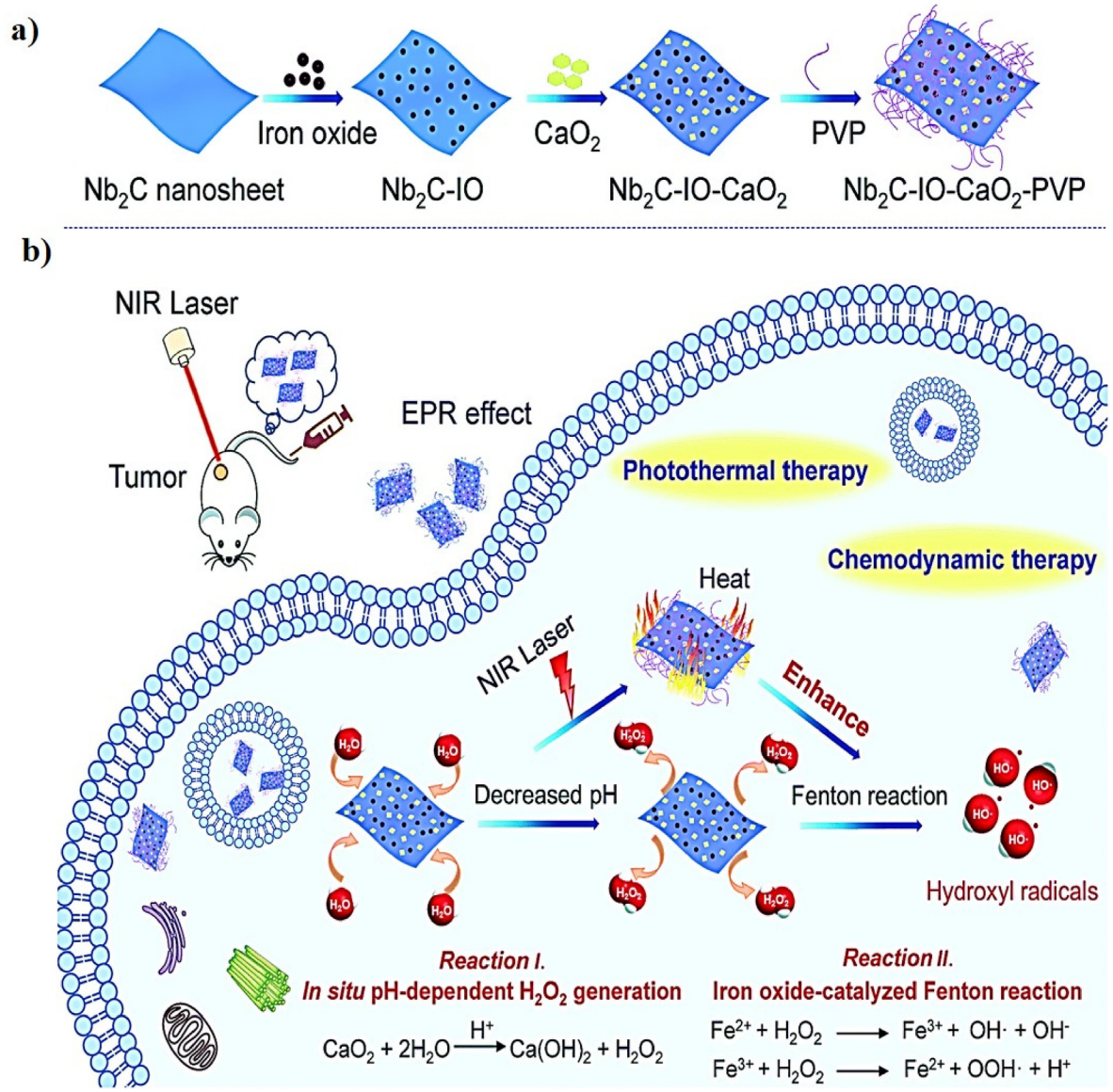


**Fig. 5.** A schematic illustration of (a) the preparation of $Nb_2C$-IO-$CaO_2$ nanosheets and (b) PT-enhanced CDT utilizing $Nb_2C$-IO-$CaO_2$ nanosheets. Reprinted with permission of Ref. [117]. Copyright 2019 Royal Society of Chemistry.

have been used as photoablation agents because of their strong NIR absorbance. In addition, $MoS_2$ nanosheets have a peroxidase-mimicking ability, allowing them to catalyze the decomposition of $H_2O_2$ to produce •OH. FeO/$MoS_2$ was synthesized via electrostatic interactions and then modified with BSA to enhance their biocompatibility. $MoS_2$ has an average size of 150 nm, and FeO has an average size of $8 \pm 3$ nm. The PCE ($\eta$) of the FeO/$MoS_2$-BSA nanocomposite at 1064 nm was calculated to be 56%, indicating its excellent PT performance. The $Mo^{4+}$ ions on the surface of the $MoS_2$ nanosheets can accelerate the conversion of $Fe^{3+}$ into $Fe^{2+}$, while $Fe^{2+}$ ions can decompose $H_2O_2$ to produce a large amount of •OH via Fenton reactions, which can be further improved by the PT effect. The *in vitro* therapeutic effect of FeO/$MoS_2$-BSA on HeLa cells was confirmed using calcein-AM and propidium iodide (PI) staining, which showed a stronger red fluorescence after 1064 nm laser irradiation, indicating the destruction of the HeLa cells by •OH and PT heat. The *in vivo* PT efficiency of the FeO/$MoS_2$-BSA nanocomposites on the U14 tumor xenograft model was demonstrated using an IR thermal camera (Fig. 6b). The temperature of the tumor area was increased to 52 °C upon 1064 laser irradiation for 10 min and the treated tumors were thoroughly ablated after the 5th day of treatment, implying that synergistic PT-enhanced CDT has high anti-cancer efficiency. Furthermore, the MR signal of the tumor area was observed with an increase in the concentration of FeO/$MoS_2$-BSA, confirming that FeO/$MoS_2$-BSA can act as a promising MRI contrast agent (Fig. 6c) [127].

A number of Fe-based nanomaterials showed great potential for PT-enhanced CDT because of their photothermal conversion efficiency and •OH generation capacity via Fenton reaction [156]. In 2019, Huo et al. fabricated PEGylated single-atom Fe-containing nanocatalysts (PSAF NCs) for highly efficient tumor inhibition *via* the Fenton reaction (Fig. 7a). Single-atom Fe catalysts (SAF NCs) have evolved to become highly efficient electrocatalysts, which will enable improved therapeutic efficiency in tumor-specific nanocatalytic therapy. 1,2-Distearoyl-*sn*-glycero-3-phosphoethanolamine-N-[amino(polyethylene glycol)] (DSPE-PEG-$NH_2$) is a linear heterobifunctional PEGylation reagent with a hydrophobic structure DSPE and amino-terminated PEG chain. The SAF NCs were PEGylated with DSPE-PEG-$NH_2$ via hydrophobic-hydrophobic interactions after vigorous sonication to form the PSAF NCs. The SAF NCs exhibit a uniform dodecahedral geometry with an average diameter of ~69.5 nm. When the PSAF NC aqueous solution (200 μg/mL) was irradiated with an 808 nm laser at 2.0 W/$cm^2$

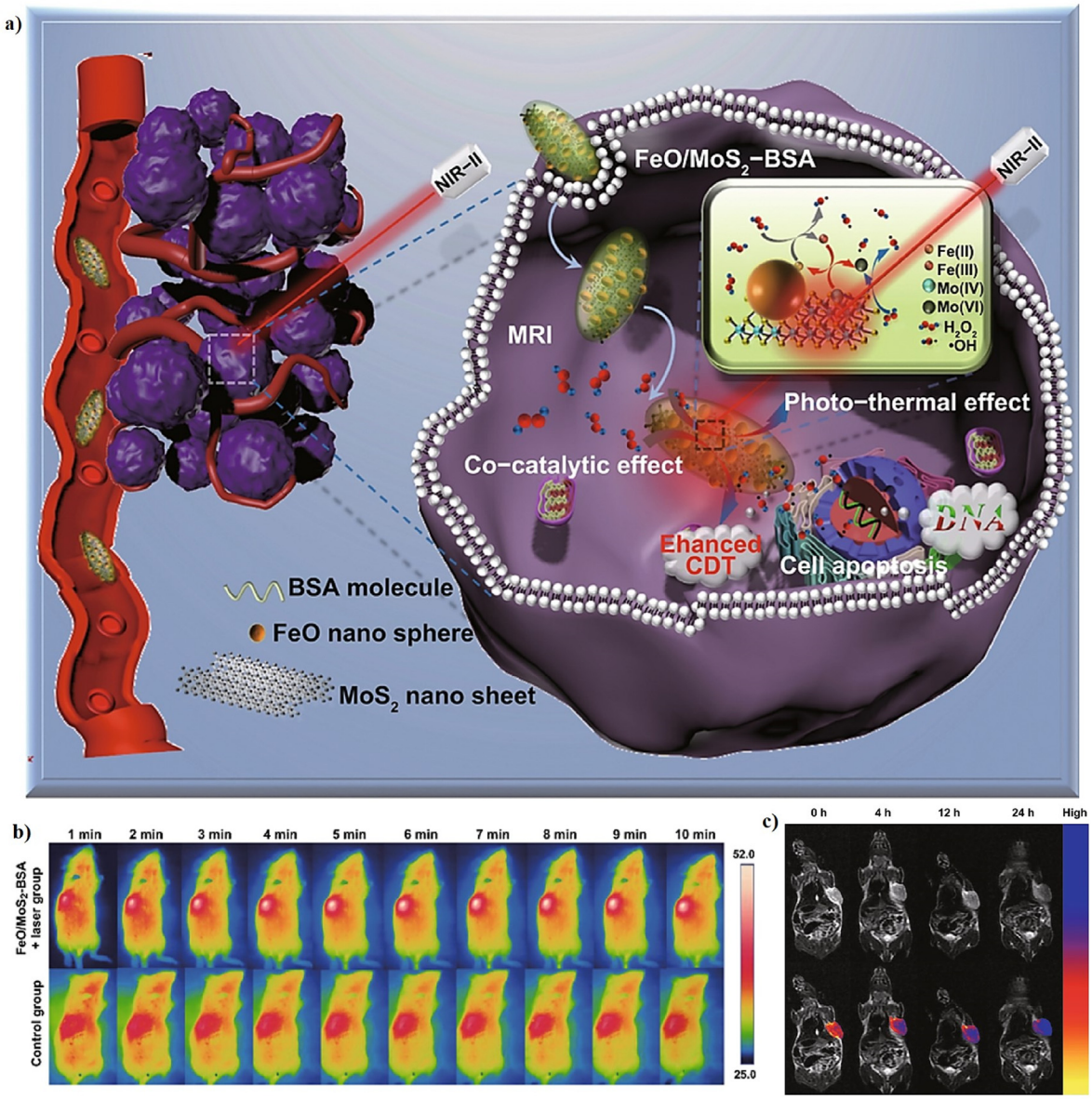


**Fig. 6.** (a) A schematic illustration of the fabrication of FeO/$MoS_2$-BSA for PT-enhanced CDT. (b) IR thermal images of tumor-bearing mice upon intravenous injection of normal saline and FeO/$MoS_2$-BSA, followed by 1064 nm laser irradiation at 0.75 W/$cm^2$ for 10 min. (c) *In vivo* MR imaging of tumor-bearing mice at various time points after intravenous injection of FeO/$MoS_2$-BSA. Reprinted with permission of Ref. [127]. Copyright 2020 Springer.

for 10 min, the temperature increased by 45 °C with high PT stability and strong PCE (19.21%). The *in vitro* therapeutic effects of PSAF NCs against 4T1 cells were evaluated, and cells treated with PSAF NCs + $H_2O_2$ exhibited a strong inhibitory effect. It is clear that the Fenton reaction catalyzed by PSAF NCs also resulted in the production of a large amount of toxic •OH and localized apoptosis and ferroptosis of tumor cells when exposed to $H_2O_2$ in the acidic TME, which can be effectively enhanced by the mild-PT effect. The *in vivo* catalytic therapeutic performance of PSAF NCs was evaluated and the PT-enhanced CDT of tumors could fully destroy the tumors in mice on the 5th and 9th days post-injection of PSAF NCs with laser irradiation [116].

As a representative Fe-based Fenton nanocatalyst in CDT, Liu et al. developed a novel all-in-one ABTS-Fe/PVP (AFP) NP in which $Fe^{3+}$ and 2,2-azino-bis (3-ethylbenzothiazoline-6-sulfonic acid) (ABTS) were dissolved in methanol, and the resulting solution mixed with polyvinylpyrrolidone (PVP) as a new CDT agent (AFP NP) for PAI-guided PT-enhanced CDT (Fig. 7b, c). ABTS is water-soluble horseradish peroxidase (HRP) substrate that can be catalyzed by HRP in the presence of $H_2O_2$ to generate its green oxidized form (oxABTS), which exhibits high absorption in the NIR region. PVP is a water-soluble polymer that coordinates to $Fe^{3+}$ and $Fe^{2+}$. The AFP NPs exhibit a sphere-like morphology with an average size of 242.3 nm and a zeta potential of −12.2 mV. The $Fe^{3+}$ in the AFP NPs can produce •OH and deplete GSH in the presence of $H_2O_2$, demonstrating that AFP NPs can increase intracellular oxidative stress. The PA images and signals were observed at different time points post-injection of the AFP NPs and the PA signals gradually increase at the tumor site, demonstrating the rapid accumulation of AFP NPs at the tumor site through the enhanced permeability and retention (EPR) effect (Fig. 7d). To investigate the PT effect of AFP NPs, the tumor temperature of the AFP NPs was rapidly increased to 47.7 °C after laser irradiation, which was sufficient to kill the tumor, confirming that the AFP NPs show superior tumor-growth inhibition efficacy because of their efficient CDT through the simultaneous generation of •OH and depletion of GSH [118]. In a similar study, Shi et al. successfully prepared molybdenum (Mo)-based polyoxometalate (POM) cluster doped with Fe (Fe-POM) as an intelligent theranostic agent for PT-enhanced CDT in the NIR-II

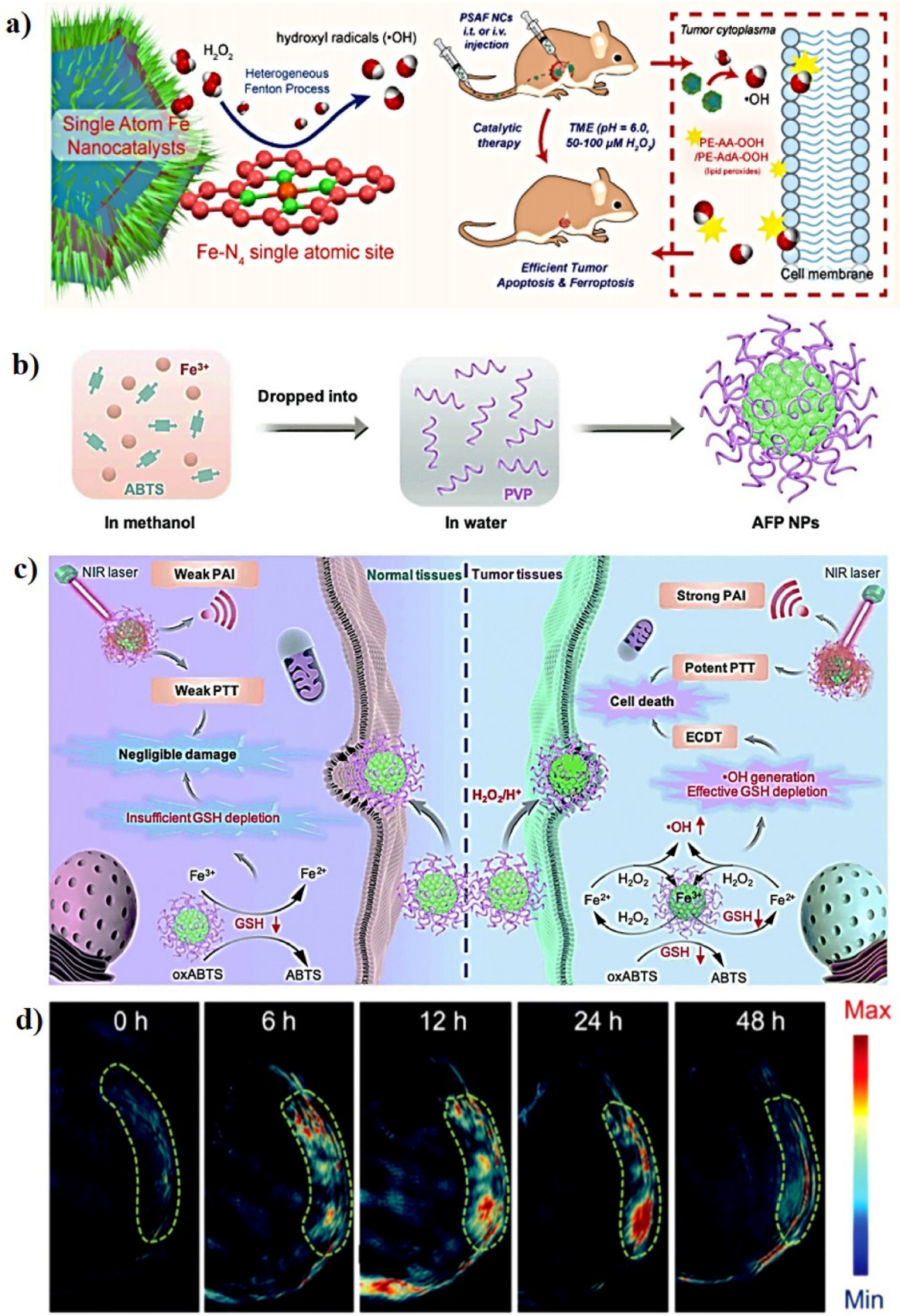


**Fig. 7.** (a) A schematic illustration of the preparation of PSAF NCs for PT-enhanced CDT. Reprinted with permission of Ref. [116]. Copyright 2019 American Chemical Society. (b) A schematic illustration of the synthesis procedure for AFP NPs. (c) Proposed mechanism for AFP NPs in the PT-enhanced Fenton-based CDT of tumor and normal tissues. (d) *In vivo* PA signals of the tumor area at various time points after intravenous injection of AFP NPs. Reprinted with permission of Ref. [118]. Copyright 2020 Royal Society of Chemistry.

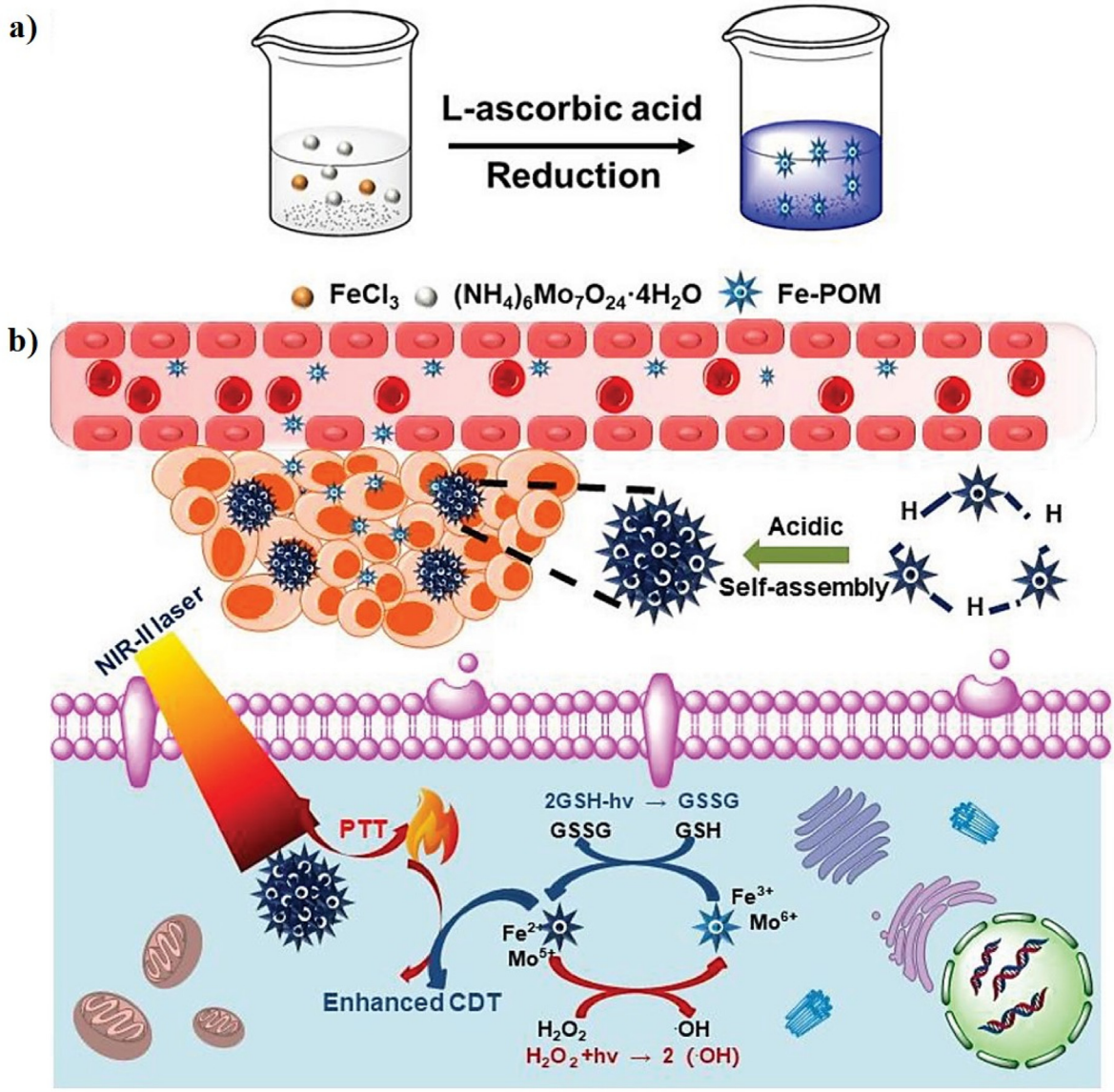


**Fig. 8.** A schematic illustration of the synthesis of Fe-POM (a) and (b) the synergistic mechanism of as-prepared Fe-POM applied in combination therapy. Reprinted with permission of Ref. [123]. Copyright 2020 Wiley.

window (Fig. 8a, b). POM clusters were prepared via a facile synthesis procedure and $FeCl_3$ and L-ascorbic acid were added to the POM solution to form Fe-POM. The Fe-POM had a highly uniform size and morphology with ultra-small diameters of 12.9 nm. The PCE ($\eta$) of Fe-POM was calculated to be 51.4%, suggesting the PT heating ability of Fe-POM in the NIR-II window. $Fe^{2+}$ and $Mo^{5+}$ can trigger the Fenton reaction, which can convert $H_2O_2$ into harmful •OH in the presence of Fe-POM and simultaneously deplete GSH for amplified CDT efficiency, confirming that Fe-POM can significantly improve the PT-catalytic efficacy. This PT effect can further improve the CDT effect, thereby achieving the synergistic effect of PT-enhanced CDT, which can effectively cause cancer cell death *in vitro* and fully inhibit the tumor *in vivo*. To obtain a more precise combination of PTT/CDT, PAI guidance will be beneficial for tracking the time-dependent tumor retention of Fe-POM. The PA signal observed at the tumor site gradually increases 2 h post-injection of Fe-POM, suggesting the rapid accumulation of Fe-POM in the tumor area [123].

In another example, Hu and co-workers successfully synthesized PB NCs and achieved the *in situ* reductions of FePt NPs, followed by coating with PEG and hyaluronic acid (HA) (PB@FePt-HA-*g*-PEG) for triple-modal imaging-guided PT-enhanced CDT (Fig. 9a). PB NCs have been used as new photo-absorbing agents for photothermal ablation therapy. FePt NPs can act as ferroptosis agents and have been used in MRI and CT imaging diagnoses. HA has been used as a specific targeting agent for cancer therapy. PEG is a synthetic polymer that can be used as a coating material on the surface of PB@FePt. The PB NCs have a nanocube structure with a hydraulic diameter of 150 nm. The PCE ($\eta$) of PB@FePt-HA-*g*-PEG was calculated to be 28.14%, implying that PB@FePt-HA-*g*-PEG possessed a good PT conversion ability. PB@FePt-HA-*g*-PEG shows a strong synergistic effect on cancer cell inhibition *in vitro*. PB@FePt-HA-*g*-PEG has been used in tri-model imaging diagnosis (MRI/CT/PT imaging) (Fig. 9b–d). Tumor-bearing mice were scanned using an MR, CT, and near-infrared (IR) thermal imaging system post-injection of PB@FePt-HA-*g*-PEG. The MR and CT signals of the tumor site increase significantly, suggesting that PB@FePt-HA-*g*-PEG has the potential to serve as an efficient CT/MR contrast agent for PT-enhanced CDT. The PT imaging ability of PB@FePt-HA-*g*-PEG was also investigated and the thermal signal of the tumor became dark red after laser irradiation, implying that the PB@FePt-HA-*g*-PEG can serve as a PT imaging agent. PB@FePt-HA-*g*-PEG can effectively catalyze the conversion of $H_2O_2$ in tumor-bearing mice into harmful •OH, which can effectively inhibit tumor growth

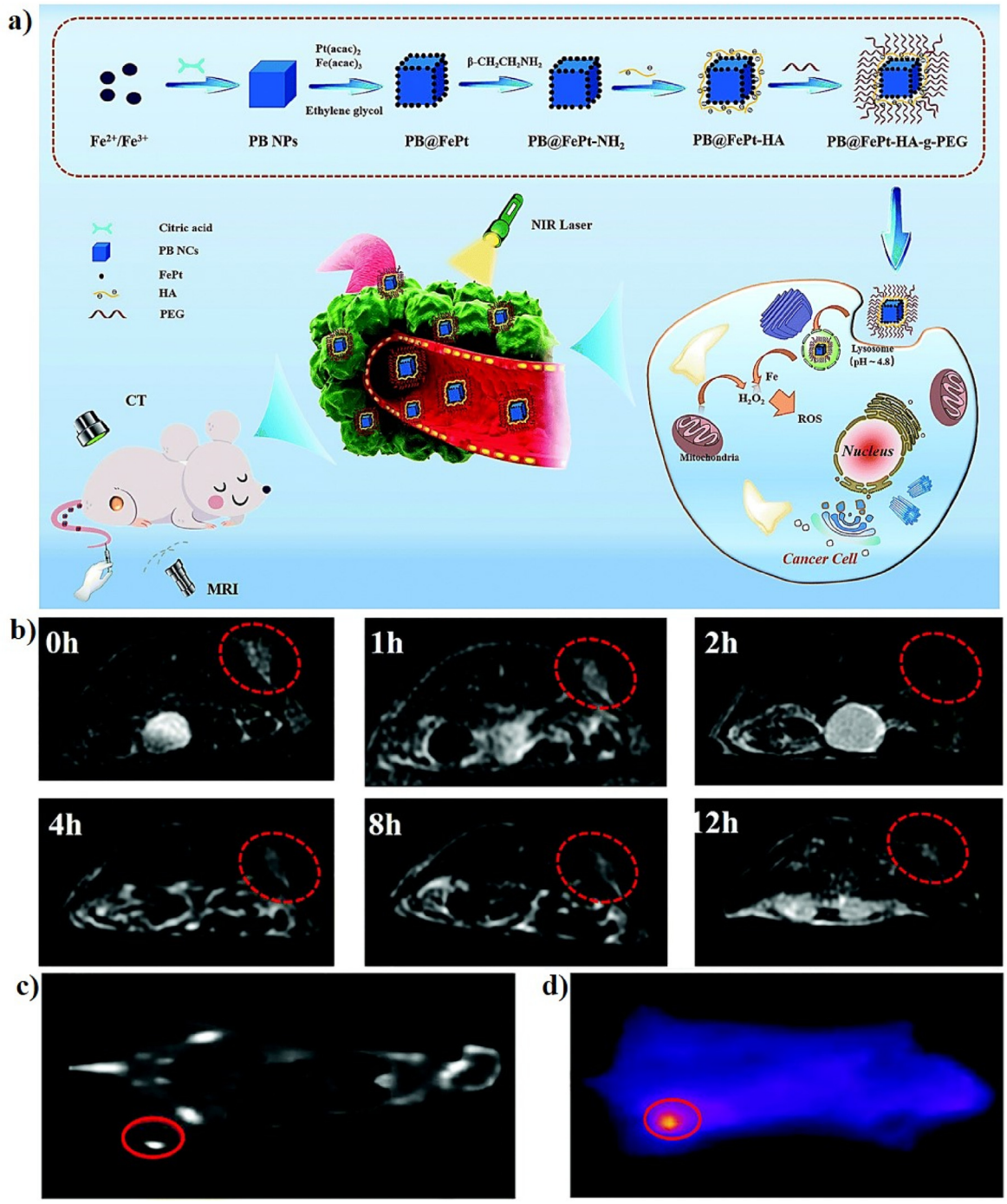


**Fig. 9.** (a) A schematic illustration of the synthetic process used to construct PB@FePt-HA-*g*-PEG for PT-enhanced CDT. (b) *In vivo* MR images of tumor-bearing mice at various time points post-injection of PB@FePt-HA-*g*-PEG. (c) CT image of tumor-bearing mice injected with PB@FePt-HA-*g*-PEG. (d) IR thermal image of tumor-bearing mice injected with PB@FePt-HA-*g*-PEG. Reprinted with permission of Ref. [124]. Copyright 2020 Royal Society of Chemistry.

under laser irradiation, implying that the PT-enhanced CDT effect of PB@FePt-HA-*g*-PEG effectively kills the cellular structure and promotes tumor ablation [124].

As a typical application, Chen et al. reported, for the first time, the use of biodegradable Fe-doped molybdenum oxide ($MoO_\chi$) ultra-fine nanowires (FMO) as Fenton reagents for PT-enhanced CDT. The FMO was synthesized using a single solvothermal technique and modified with PEG-4000. The ultra-fine FMO nanowires had a uniform thickness and lengths of ~450 nm. The PCE ($\eta$) of FMO reached 48.5% under 808 nm laser irradiation, implying that FMO has outstanding PEC and thus strong potential as a PT agent for CDT. The *in vitro* synergistic therapeutic effect of FMO on tumor cells was evaluated. The $Fe^{2+}$ and $Mo^{5+}$ in the FMO can effectively catalyze the decomposition of $H_2O_2$ and generate •OH *via* the Fenton reaction, and subsequently, the intracellular GSH can also be depleted, which may further enhance tumor cell death. The FMO-treated cells were co-stained and observed under a fluorescence microscope. The FMO + $H_2O_2$ + laser showed a strong red fluorescence, indicating that the synergistic therapeutic effect of •OH and PT heat had an improved killing efficacy on tumor cells. The tumor-bearing mice were scanned before and after the intratumoral injection of FMO, and the MR signal was observed at the tumor site, indicating that the FMO can be applied as a potential contrast agent for $T_1$-weighted MRI. The tumor temperature

in mice injected with the FMO solution was increased up to 50 °C upon laser irradiation for 10 min and the treated tumors completely disappeared within 15 days, indicating that FMO has great potential for use in MRI-guided PT-enhanced CDT [125].

Recently, Zhao and co-workers reported the use of $Fe_3O_4$ magnetic NPs and bismuth trisulfide ($Bi_2S_3$) integrated virus-like $Fe_3O_4$@$Bi_2S_3$ nanocatalysts (F-BS NCs) modified with BSA (F-BSP NCs) for PT-enhanced CDT. $Bi_2S_3$ has been used as a PT agent for PTT because of its excellent *in vivo* biocompatibility, stability, and high PCE, and ease of synthesis. $Fe_3O_4$ magnetic NPs exhibit peroxidase-like activity. The $Fe_3O_4$ magnetic NPs were synthesized using a simple hydrothermal technique, which was dispersed in a thioacetamide (TAA) and $Bi(NO_3)_3$ solution under ultrasonication to form virus-like $Fe_3O_4$@$Bi_2S_3$ (F-BS NCs) and then modified with BSA (F-BSP NCs) to enhance their stability and *in vivo* biocompatibility. The $Fe_3O_4$ NPs have an average diameter of 80 nm. The zeta potentials of F-BS NCs and F-BSP NCs were −8.05 and −17 mV, respectively. The PCE ($\eta$) of the F-BS NCs was 23.46%. The $Fe^{2+}$ ions in the F-BSP NCs react with $H_2O_2$ to produce highly toxic •OH via a mild PT effect and sequential Fenton reactions, which can further improve the CDT effect. The *in vitro* anticancer therapeutic efficacy of F-BSP NCs shows the highest apoptosis and necrosis after laser irradiation. The *in vivo* therapeutic ability and PAI performance of F-BSP NCs were further investigated in tumor-bearing mice. The tumor temperature of the F-BS NCs reached 59.1 °C upon laser irradiation and the treated tumor almost disappeared after 14 days of treatment, suggesting that the synergistic PT-enhanced CDT has an excellent therapeutic effect. The F-BS NCs also showed a clear PA signal in the tumor after intratumoral injection, confirming that the F-BS NCs can serve as ideal diagnostic PAI agents for diagnosis and treatment [128].

### 3.2. Copper-based nanomaterials for PT-enhanced CDT

Recently, copper-based nanomaterials have found many applications in a variety of research fields in CDT as potential alternatives for iron-based nanomaterials with promising developments and progress [99]. Copper (Cu) ions can also drive the Fenton-like reactions that prompt the decomposition of $H_2O_2$ to produce •OH to induce cancer cell apoptosis [36,38]. More importantly, CDT triggered by copper ions can start under neutral and very mild acidic conditions, which accurately matches the TME [56]. Cu-based nanomaterials are currently explored as new PT agents due to their low biotoxicity, easy fabrication, and low cost [61]. For example, Liu et al. reported, for the first time, the use of trithiol-terminated poly-(methacrylic acid) (PTMP-PMAA)-modified copper(I) phosphide nanocrystals (CP NCs) for MRI-guided PT-enhanced CDT (Fig. 10a). Cu(I) phosphide was synthesized from Cu(II) chloride dehydrate ($CuCl_2{\cdot}H_2O$) and triphenyl phosphite (TPOP) at high temperature to form $Cu_3P$, which was then coated with PTMP-PMAA to form the CP NCs to enhance their hydrophilicity. The CP NCs exhibit a hexagonal morphology with an average particle size of ~22 nm. The temperature of the CP NC aqueous solutions reached 51 °C after 10 min of

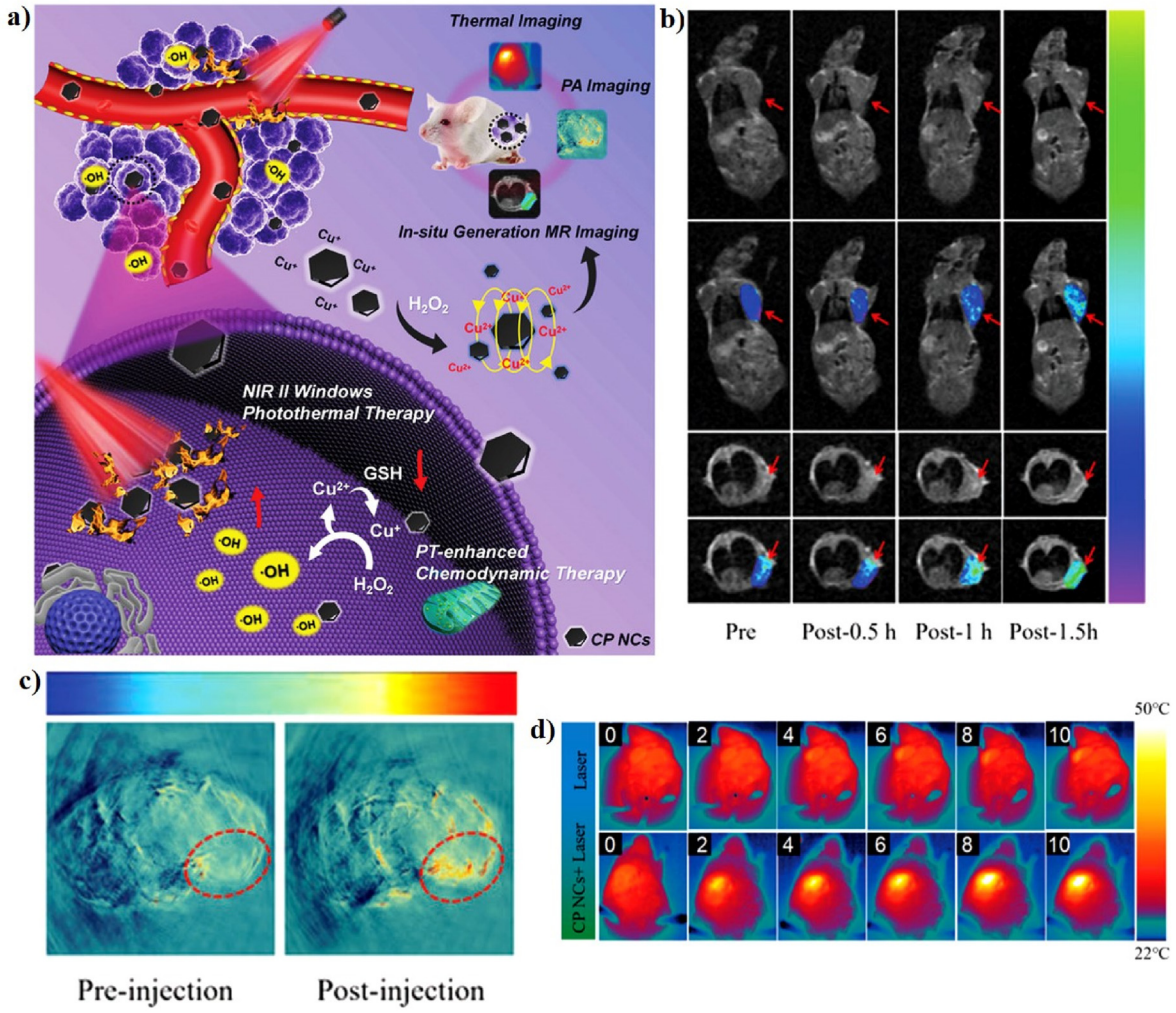


**Fig. 10.** (a) A schematic illustration of the synthesis of CP NCs and their application in synergistic combination therapy. *In vivo* $T_1$-MR (b) and PA (c) imaging of tumor-bearing mice. (d) *In vivo* IR thermal images of tumor-bearing mice. Reprinted with permission of Ref. [130]. Copyright 2019 Wiley.

laser irradiation, suggesting that the CP NCs have excellent PT properties. The PCE ($\eta$) of the CP NCs was determined to be 27%, which can further improve the Fenton-like reaction. The MR and PA imaging properties were investigated *in vitro* and *in vivo*. The $T_1$-MR signal of the tumor region was significantly enhanced after injection of the CP NCs, indicating that CP NCs can be used as a new *in situ* self-generation MRI contrast agent (Fig. 10b). The PA signal in the tumor area was notably enhanced 12 h post-injection of the CP NCS, indicating the potential PA imaging ability of CP NCs (Fig. 10c). The Cu(I) on the surface of CP NCs is more effective in the weakly acidic TME with a high production of •OH and triggers the apoptosis of cancer cells, suggesting that CP NCs have excellent •OH generation capability with the help of 1064 nm laser irradiation. The *in vivo* synergistic therapeutic effect of CP NCs on U14 tumor-bearing mice was confirmed using IR thermal camera (Fig. 10d). The tumor temperature of mice injected with the CP NC solution was increased up to 48 °C upon 1064 nm laser irradiation and tumor growth was significantly inhibited on the 5th day. Furthermore, the excess GSH in the TME can further reduce the Cu(II) produced by the Fenton-like catalytic reaction to Cu(I), enhancing the production of •OH, indicating that the CP NCs have great potential for use in MRI/PAI-guided PT-enhanced CDT [130].

Cu-based nanomaterials have become research hotspots in the field of biomedicine in recent decades because of their excellent photothermal conversion efficiency, biocompatibility, and Fenton-like properties [65]. Compared with other copper-based nanomaterials, copper selenide ($Cu_2Se$) nanomaterials are particularly interesting due to their strong absorption in NIR window and Fenton-like properties, and Cu and selenium (Se) are considered as important trace elements in the human body [157,158]. For example, Wang and co-workers successfully synthesized PEG-coated copper selenide ($Cu_2Se$) hollow nanocubes (HNCs) as a promising catalyst for PT-enhanced CDT (Fig. 11a, b). The HNCs were prepared via an anion exchange method using $Cu_2O$ nanocubes and then modified with thiolated PEG to enhance the stability and dispersibility (PEG-$Cu_2Se$ HNCs). The PEG-$Cu_2Se$ HNCs show excellent biocompatibility, high PCE, and strong Fenton-like catalytic properties. The $Cu_2Se$ HNCs have a regular cubic morphology with an average diameter of 86.89 ± 19.93 nm. The PCE ($\eta$) of the $Cu_2Se$ HNCs was 50.89% in the NIR-II window, which was significantly higher than that of commonly reported photothermal agents, such as Au–$Cu_9S_5$ NPs (37%) [159] and $Cu_3BiS_3$ nanorods (40.7%) [160]. *In vitro* synergistic treatment with PEG-$Cu_2Se$ HNCs + $H_2O_2$ + laser irradiation had a significant inhibitory effect on 4T1 cells. The strong NIR absorbance of the PEG-$Cu_2Se$ HNCs indicates their potential for use in PAI. A strong PA signal was observed at the tumor site after injection of PEG-$Cu_2Se$ HNCs, suggesting that the PEG-$Cu_2Se$ HNCs can serve as an outstanding agent for PAI. The PEG--$Cu_2Se$ HNCs exhibit a strong Fenton-like reaction rate in the presence of $H_2O_2$, which can produce a large amount of •OH and significantly improve the therapeutic efficacy of the Fenton-like catalyst to produce •OH, indicating that the mild PT effect with CDT can completely eradicate tumors [41].

In another study, An et al. reported $Cu^{2+}$-doped zeolitic imidazolate framework-8-coated polydopamine (PDA) NPs (PDA@Cu/ZIF-8 NPs) for GSH-triggered and PT-enhanced CDT (Fig. 11c, d). PDA NPs were synthesized via solution-phase oxidation and Cu/ZIF-8 was coated on the surface of PDA to achieve highly uniform PDA@Cu/ZIF-8. PDA acts as a PT agent that can produce heat under laser irradiation to generate •OH and deplete GSH, which significantly retards the growth of xenograft tumors. PDA NPs have an average diameter of 50 nm. The temperature of the PDA@Cu/ZIF-8 NP solutions increases to 70 °C after 10 min of laser irradiation, indicating their potential as a PT agent. The *in vitro* anticancer effect of PDA@Cu/ZIF-8 NPs resulted in increased cell death after laser irradiation, implying that the rationally designed PDA@Cu/ZIF-8 NPs for new PTT/CDT treatment can serve as a novel anticancer agent. The synthesized PDA@Cu/ZIF-8 NPs can react with intracellular GSH to simultaneously deplete GSH. In addition, $Cu^{+}$ decomposes $H_2O_2$ to produce a large amount of •OH via Fenton-like reactions, which can be further enhanced by the PT effect, causing GSH-controlled ROS generation and GSH depletion in the tumor area. The *in vivo* PT-enhanced CDT results suggest that PDA@Cu/ZIF-8 NPs exhibit excellent tumor-killing ability [72].

Currently, copper-oxide ($Cu_2O$) nanocrystals have been reported to have a variety of morphologies, including spheres, nanocubes, triangular nanoplates, and octahedrons [161–163]. More interestingly, the truncated octahedron is considered an excellent candidate for the Fenton-like catalytic activity [132]. Similarly, Li et al. developed a triphenylphosphonium (TPP)-conjugated gold-coated copper(II)-based truncated octahedron (CuO@AuCu-TPP) as a Fenton-like catalyst for PA/CT imaging-guided PT-enhanced CDT (Fig. 12a). $Cu_2O$ was prepared by reducing a solution of copper citrate complexed with ascorbic acid and the Au NPs were then covered on the surface of the $Cu_2O$ via a disproportional reaction. Finally, the TPP as a targeting group was conjugated at the end through electrostatic interactions to form CuO@AuCu-TPP. The CuO@AuCu-TPP showed a truncated octahedral structure, with an average particle size of 255 nm and a zeta potential of −7 mV. The PCE ($\eta$) of CuO@AuCu-TPP with 808 nm laser irradiation was calculated to be 37.9%, indicating its outstanding PT properties. Cu(II) was reduced to Cu(I) because of the intracellular GSH, which simultaneously depletes GSH, and Cu (I) can react with $H_2O_2$ to disrupt the redox balance in the mitochondria via •OH generation and GSH consumption via Fenton-like reactions. The *in vitro* anticancer efficacy of CuO@AuCu-TPP significantly inhibited HeLa cell viability under laser irradiation, indicating that PT heat can effectively enhance the efficiency of •OH generation. The *in vivo* synergistic therapeutic efficacy of Au on the surface of CuO@AuCu-TPP showed an excellent PT effect upon laser irradiation, which causes the tumor temperature to increase and enhance the speed of the Fenton-like reaction, thus enabling a synergistic PT effect, Fenton-like reaction, and accurate mitochondrial-targeting ability to achieve strong therapeutic effects (Fig. 12b). In addition, PA and CT images were obtained in mice and strong PA and CT signals at the tumor site were observed 6 h post-injection, indicating that CuO@AuCu-TPP shows great promise for therapeutic application in cancer diagnostics (Fig. 12c, d) [132].

In addition, copper sulfide (CuS) NPs can be used as a theranostic agent because of their PT, PA, and Fenton-like properties [70]. For example, Wang et al. developed hollow and solid copper sulfide NPs ($Cu_9S_8$ NPs) as a Fenton-like agent for PT-enhanced CDT (Fig. 13a). The copper sulfide NPs have a hollow sphere structure with an average diameter of ~18.05 nm and shell thickness of ~3.50 nm. The hollow $Cu_9S_8$ NPs show excellent chemodynamic treatment effects for cancer, both *in vitro* and *in vivo,* due to the •OH generated from endogenous $H_2O_2$ under the catalytic conditions of copper ions. Subsequently, the mild temperature generated from the PT effects can effectively improve the CDT efficacy. 4T1 tumor-bearing mice were intravenously injected with $Cu_9S_8$ NPs at various time points and the PA images of the tumor site slowly changed from black to blue over 2–4 h (Fig. 13b, c), suggesting an increase in the signal strength, which can be used to provide useful information for guiding PT-enhanced CDT [64]. In another study, Sun et al. developed a NIR-II PT Fenton-like nanocatalyst (PFN), consisting of human serum albumin (HSA), manganese dioxide ($MnO_2$), and copper sulfide (CuS) for MRI-guided PT-enhanced CDT (Fig. 13d). PFN was synthesized using a two-step technique. HAS-encapsulated $MnO_2$ NPs were prepared using a redox reaction and the CuS NPs were deposited via a biomimetic mineralization process to form PFN. CuS NPs are promising Fenton-like nanocatalysts that react with $H_2O_2$ to generate •OH for PT-enhanced CDT. The $MnO_2$ NPs decompose into $Mn^{2+}$, which is a prominent imaging agent for $T_1$-weighted MRI. The PFN generates local

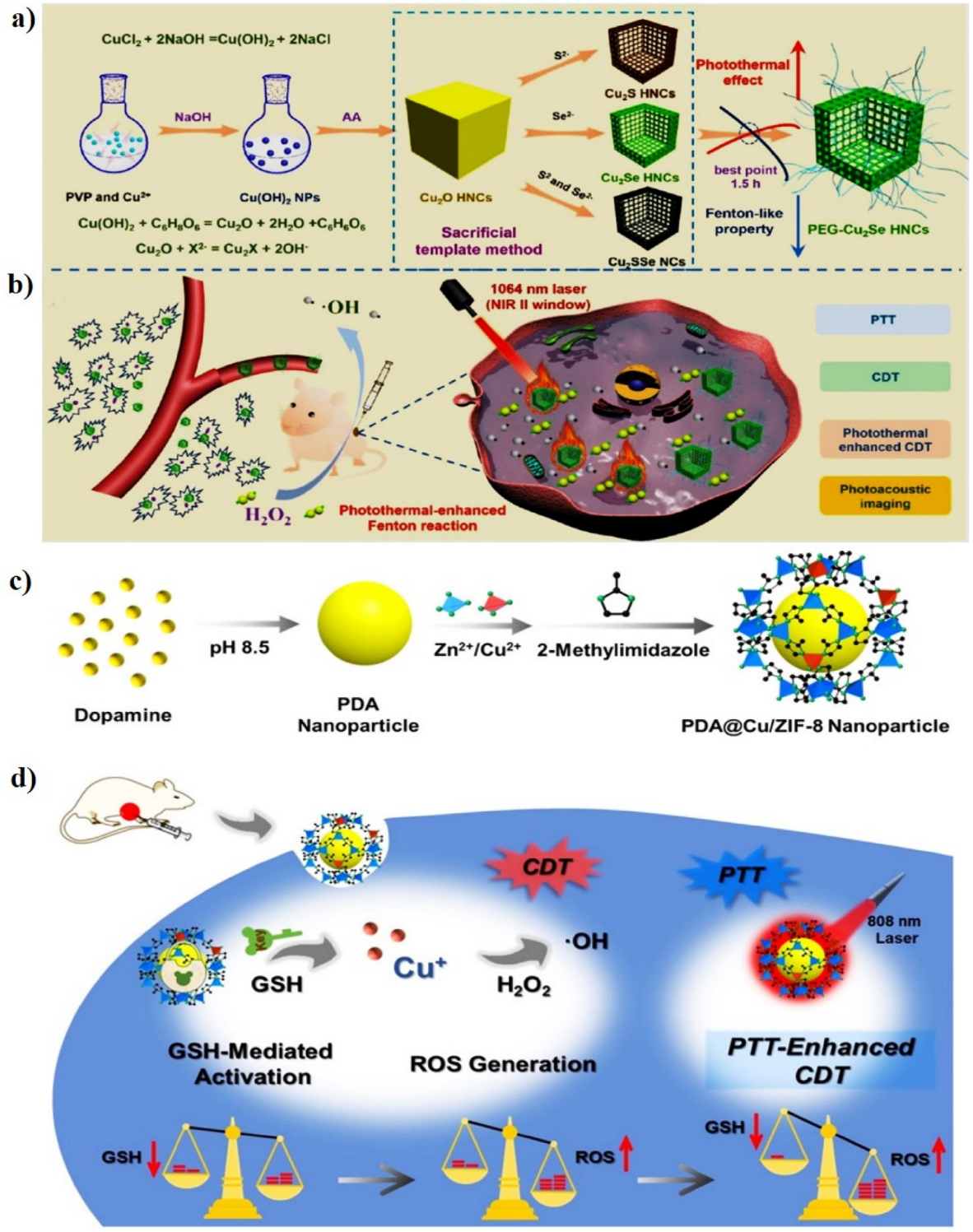


**Fig. 11.** (a) A schematic illustration of the preparation of PEG-$Cu_2Se$ HNCs. (b) Proposed mechanism of PEG-$Cu_2Se$ HNCs for PT-enhanced CDT in the NIR-II window. Reprinted with permission of Ref. [41]. Copyright 2019 American Chemical Society. A schematic illustration of the synthesis of PDA@Cu/ZIF-8 NPs (c) and its application in combination therapy (d). Reprinted with permission of Ref. [72]. Copyright 2020 Elsevier Ltd.

heat under 1064 nm laser irradiation, which accelerates the Fenton-like reactions. The particle size of PFN was 22 nm and its zeta potential was −18.7 mV because of the negative charge of CuS. The PCE ($\eta$) of PFN was 30.17%, implying that it is a good PT agent. The *in vitro* anticancer efficacy of PFN + $H_2O_2$ + laser irradiation showed the highest level of apoptotic cells, implying synergistic NIR-II PTT and CDT. The tumor temperature of mice injected with PFN gradually reached 55 °C after 5 min under laser irradiation and the treated tumor was completely inhibited without any reoccurrence, implying that the PFN shows superior PT-heating ability and potent antitumor efficiency *in vivo*. The MR signal in the tumor regions reached its brightest at 30 min post-injection of PFN, indicating the effective accumulation of PFN in tumors and demonstrating their, utility as an activatable MRI contrast agent for cancer therapy (Fig. 13e) [135].

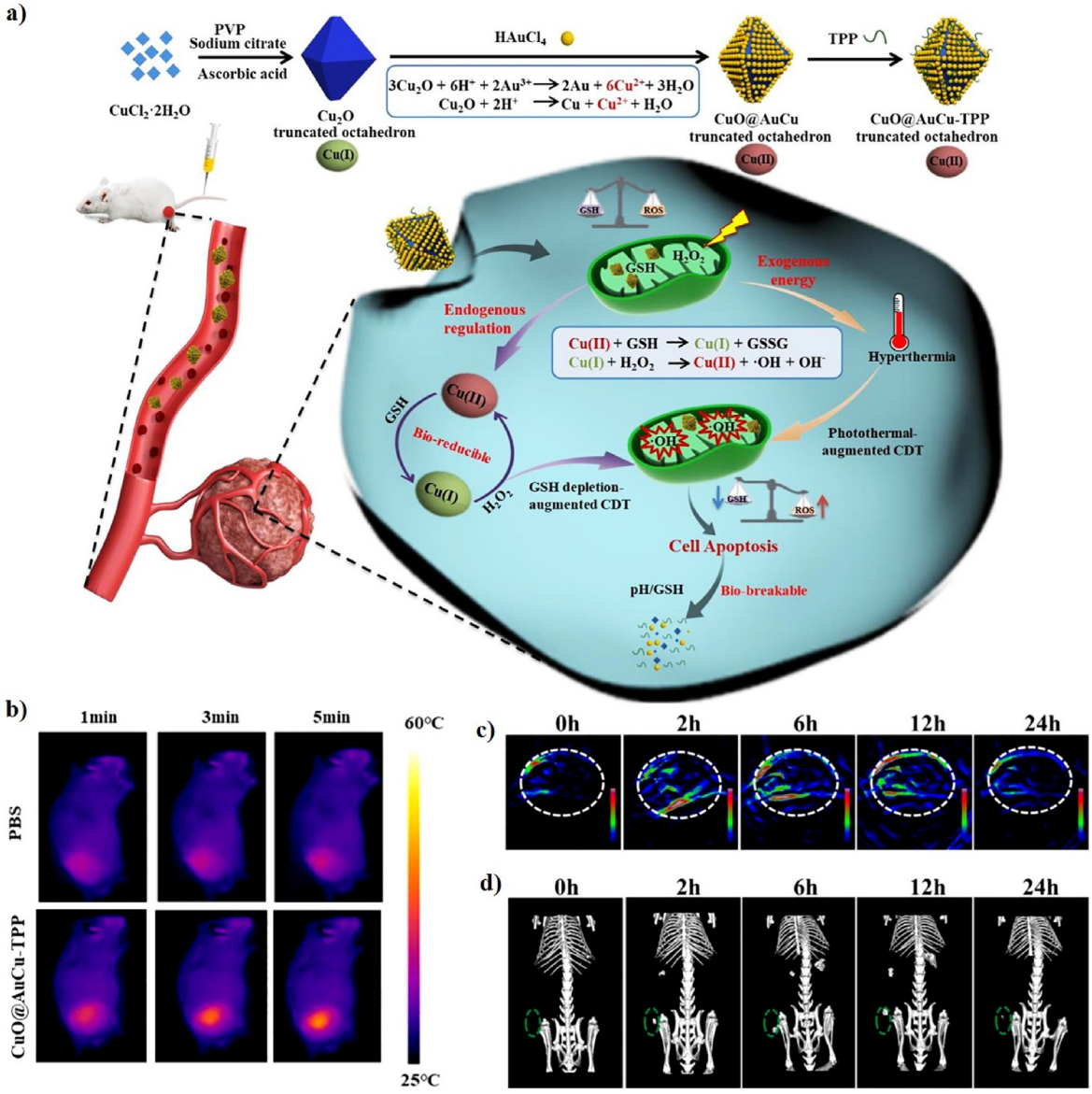


**Fig. 12.** (a) A schematic illustration of the synthesis of CuO@AuCu-TPP and the therapeutic mechanism of CuO@AuCu-TPP. (b) IR thermal images of mice. *In vivo* PA (c) and CT (d) images post-injection of CuO@AuCu-TPP. Reprinted with permission of Ref. [132]. Copyright 2020 Elsevier Ltd.

### 3.3. Gold-based nanomaterials for PT-enhanced CDT

Gold-based nanomaterials are the most well-studied nanomaterials for biomedical applications, such as biosensors, therapy, and multimodal imaging [164–170]. Many researchers are currently using gold-based nanomaterials as enzyme mimetics and have greatly expanded the number of new therapeutic applications derived from their enzyme-like functions [171,172]. Gold-based nanomaterials have been used in a variety of research fields in PT-enhanced CDT because of their strong NIR absorption and inherent catalytic properties [137,173]. For example, Fan et al. reported novel nanozymes with a yolk-shell structure in which the gold (Au) NP core was coated with a hollow carbon nanosphere with a porous shell (Au@HCNs) for PT-catalytic therapy. Au NPs have been one of the most widely studied nanozymes in recent years that generate ROS because of their intrinsic enzyme-like activities, and they are also good NIR-absorbing agents. AuNPs were synthesized according to a literature method and then coated with $SiO_2$ using the Stöber method, yielding $Au@SiO_2$ NPs. PDA was polymerized on the surface of $Au@SiO_2$, yielding $Au@SiO_2$@PDA NPs, which were carbonized under a $N_2$ atmosphere for 2 h at 800 °C and named as Au@HCNs. The Au@HCNs have an average size of 275 ± 0.355 nm and a PCE value ($\eta$) of 26.8%. The enzyme-like activity of Au@HCNs can produce ROS, such as •OH and superoxide radicals ($\bullet O_2^-$), and PT heat can improve the generation of ROS to accelerate the enzymatic reactions. The *in vitro* anticancer effect of Au@HCNs significantly inhibits the growth of cancer cells after laser irradiation and generates ROS, inducing cell death. The temperature of Au@HCNs-treated tumors rapidly increases from 33 to 52.9 °C under laser irradiation for 10 min, leading to their complete disappearance without recurrence after treatment. Au@HCNs can react with $H_2O_2$ and $O_2$ in the TME to produce toxic ROS, resulting in cell death, which may be enhanced by the mild PT effect [137].

### 3.4. Other metal oxide- and sulfide-based nanomaterials for PT-enhanced CDT

Several transition metals have also been used as Fenton-like agents for PT-enhanced CDT [107,174]. The tungsten trioxide ($WO_{3-x}$) has been used as a PT material for PTT because of its strong absorption in the NIR region and has also been used as a Fenton-like agent for CDT [107, 175–177]. In 2018, Liu et al. successfully prepared ultrasmall tungsten

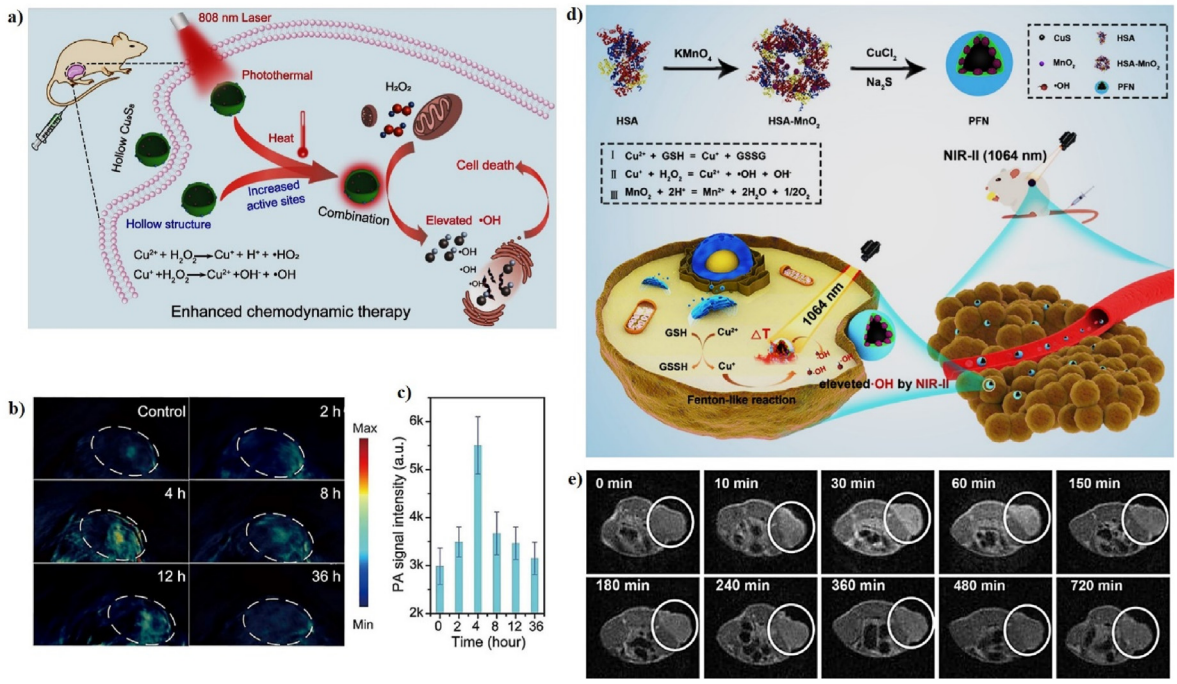


**Fig. 13.** (a) A schematic illustration of the fabrication of hollow $Cu_9S_8$ NPs for PT-enhanced CDT. *In vivo* PA images (b) and PA signal (c) of tumor-bearing mice before and after intravenous injection of hollow $Cu_9S_8$ NPs. Reprinted with permission of Ref. [64]. Copyright 2020 Elsevier Ltd. (d) A schematic illustration of PFN for PT-enhanced CDT. (e) *In vivo* $T_1$-weight MR images at different time points. Reprinted with permission of Ref. [135]. Copyright 2020 American Chemical Society.

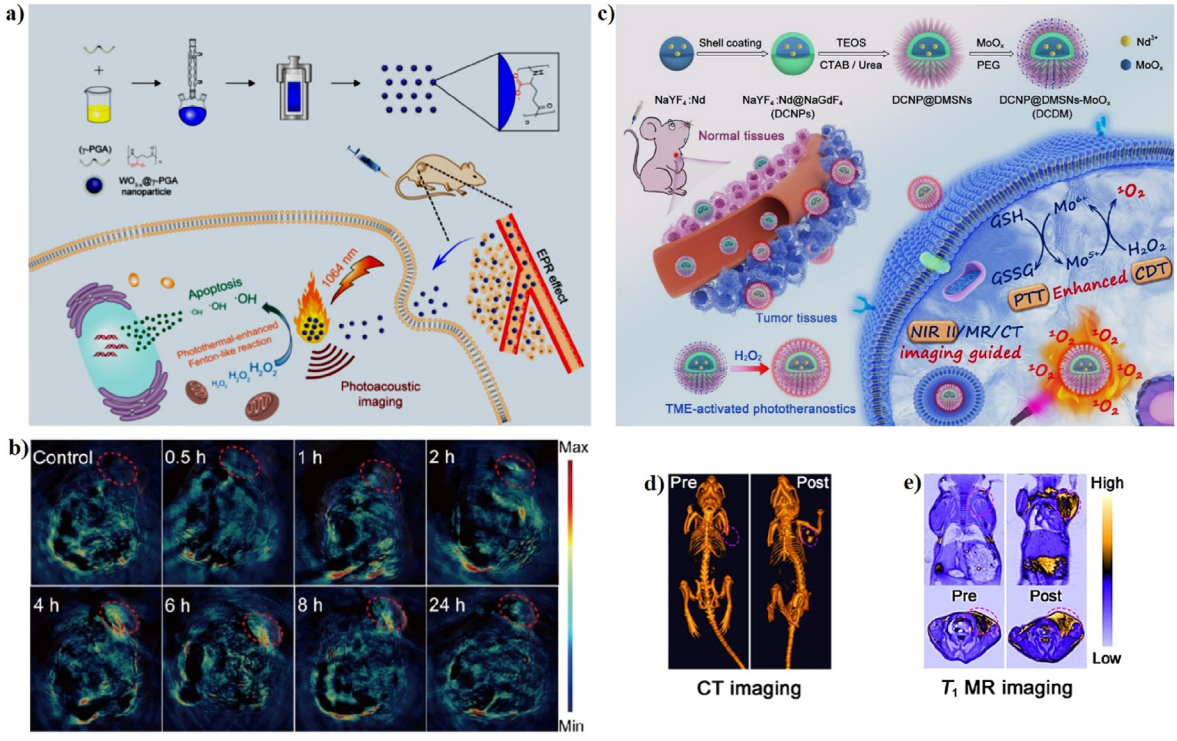


**Fig. 14.** (a) A schematic illustration of the synthesis of $WO_{3-x}$@γ-PGA NPs for PT-enhanced CDT. (b) *In vivo* PA imaging of tumor-bearing mice before and post-injection of $WO_{3-x}$@γ-PGA NPs. Reprinted with permission of Ref. [24]. Copyright 2018 American Chemical Society. (c) A schematic illustration of the synthesis of DCDMs for PT-enhanced CDT. *In vivo* CT (d) and MR (e) images of tumor-bearing mice before and post-injection of DCDMs. Reprinted with permission of Ref. [139]. Copyright 2020 American Chemical Society.

trioxide ($WO_{3-x}$) NPs, which were then coated with γ-poly-L-glutamic acid (γ-PGA) for PAI and effective PT-enhanced CDT (Fig. 14a). The $WO_{3-x}$@γ-PGA NPs were synthesized via a simple hydrothermal reaction using γ-PGA as a ligand and $WCl_6$ as the tungsten source. The $WO_{3-x}$@γ-PGA NPs have a monodispersed irregular morphology with an average particle size of 5.73 ± 0.93 nm. The 1064 nm laser PCE (η) of the

$WO_{3-x}$@γ-PGA NPs was 25.8%, as calculated from the heating and cooling curves. More importantly, the Fenton-like reaction occurred for $WO_{3-x}$@γ-PGA NPs in the presence of $H_2O_2$, indicating that the $WO_{3-x}$@γ-PGA NPs can react with $H_2O_2$ to generate a large amount of •OH; this Fenton-like reaction was promoted by the PT effect. Most of the cells were killed in the presence of $WO_{3-x}$@γ-PGA NPs + $H_2O_2$ + laser irradiation, which can be attributed to the *in vitro* PT-enhanced CDT. The tumors of mice in the presence of $WO_{3-x}$@γ-PGA NPs + laser irradiation gradually decrease and almost disappear after 18 days, indicating that $WO_{3-x}$@γ-PGA NPs can cure tumors after laser irradiation. PAI was employed to detect the accumulation of nanomaterials in the tumor areas to guide PT-enhanced CDT. 4T1 tumor-bearing mice were intravenously injected with the $WO_{3-x}$@γ-PGA NPs. PA images of the mice were scanned before and after injection at various time points (Fig. 14b). The strongest PA signal was observed at 4 h post-injection, suggesting that the $WO_{3-x}$@γ-PGA NPs have great potential for use in PAI [24].

Currently, molybdenum oxide NPs (MoOirst time, the use of biodegradable NPs) have aroused worldwide interest because of their excellent PT conversion efficiency and Fenton-like properties [178]. For instance, Dong et al. developed PEGylated down-conversion NPs (DCNPs) with dendritic mesoporous silica (DMSN) and then loaded ultra-small molybdenum oxide NPs (MoOirst time, the use of biodegradable NPs) as all-in-one nanotheranostic agents (PEG-DCNP@DMSN-MoOirst time, the use of biodegradable NPs) for multimodal imaging-guided PT-enhanced CDT (Fig. 14c). DCNP@DMSN had a uniform hexagonal structure with an average diameter of 123 nm. The PCE (η) of PEG-DCNP@DMSN-MoOirst time, the use of biodegradable NPs (DCDMs) was 51.5%, implying that the DCDMs possess excellent PT properties. $Mo^{5+}$ can efficiently catalyze the decomposition of $H_2O_2$ to form a considerable amount of singlet oxygen ($^1O_2$) in the mildly acidic TME, leading to irreversible cell death. Subsequently, the generated $Mo^{6+}$ can effectively decrease the levels of GSH in the tumor area, and the GSH depletion and PT effect can further accelerate the generation of $^1O_2$ and enhance CDT. The synergetic PT-enhanced CDT of DCDMs effectively inhibits apoptosis *in vitro* and killed the tumors *in vivo*. Moreover, the CT and MR signals of the tumor area 12 h post-injection were obviously higher than those prior to injection, implying that the DCDMs are multimodal imaging contrast agents for clinical diagnosis (Fig. 14d, e) [139].

As a representative manganese dioxide ($MnO_2$)-based Fenton nanocatalyst in CDT, Wang et al. designed a gold@manganese dioxide (Au@$MnO_2$) core-shell nanostructure for PAI/MRI-guided PT-enhanced CDT and GSH-triggered CDT. Au@$MnO_2$ has a uniform core-shell structure with an average size of ~25 nm. The PCE (η) of Au@$MnO_2$ after being triggered by GSH was 23.6%, demonstrating that Au@$MnO_2$ had good PT properties. The GSH-triggered and PT-enhanced CDT of Au@$MnO_2$ can efficiently catalyze the generation of •OH from $H_2O_2$ because of the high amount of $Mn^{2+}$ produced upon the reduction of $MnO_2$ by GSH and the PT effect can accelerate the production of •OH, indicating that Au@$MnO_2$ has promising potential as a GSH-triggered smart theranostic agent for PAI/MRI-guided PT-enhanced CDT. The *in vitro* and *in vivo* therapeutic effects of Au@$MnO_2$ with laser irradiation show the highest apoptosis and necrosis rates because of the synergistic effect of the GSH-triggered Au@$MnO_2$ agents for PT-enhanced CDT. The complementary effects of MRI and PAI can efficiently enhance the diagnosis of cancer. PA and $T_1$-weighted MR imaging of mice were performed at various time points post-injection of Au@$MnO_2$. The $T_1$-weighted MR signal was observed in the tumor area and the GSH-triggered PAI of Au@$MnO_2$ was similar to that of MRI, indicating that Au@$MnO_2$ has promising potential as a GSH-triggered smart theranostic agent for PAI/MRI-guided PT-enhanced CDT [43].

In another similar recent study, An et al. constructed PEG-decorated $MnO_2$@$HMCu_{2-x}S$ nanocomposites (HMCMs), consisting of manganese dioxide ($MnO_2$) and hollow mesoporous copper sulfide ($HMCu_{2-x}S$), for PT-enhanced CDT (Fig. 15a). The particle size of $MnO_2$ was 80 nm. The PCE (η) of HMCM was 22.3%, implying that HMCM has great potential as an ideal PT agent. $MnO_2$ reacts with GSH, converting Mn(IV) to Mn(II) to enhance the Fenton-like reaction with additional •OH produced due to the increased generation of $Mn^{2+}$ under laser irradiation. The *in vitro* therapeutic effect of HMCM with laser irradiation showed higher cytotoxicity to MCF-7 cells, which caused higher $Mn^{2+}$ accumulation in the cells, allowing for the Fenton-like reaction to accelerate endogenous $H_2O_2$ for a high level of ROS production. The *in vivo* anticancer effects of HMCMs with laser irradiation efficiently eliminate tumor growth and showed a high tumor inhibition rate of 75%, demonstrating that HMCMs have superior anticancer efficiency [46]. In addition, Wang et al. developed biodegradable cobalt sulfide ($CoS_2$) nanoclusters ($CoS_2$ NCs) for the PT-enhanced CDT of cancer cells via Fenton-like catalytic activity (Fig. 15b). Cobalt chalcogenides have received a lot of attention in the field of biomedicine because of their high PT properties, biological safety, and catalytic properties. The $CoS_2$ NCs were prepared via a simple one-pot solvothermal method using a cobalt and sulfur source. The $CoS_2$ NCs have a spherical morphology with an average diameter of 19.79 ± 5.2 nm. The PCE (η) of the $CoS_2$ NCs was 60.4%. The $CoS_2$ NCs can generate •OH in the presence of $H_2O_2$ and PT heat accelerates the efficacy of the Fenton-like reaction. The *in vitro* PT-enhanced CDT based on $CoS_2$ NCs was concentration-dependent, which can significantly improve their therapeutic effect on cancer. 4T1 tumor-bearing mice were injected with $CoS_2$ NCs and laser-irradiated, resulting in complete inhibition and no reoccurrence. In addition, strong PA signals were observed at the tumor site after injection of $CoS_2$ NCs, suggesting that $CoS_2$ NCs have excellent PAI ability [42].

## 4. Combination therapy

Monotherapies such as PTT, CDT, CHT, SDT, PDT, IMT, and ST, have been extensively used in preclinical and clinical studies, and many researchers have reported that monotherapy is not as effective as expected because of the development of resistance and side effects over a long-term period of treatment [179]. Combination therapy commonly refers to the simultaneous co-delivery of drugs or combined-therapeutic strategies in various forms for the effective treatment of cancer [68]. Combination therapy has attracted an increasing amount of clinical attention because of its superior advantages in overcoming the intrinsic drawbacks of monotherapy [90]. The combination of PT-enhanced CDT with CHT, SDT, PDT, IMT, and ST has emerged as a potential alternative to monotherapies due to their synergistic therapeutic effects [99]. In addition, monomodal imaging (e.g., PAI, FLI, MRI, and CT alone) has been widely studied in clinical disease diagnosis, but there are still some short-comings and unsolvable problems that need to be overcome in multimodal imaging (PAI/FLI/MRI/CT multimodal diagnostic imaging) techniques to provide information for the effective diagnosis of disease [180]. Multimodal imaging (PAI/FLI/MRI/CT multimodal diagnostic imaging-guided combination cancer therapy) is also essential for the early stage of diagnosis, prognosis, and therapeutic effects of the tumor, which play a major role in accurate biomedicine [52,181].

### 4.1. PT-enhanced CDT with CHT

CHT is a widely accepted method and has been proven successful in cancer treatment in a clinical setting, which is the first-line treatment of patients for the advanced stage of tumors and metastatic tumors [182,183]. CHT has also recently achieved remarkable clinical success in extending the lives of millions of patients, which has several unique advantages such as high efficiency, reliability, reduce pain, and convenience [184]. The use of chemotherapeutic agents is based on the basic principle of highly toxic compounds to inhibit tumor growth and metastasis [185]. Cancer cell apoptosis is also one of the main mechanisms by which chemotherapeutic agents kill cells [186]. However, the major drawbacks of CHT include CHT-resistance, limited dosage, non-specific distribution, low drug levels in the tumor tissues, and severe systemic toxicity, which are responsible for the inefficiency of CHT in patients [187–189]. Hence, minimizing the side effects of CHT agents

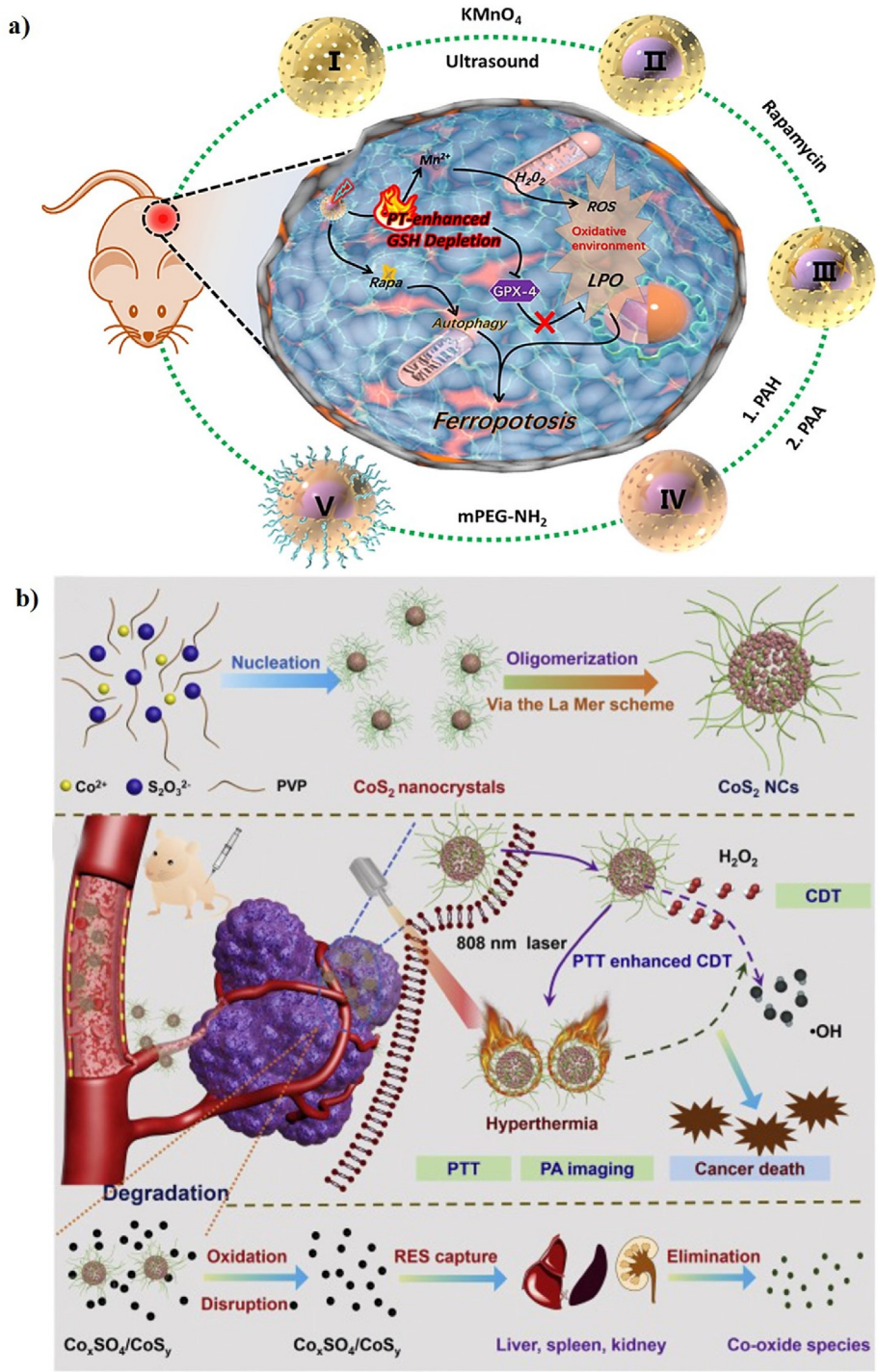


**Fig. 15.** (a) A schematic illustration of the synthesis and working mechanisms of HMCMs. Reprinted with permission of Ref. [46]. Copyright 2019 American Chemical Society. (b) A schematic illustration of the fabrication of $CoS_2$ NCs for PT-enhanced CDT. Reprinted with permission of Ref. [42]. Copyright 2020 Elsevier Ltd.

remains a challenge in the field of cancer CHT. PTT can effectively improve intracellular drug delivery, accelerate drug release, increase drug accumulation at the tumor site, and inhibit drug resistance [190, 191]. ROS also plays an important role in the redox balance of biological processes [192]. The high amount of ROS in cancer cells can effectively increase the oxidative damage of cancer cells and enhance the delivery efficiency, thereby resulting in cell death [193]. Therefore, the integration of anticancer drugs and PT-enhanced Fenton-based nanocatalysts into one nanomaterial is highly desirable and PT-enhanced CDT with CHT has demonstrated to be have great potential to overcome the side effects, thus achieving synergistic cancer therapy [194].

In a similar study, Qi et al. reported a multifunctional carbon dot (CD)-decorated silver (Ag)/gold (Au) bimetallic nanoshell (NS) as a smart nanozyme (CDs-Ag/Au NS, CAANS) for chemo-PTT. The CD-loaded Ag/Au NSs were proven conducive to generating toxic ROS to stimulate CHT. The CAANSs have an average size of 52 nm. Tryptophan (Trp) plays an important role in oxidative stress by inducing the formation of ROS such as superoxide radicals ($\bullet O_2^-$), which are decomposed to produce $H_2O_2$ in cancerous cells under the PT catalytic process in the presence of CAANSs and effectively kill cancer cells. The apoptosis rate was 95%, suggesting that CAANS can serve as an effective catalytic nanomedicine for cancer therapy [136]. In another study, Wang et al.

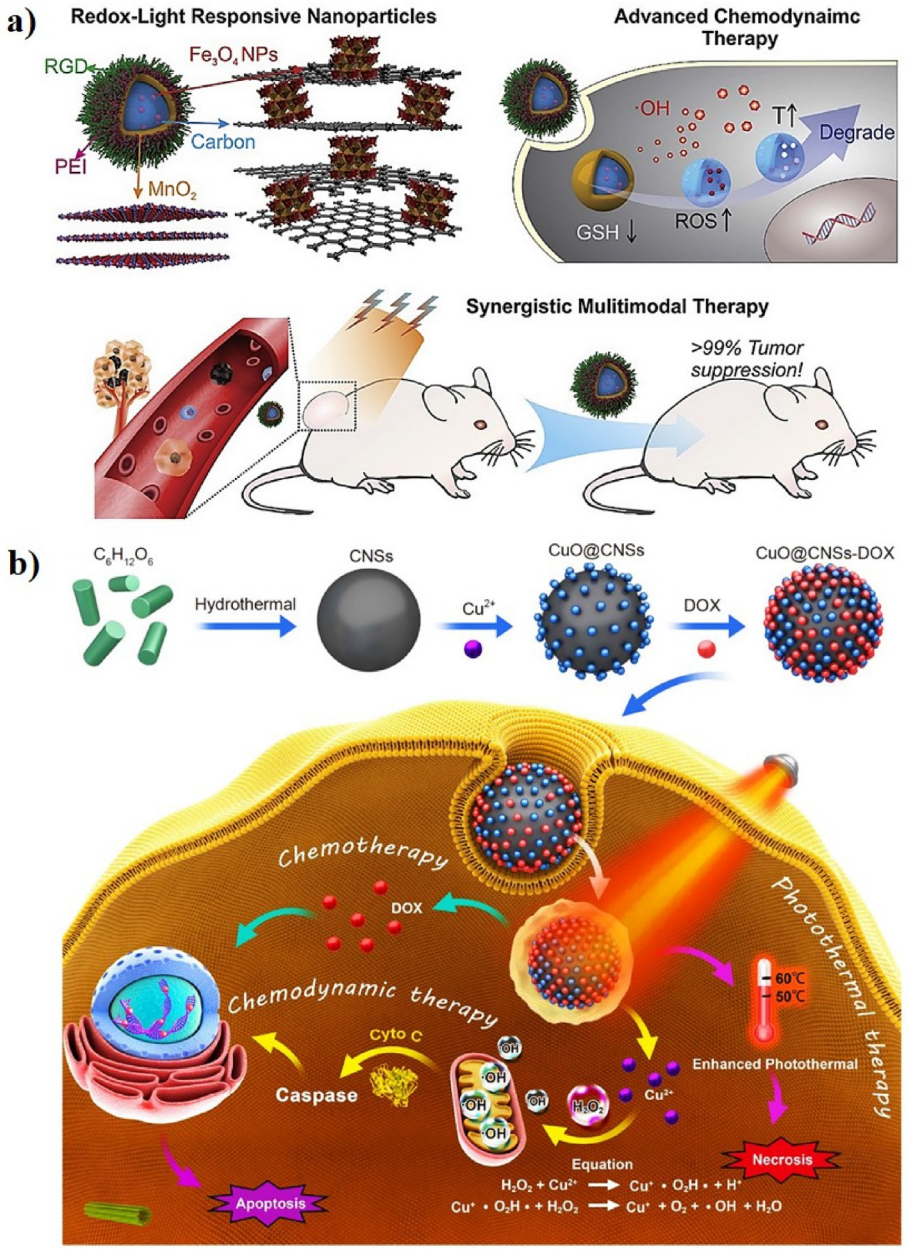


**Fig. 16.** (a) A schematic illustration of the fabrication of RLR NPs for chemo-PT-enhanced CDT. Reprinted with permission of Ref. [121]. Copyright 2019 Elsevier Ltd. (b) A schematic illustration of the synthesis of CuO@CNSs-DOX for chemo-PTT/CDT. Reprinted with permission of Ref. [133]. Copyright 2020 Springer.

developed new redox and light-responsive (RLR) NPs with ultra-small iron oxide ($Fe_3O_4$) NP-engineered framework comprised of an amorphous hollow carbon matrix core ($Fe_3O_4$–C) with nanoflower-like $MnO_2$ loaded with doxorubicin (DOX) for chemo-PT-CDT through a Fenton-like reaction, GSH depletion, and chemo-PT effect (Fig. 16a). The RLR NPs had an average diameter of 200 nm. The PCE ($\eta$) of the RLR NPs was 26.8%, which is the most efficient NIR of the PT agent. Ultra-small $Fe_3O_4$ NPs release $Fe^{2+}$ and $Fe^{3+}$ ions sequentially, which can self-activate the Fenton-like reactivity by catalyzing the conversion of $H_2O_2$ into a large number of toxic •OH radicals. This indicates that the acidic nature of the TME can accelerate the Fenton-like reactivity stimulated by the $Fe_3O_4$ NPs and enhance the therapeutic efficacy via the ferroptosis pathway. The RLR NPs were programmed to self-activate CDT by reducing the intracellular levels of the antioxidant GSH, accelerating ROS generation, spatiotemporal controllable PTT, and redox-triggered DOX release. The RLR NPs-treated cells have a significantly higher level of ROS after laser irradiation, suggesting the heat production from PTT can accelerate the RLR NPs-based CDT. In addition, the RLR NP-based PTT can also improve the accumulation of DOX in cancer cells for CHT. Tumor-bearing mice were intravenously injected with FITC-labeled RLR NPs and *in vivo* fluorescence signals were observed at the tumor site after 2 h. In addition, $T_1$ MRI positive probes ($Mn^{2+}$) were released, allowing *in situ* MRI and the MR signals were observed at 1 and 3 h. The *in vivo* synergistic therapeutic efficacy of the RLR NPs almost stopped tumor growth during the experimental periods, suggesting that the RLR NPs have great potential for use in MRI-guided chemo-PT-enhanced CDT [121].

In another effort, Jiang and co-workers designed multifunctional doxorubicin (DOX)-loaded copper oxide-decorated carbon nanospheres (CuO@CNSs) for chemo-PT-enhanced CDT (Fig. 16b). The CNSs were used as PT agents, which were synthesized via a hydrothermal reaction. CuO was adsorbed on the surface of the CNSs, which can serve as a Fenton-like agent and enhance the PCE of NPs. DOX was finally conjugated on the surface of the CuO@CNSs via electrostatic interactions. The CuO@CNSs have a uniform spherical morphology with an average size of

15 nm. The PCE ($\eta$) of the CuO@CNSs was 10.14%, indicating excellent PT properties. The temperature of the CuO@CNS aqueous solution reached up to 60.3 °C, indicating that CuO@CNSs have potential advantages as PT agents. Copper oxide (CuO) can release $Cu^{2+}$ ions in the TME, which can produce •OH to induce cancer cell apoptosis via Fenton-like reactions. DOX is also released into the TME to kill cancer cells. The CuO@CNSs-DOX + NIR-treated 4T1 cells showed 29% cell apoptosis, indicating that the synergistic PT-enhanced CDT can enhance apoptosis and promote efficacy. The tumors treated with CuO@CNSs-DOX + NIR were completely inhibited, indicating that the synergistic PT-enhanced CDT had a good effect. PAI can provide a non-invasive diagnosis of diseases; the tumor region exhibits a strong PA signal after injection of CuO@CNS, indicating that the CuO@CNSs are ideal PA imaging contrast agents for PAI-guided cancer diagnosis. Multifunctional CuO@CNSs-DOX nanoplatforms have great potential for PAI-guided chemo-PT-enhanced CDT [133].

### 4.2. PT-enhanced CDT with SDT

SDT is a new non-invasive therapy that can eradicate solid tumors using ultrasound (US)-activated sonosensitizers to generate ROS, leading to tumor cell death [195–199]. Although its principle is similar to PDT, SDT is an emerging US-based cancer therapeutic method and is expected to be highly efficient because of its deeper penetration into the tumor site [200–202]. US can penetrate much deeper by several centimeters than PDT to trigger ROS generation and can therefore overcome the major problem of the deep penetration barrier of PDT [203,204]. PT-enhanced CDT with SDT has been used for high-efficiency cancer therapy [198]. For example, Liu et al. reported biocompatible PTMP-PMAA-modified ferrous phosphide ($Fe_2P$) nanorods (FP NRs) as an "all-in-one" Fenton-like agent for ultrasound (US)- and PT-enhanced CDT (Fig. 17a). $Fe_2P$ was synthesized via a high-temperature method and PTMP-PMAA was coated onto the surface of $Fe_2P$ via a ligand exchange method to enhance their biocompatibility and hydrophilicity. The FP NRs have a rod-like morphology with an average size of 180 nm. The PCE ($\eta$) of the

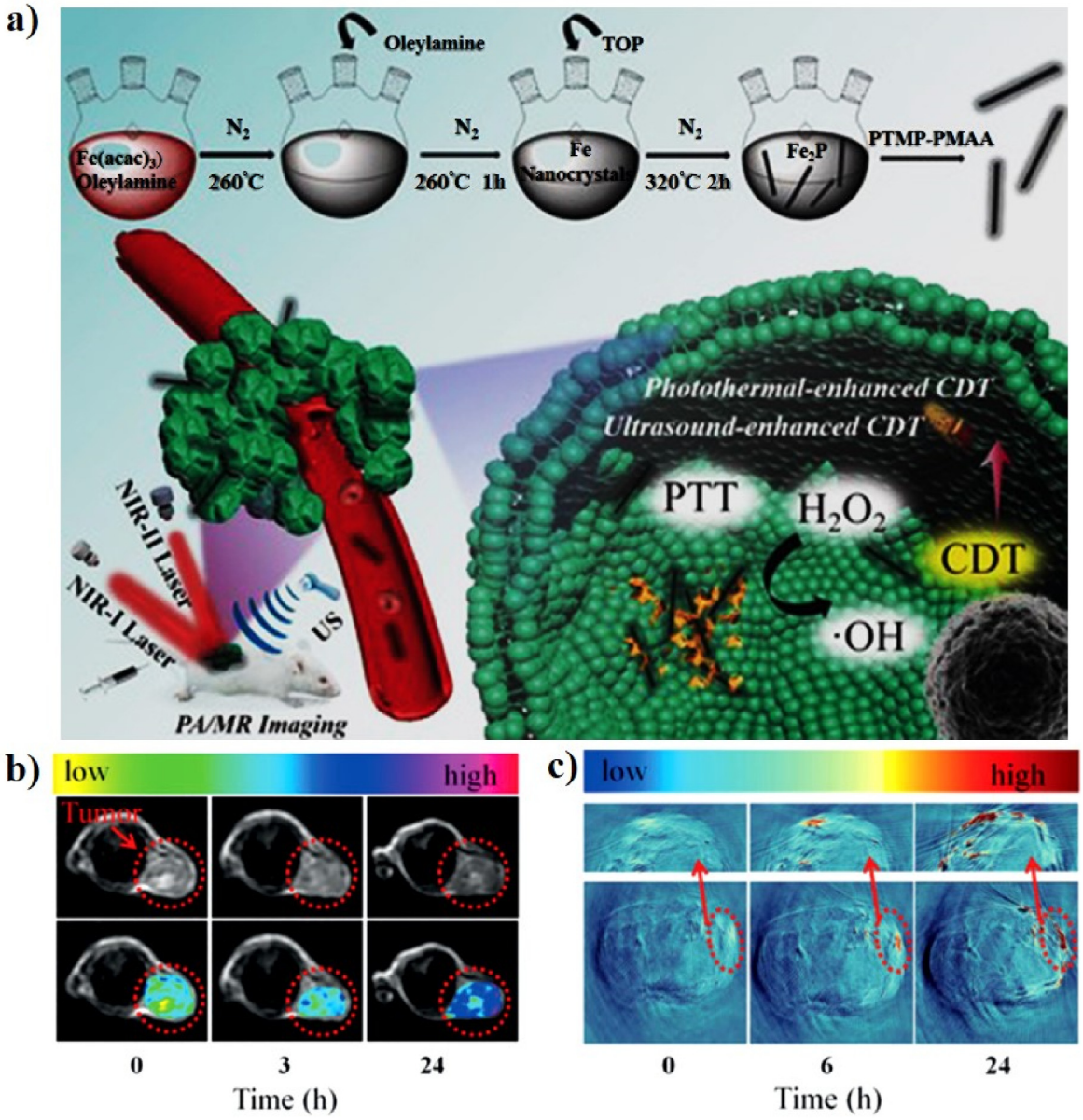


**Fig. 17.** (a) A schematic illustration of the synthesis of FP NRs for US/PT-enhanced CDT. *In vivo* MR (b) and PA (c) images of tumor-bearing mice. Reprinted with permission of Ref. [48]. Copyright 2019 Wiley.

FP NRs was 56.6% upon irradiation at 1064 nm, indicating their outstanding PT conversion effect. The FP NRs generate heat under 1064 nm laser irradiation, which effectively enhances the production of •OH. The conversion of $Fe^{3+}$ to $Fe^{2+}$ was accelerated by US and the $Fe^{2+}$ produced further reacts with $H_2O_2$ to generate more toxic •OH. Taken together, US and PT heat can effectively enhance the production of ROS by the FP NRs, allowing the application of FP NRs in PT-enhanced CDT with SDT *in vitro* and *in vivo*. HeLa cell-treated with FP NRs under the US and 1064 nm laser irradiation exhibit more dead cells, suggesting that the combination of PT-enhanced CDT and SDT shows outstanding anticancer effects. U14 tumor-bearing mice were intravenously injected with the FP NRs. The $T_2$-weighted MRI (Fig. 17b) and PA signals (Fig. 17c) of the tumor were enhanced after 24 h, suggesting that the FP NRs can accumulate at the tumor site through the EPR effect. Tumors were fully inhibited after US and1064 nm laser irradiation, implying that the FP NRs have a good PT-enhanced CDT with SDT effect. Hence, FP NRs can serve as dual-modality MRI/PAI agents to accurately diagnose tumors and provide precise information for US- and PT-enhanced CDT. The synergistic ultrasound- and PT-enhanced CDT can cause cancer cell death *in vitro* and fully inhibit tumors *in vivo*, which indicates their remarkable anticancer activity [48].

### 4.3. PT-enhanced CDT with PDT

PDT has been developed over the last decade as an attractive alternative treatment modality, which uses photosensitizers to produce ROS under laser irradiation to induce cancer cell apoptosis [205–207]. PDT has been clinically approved for the treatment of various diseases [208, 209]. It has the distinct advantages of high selectivity, reduced invasiveness, strong curative effect, and reduced side effects [206]. However, the clinical use of PDT is limited by its poor tissue penetration and tumor hypoxia [210]. To solve this problem, combination therapies using PTT, CDT, and PDT have been employed to achieve a remarkable inhibition of tumor growth by promoting multiple anticancer mechanisms, which can effectively improve the therapeutic effect of PDT [96,211]. For example, Xiao et al. prepared L-buthionine-sulfoximine (BSO)-modified $FeS_2$ NPs (BSO–$FeS_2$ NPs) as theranostic agents for PAI-guided PT-enhanced chemodynamic/photodynamic therapy (Fig. 18a). The $FeS_2$ NPs were prepared using a simple synthesis of CdTe NPs and BSO was conjugated to TGA on the surface of $FeS_2$ utilizing carbodiimide/*N*-hydroxysuccinimide (EDC/NHS) chemistry. $FeS_2$ has been applied for PTT and PDT, and can also catalyze the decomposition of $H_2O_2$ to effectively produce •OH for CDT. BSO–$FeS_2$ NPs have a uniform spherical morphology with an average particle size of 7.27 ± 1.43 nm. Moreover, they exhibited an outstanding PCE ($\eta$) of 49.5%. The $FeS_2$ NPs can catalyze the decomposition of $H_2O_2$ to produce a large amount of •OH via a Fenton-like reaction in an acidic environment. The BSO–$FeS_2$ NPs inhibit the synthesis of GSH, suggesting that BSO can considerably accelerate the accumulation of ROS to achieve excellent tumor treatment efficacy. 4T1 cells treated with BSO–$FeS_2$ NPs show a higher rate of apoptosis (45.45%) after laser irradiation, indicating that BSO–$FeS_2$ NPs with laser irradiation can successfully induce 4T1 cells apoptosis. Mice injected with BSO–$FeS_2$ NPs exhibit an increase in the tumor temperature increase to 45 °C, which was sufficient to kill the tumor (Fig. 18b). The *in vivo* PA signals in tumor-bearing mice treated with BSO–$FeS_2$ NPs were significantly high, indicating that the BSO–$FeS_2$ NPs can be used as promising PA contrast

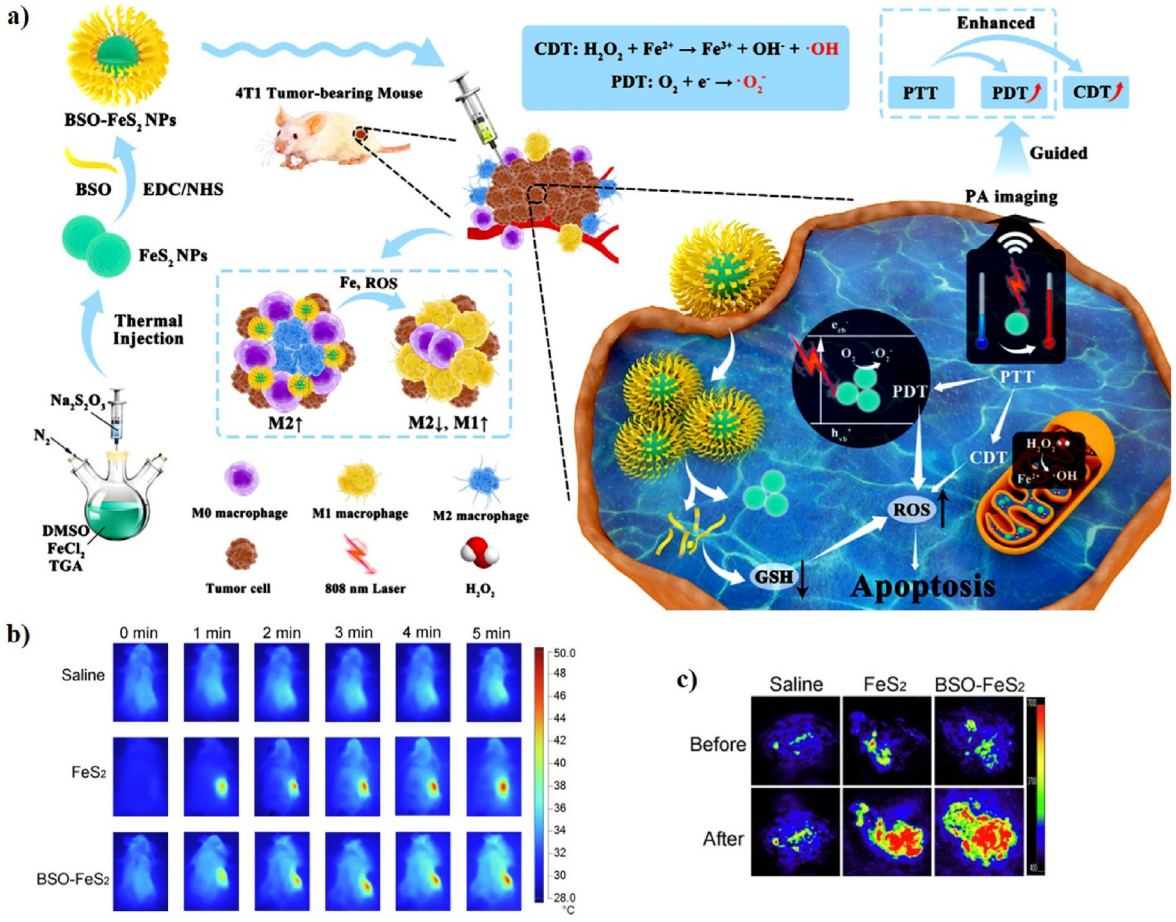


**Fig. 18.** (a) A schematic illustration of the fabrication of BSO–$FeS_2$ NPs for PT-enhanced PDT/CDT. (b) IR thermal images of tumor-bearing mice. (c) *In vivo* PA images tumor-bearing mice after intratumoral injection of BSO–$FeS_2$ NPs. Reprinted with permission of Ref. [120]. Copyright 2020 Elsevier Ltd.

agents for solid tumor monitoring (Fig. 18c). Therefore, BSO–$FeS_2$ NPs have been used as an "all-in-one" theranostic agent for the PAI-guided PTT/CDT/PDT of cancer [120].

### 4.4. PT-enhanced CDT with IMT

Recently, IMT has emerged as a promising therapeutic modality that mobilizes the host's immunity against cancer [212–214]. However, the major drawbacks of IMT are its poor immunogenicity, high mutability, insufficient activation of the host immune system, and low immune cell infiltration in most cancers [215,216]. Recent reports have shown that combining IMT with PT-enhanced CDT may increase the response rates for non-inflamed tumors [217]. PT-induced IMT can activate innate and adaptive immune responses against cancer [218,219]. Therefore, the achievement of PTT/CDT mediated by nanomaterials conjugated with antigens and adjuvants has been developed over the past decade as a potential alternative for safer and more effective cancer IMT [220,221]. For example, Jiang et al. first reported the integration of semiconductor copper(II) oxide (CuO) and molybdenum disulfide ($MoS_2$) nanoflowers to form $MoS_2$–CuO heteronanocomposites, which were subsequently loaded with BSA and immunoadjuvant imiquimod (R837) for PTT/CDT/IMT (Fig. 19a). The $MoS_2$ nanoflowers were prepared via a hydrothermal method and CuO was then loaded on the surface of the $MoS_2$ nanoflowers, which were modified with BSA and R837 to enhance their immunogenicity and biocompatibility. The $MoS_2$–CuO@BSA/R837 (MCBR) nanoplatforms significantly improved the antitumor efficiency of the synergetic PTT/CDT/IMT. $MoS_2$ has a diameter of ~130 nm and the PCE ($\eta$) of $MoS_2$–CuO was calculated to be 24.6%. CuO can react with the overexpressed $H_2O_2$ present in the TME to produce a large amount of •OH via a Fenton-like reaction; this reaction can be further improved by the PT effect of $MoS_2$. The MCBR can destroy the primary tumor and release tumor-associated antigens (TAAs), which combine with R837 as an immune-stimulating adjuvant to trigger a strong antitumor immunological response, which can effectively remove primary and metastatic tumors via synergetic PT-enhanced CDT/IMT. Multimodal imaging, such as MRI, CT, and infrared (IR) thermal imaging, can provide complementary information for the diagnosis and treatment of cancer. The $T_1$-MR signal of the tumor site is significantly enhanced after the injection of MCBR, indicating that MCBR can serve as an ideal $T_1$-MR contrast agent (Fig. 19b). A strong CT signal was observed in the tumor area, demonstrating the ideal CT imaging capability of MCBR (Fig. 19c). The temperature variations in the tumor area were also studied after post-injection of MCBR and laser irradiation (Fig. 19d), confirming that MCBR possesses the potential to act as a multifunctional contrast agent for MRI/IR/CT-guided PT-enhanced CDT/IMT [47].

In another similar recent study, Wang et al. fabricated chlorin e6 (Ce6)-loaded PEG-coated $Au_2Pt$ ($Au_2Pt$-PEG-Ce6) for collaborative phototherapy/CDT (Fig. 20a). The $Au_2Pt$ NPs have a spherical morphology with an average diameter of 42 ± 3 nm, and the zeta potential of $Au_2Pt$-PEG-Ce6 was −24.2 mV. The PCE ($\eta$) of $Au_2Pt$-PEG-Ce6 was 31.5%, implying that $Au_2Pt$-PEG-Ce6 has an excellent PT conversion ability. $Au_2Pt$-PEG-Ce6 possesses catalase- and peroxidase (POD)-like activities, which can effectively generate $O_2$ and •OH for PT-enhanced PDT and CDT. In this reaction, $H_2O_2$ was decomposed by $Au_2Pt$ to produce •OH for 3,3′,5,5′-tetramethylbenzidine (TMB) oxidation, which occurs in a pH- and temperature-dependent manner. The *in vitro* synergistic effect of

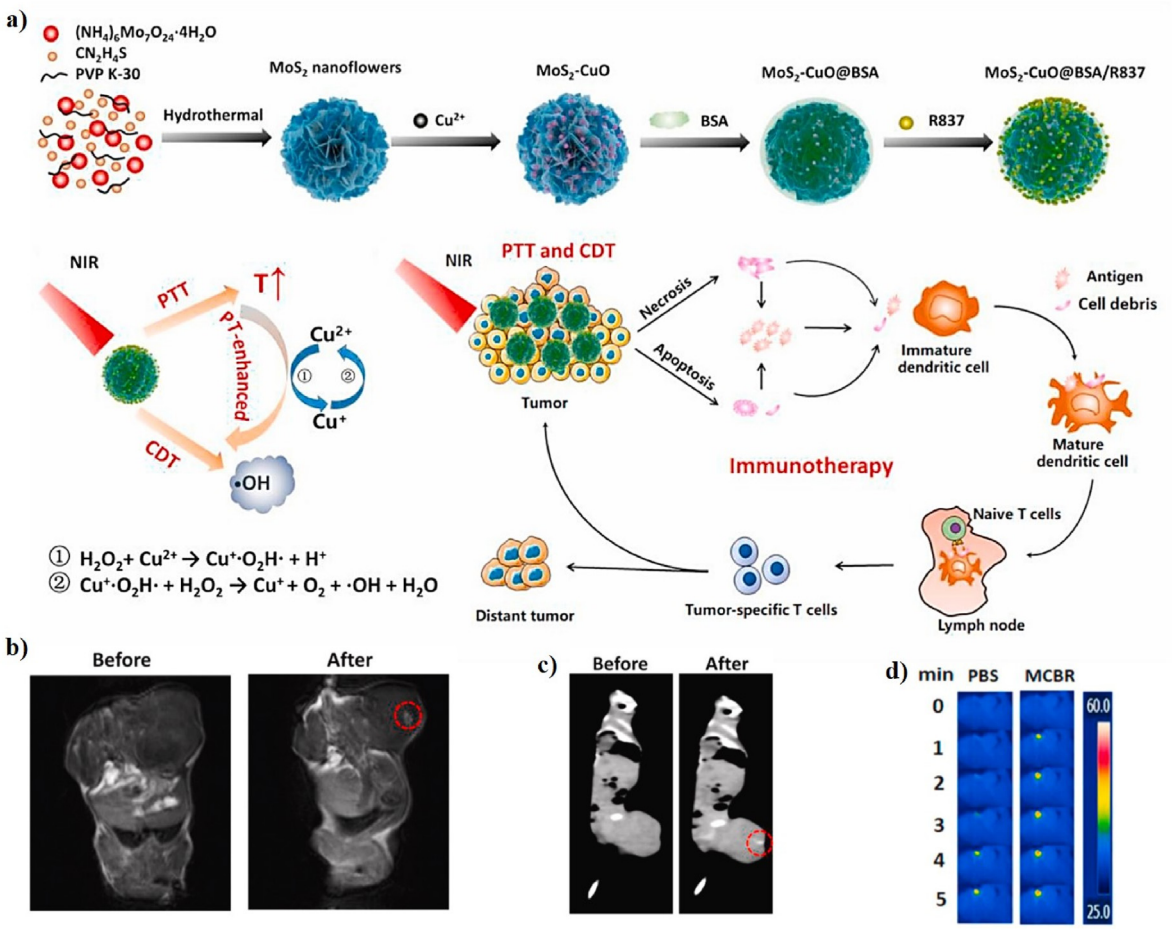


**Fig. 19.** (a) A schematic illustration of the synthesis of $MoS_2$–CuO@BSA/R837 (MCBR) for PTT/CDT/IMT. *In vivo* MR (b), CT (c), and IR thermal (d) images of a tumor after intratumoral injection with MCBR. Reprinted with permission of Ref. [47]. Copyright 2020 Elsevier Ltd.

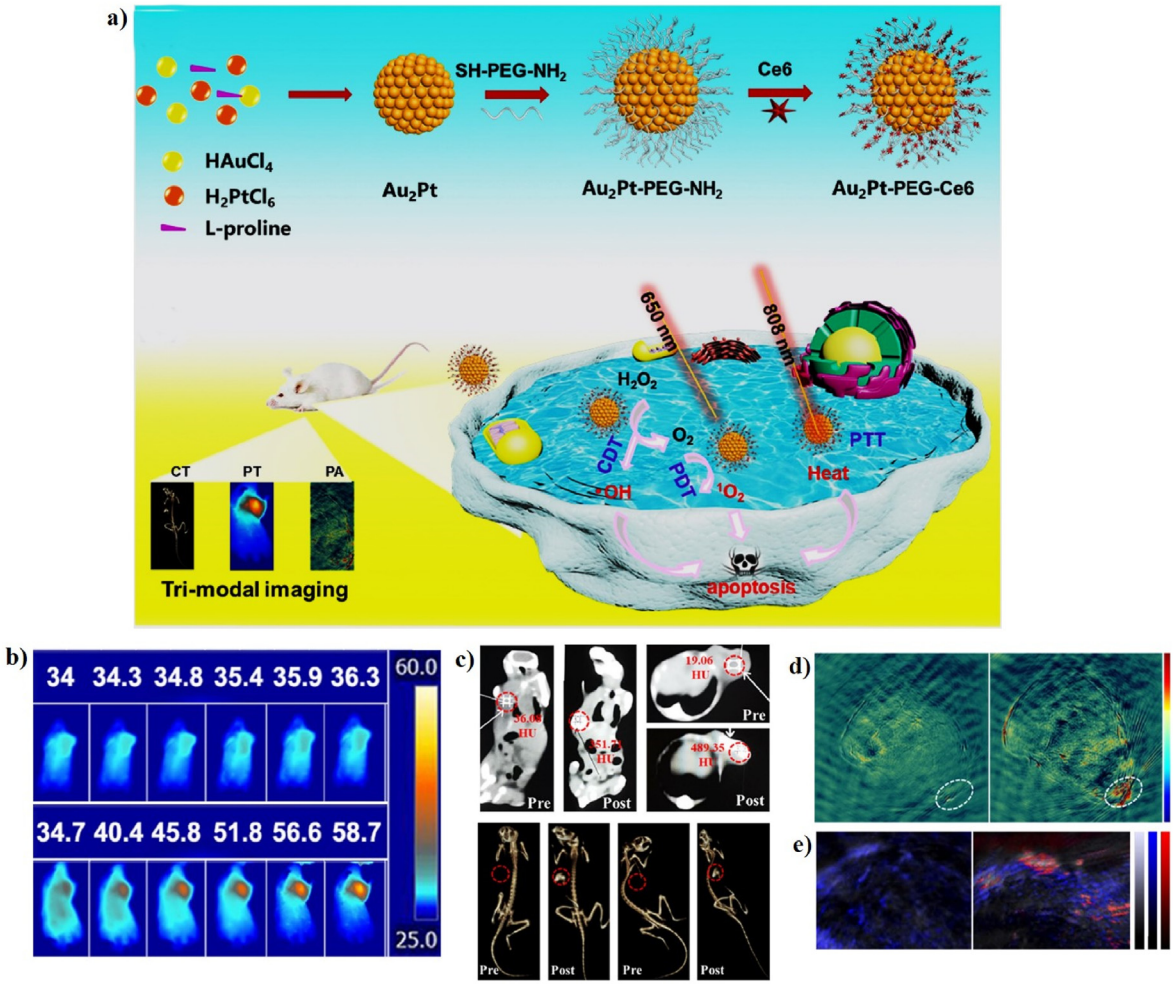


**Fig. 20.** (a) A schematic illustration of the synthesis procedure of $Au_2Pt$-PEG-Ce6 for collaborative phototherapy/CDT. (b) *In vivo* IR thermal images of tumor-bearing mice injected with saline and $Au_2Pt$-PEG-Ce6. (c) *In vivo* CT images of tumor-bearing mice pre- and post-intratumoral injection of $Au_2Pt$-PEG-Ce6. (d) *In vivo* PA images of tumor-bearing mice injected with saline and $Au_2Pt$-PEG-Ce6. (e) *In vivo* PA images of hemoglobin (HB) and oxyhemoglobin ($HBO_2$) in the tumor area post-injection of $Au_2Pt$-PEG-Ce6. Reprinted with permission of Ref. [138]. Copyright 2020 Elsevier Ltd.

$Au_2Pt$-PEG-Ce6 against HeLa cells was further evaluated and the survival rate of the HeLa cells treated with $Au_2Pt$-PEG-Ce6 was significantly reduced to 12% after 650 and 808 nm laser irradiation, indicating that the synergistic effect can enhance the therapy efficiency. $Au_2Pt$-PEG-Ce6 showed significant tumor-suppressive therapeutic efficiency in intratumorally injected U14 tumor-bearing mice under 650 and 808 nm laser irradiation, implying the prominent synergistic effect of PT-enhanced PDT and CDT. In addition, the tumor temperature variations in the $Au_2Pt$-PEG-Ce6 group were more prominent than those in the control group. Moreover, the temperature increased in the tumor area, implying that NIR laser irradiation was biosafe toward healthy tissues (Fig. 20b). The CT imaging ability of $Au_2Pt$-PEG-Ce6 was evaluated *in vitro* and *in vivo,* and strong CT signals were observed in the tumor area, indicating that $Au_2Pt$-PEG-Ce6 can serve as a good CT imaging agent (Fig. 20c). PA images and signals were observed after injection of $Au_2Pt$-PEG-Ce6 (Fig. 20d, e). Thus, $Au_2Pt$-PEG-Ce6 shows promising therapeutic potential for use in multimodal imaging-guided PT-enhanced PDT/CDT [138].

### 4.5. PT-enhanced CDT with ST

Tumor cells require a considerable amount of energy during tumor metabolism, growth, proliferation, and metastasis [222]. Based on the Warburg effect, the proliferation of tumor cells mainly produces sufficient energy through aerobic glycolysis, which makes tumor cells more sensitive to variations in the intracellular glucose concentration [223]. Therefore, glucose consumption in tumor cells can disrupt glucose metabolism in tumor cells, resulting in the ST of tumor cells [224]. Cancer ST is a new strategy that blocks the energy supply to tumor cells [225,226]. To date, various strategies have been developed to prevent tumor growth and metabolism via intratumoral glucose consumption [225]. Glucose oxidase (GOx or GOD) is an enzyme that can effectively catalyze the reaction between glucose and $O_2$ to produce gluconic acid and $H_2O_2$, which can occur under acidic conditions, which are satisfactory reactants for CDT [227]. The use of glucose oxidation *via* the catalytic reaction of GOx can block the energy supply to prevent tumor growth [228]. In particular, GOx-based ST shows an extraordinary capability to inhibit tumor growth by catalyzing the oxidation of glucose, which has received a lot of attention from researchers in recent years [229]. However, GOx-based ST has limited therapeutic efficiency, such as low stability, immunogenicity, and fragile enzymatic activity, and has also been recently used as an auxiliary treatment [59,228]. Therefore, the combination of PT-enhanced CDT with ST can effectively produce a synergistic antitumor effect, which can significantly prevent the growth of tumors when compared with a single therapy (PTT, CDT, or ST) [230]. In particular, the large amount of generated/accumulated $H_2O_2$ and the production of gluconic acid in the TME is satisfactory for accelerating the Fenton or Fenton-like reactions to generate •OH and further improve the CDT efficacy [228,231]. In addition, the increased temperature in the

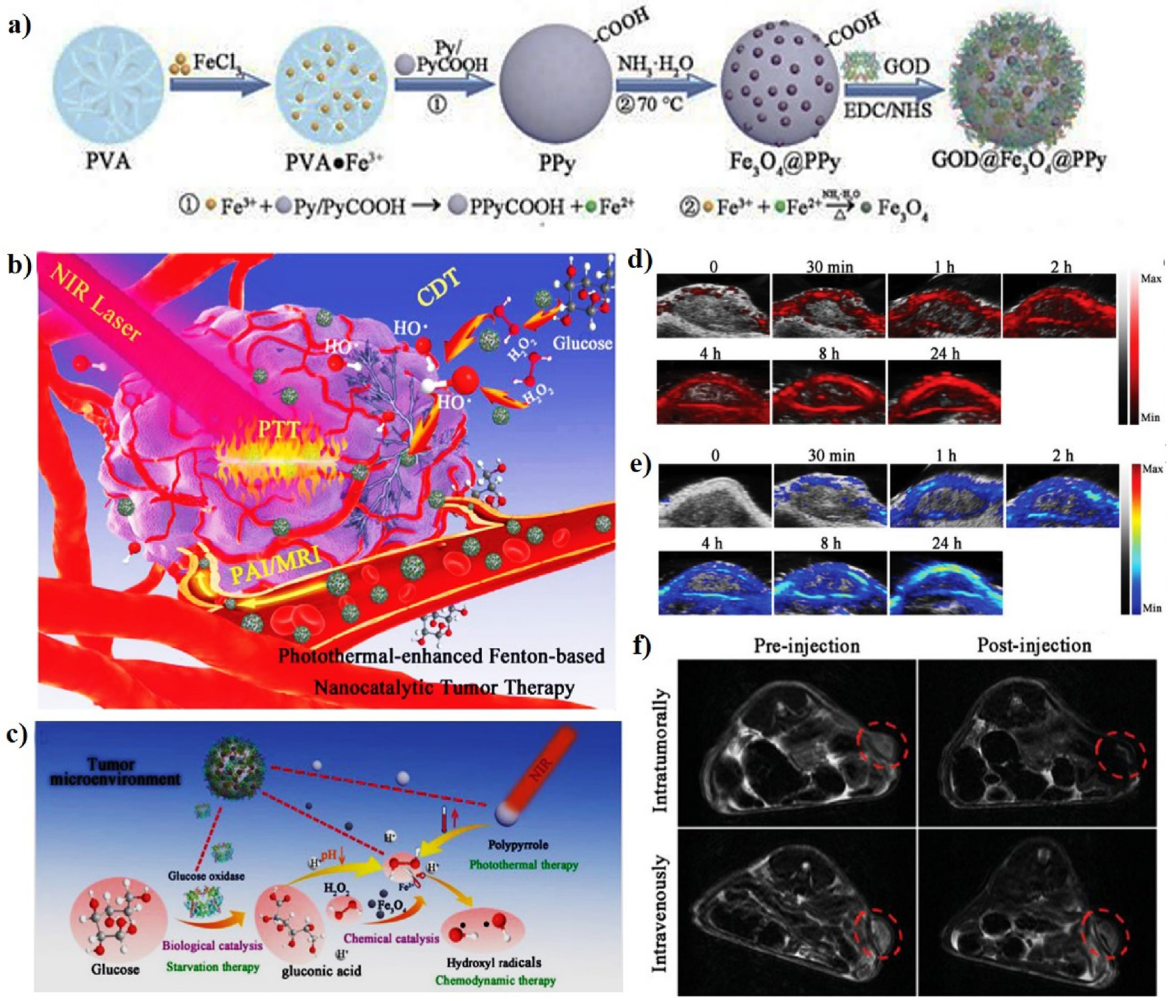


**Fig. 21.** A schematic illustration of the synthesis of $Fe_3O_4$@PPy@GOD NCs (a) and PT-enhanced CDT (b). (c) Proposed mechanism of $Fe_3O_4$@PPy@GOD NCs for PT-enhanced Fenton-based CDT. *In vivo* PAI and PA signals of the tumor area at various time points post-injection of $Fe_3O_4$@PPy@GOD NCs at 808 nm (d) and 1280 nm (e). (f) *In vivo* $T_2$-weighted MR images of tumor-bearing mice before and after intratumoral and intravenous injection of $Fe_3O_4$@PPy@GOD NCs (the red dotted circles indicate the tumor areas). Reprinted with permission of Ref. [59]. Copyright 2018 Wiley.

TME can effectively accelerate the transformation of $H_2O_2$ and •OH, and therefore, the rational combination of PT-enhanced CDT with ST is expected to enhance its performance in the treatment of tumors [27].

As representative GOD-based nanocomposites in CDT, Feng et al. reported, for the first time, superparamagnetic $Fe_3O_4$-modified polypyrrole (PPy) NPs conjugated with glucose oxidase (GOD) for PT-enhanced CDT (Fig. 21a, b). PPy is a typical electroconductive polymer because of its high conductivity and biocompatibility. PPy NPs can serve as photoabsorbing agents for PTT. $Fe_3O_4$ can be used as an effective Fenton agent for CDT. However, the major disadvantage of $Fe_3O_4$ for CDT is the low intracellular levels of $H_2O_2$ *in vivo* and the unsatisfactory catalytic Fenton reaction in the mildly acidic TME. Therefore, PT-enhanced CDT with ST is urgently required to develop an efficient approach to successfully achieve synergistic-therapeutic efficiency. GOD is an enzyme with abundant amino groups, which are covalently bonded to the surface carboxyl groups of $Fe_3O_4$@PPy NPs to form $Fe_3O_4$@PPy@GOD nanocomposites (NCs). The $Fe_3O_4$@PPy@GOD NCs had uniform size, with an average diameter of 163.5 nm. The PCE ($\eta$) of $Fe_3O_4$@PPy@GOD NCs was 35.1 and 66.4% at 808 and 1064 nm, respectively. The intratumoral glucose was converted into gluconic acid and $H_2O_2$ by the conjugated GOD and the integrated $Fe_3O_4$ component catalyzes the conversion of the *in situ* generated $H_2O_2$ into highly toxic •OH via the well-established catalytic Fenton reactions, resulting in ST-enhanced CDT. Importantly, PPy NPs not only effectively generate heat, but also accelerate the intratumoral catalytic Fenton reaction to induce cancer cell apoptosis and necrosis, indicating the synergistic effect of PT-enhanced CDT with ST in combating cancer (Fig. 21c). 4T1 tumor-bearing mice treated with $Fe_3O_4$@PPy@GOD NCs and 808 or 1064 nm laser irradiation almost completely inhibit tumor growth during the experimental period, implying that $Fe_3O_4$@PPy@GOD NCs are potentially powerful therapeutic agents for combating cancer. $Fe_3O_4$@PPy@GOD NCs can serve as an efficient contrast agent for dual-modality PAI/MRI. The photoacoustic (PA) intensities of $Fe_3O_4$@PPy@GOD NCs at 808 or 1280 nm were evaluated in 4T1 tumor-bearing mice; the PA amplitude at 808 or 1280 nm in the tumor site increases gradually post-injection of the $Fe_3O_4$@PPy@GOD NCs, suggesting the time-dependent accumulation of $Fe_3O_4$@PPy@GOD NCs at the tumor site (Fig. 21d, e). The MR signaling properties of the $Fe_3O_4$@PPy@GOD NCs show a uniform signal distribution inside the entire tumor, suggesting that the $Fe_3O_4$@PPy@GOD Cs can reach the whole tumor site from blood circulation, leading to successful dual-mode imaging-guided PT-enhanced CDT/ST (Fig. 21f) [59].

In another study, Liu and co-workers synthesized glucose oxidase (GOx)-loaded polyethylenimine (PEI)-coated $Fe_3O_4$ that reacted with PEGylated multi-walled carbon nanotubes (MWNTs) to form PEG-MWNT-$Fe_3O_4$ (PMF) for PT-enhanced CDT. PEI is a highly charged cationic polymer that is widely used as a biocompatible coating material on the surface of NPs. MWNTs have been extensively used as effective

photoablation agents in PTT. GOx is capable of converting glucose in the mildly acidic TME into gluconic acid and $H_2O_2$, which can act as an effective Fenton catalyst and boost the $Fe_3O_4$-based Fenton reaction to produce •OH to induce tumor cell death. Moreover, this Fenton reaction can be further enhanced upon laser irradiation via the PT effect from the MWNTs, which significantly enhances the CDT effect. $Fe_3O_4$ shows a spherical morphology with an average size of 12–20 nm. The temperature of the PMF-GOx (PMFG) aqueous solutions increases to 45 °C under 808 nm laser irradiation for 5 min, which was sufficient to improve CDT. The *in vitro* therapeutic effect of PMFG + NIR-treated on MCF-7 cells showed enhanced cell apoptosis, implying a highly effective •OH was generated under laser irradiation [25].

Transition metal chalcogenides, including, copper-molybdenum sulfide ($Cu_2MoS_4$) have received significant attention because of their strong absorption in the NIR region and great catalytic performance, which can combine with GOx to achieve ST and PT-enhanced CDT [232]. For example, Chang et al. reported, for the first time, the use of PEGylated hollow mesoporous copper-molybdenum sulfide ($Cu_2MoS_4$) (CMS) loaded with GOx (PEG-CMS@GOx) for synergetic cancer therapy via PT-enhanced photodynamic/chemodynamic/starvation/immunotherapy (Fig. 22). PEG-CMSs show plentiful pores with an average size of 5.88 nm, and a zeta potential of −13.7 mV. The 1064 nm laser irradiated CMS presents a high PCE ($\eta$ = 63.27%), confirming that CMS has excellent PT stability and serves as a PT agent. The existence of multivalent metal ions, such as $Cu^{+}/Cu^{2+}$ and $Mo^{4+}/Mo^{6+}$ redox couples, in CMS results in a large amount of •OH being generated via Fenton-like, catalase-like, and glutathione peroxidase (GPx)-like reactions, which can significantly improve the CDT effect. CMS can react with endogenous $H_2O_2$ to produce $O_2$, which can stimulate the conjugated GOx to produce gluconic acid and $H_2O_2$ within the tumors sites and boost the Fenton-like reaction to generate •OH. Meanwhile, CMS with 1064 nm laser irradiation shows an excellent tumor-killing capability by photo-based therapy because of its good PCE and toxic $\bullet O_2^-$ generation performance for PDT. In addition, CMS can elicit vaccine-like immune responses after primary tumor ablation, which can promote the conjugated anti-cytotoxic T-lymphocyte antigen-4 (CTLA4) and successfully inhibit tumor metastasis via IMT. The *in vitro* therapeutic effect of PEG-CMS@GOx was assessed in HeLa cells with various stimulations. PEG-CMS@GOx reacts with $H_2O_2$ in HeLa cells to produce a small amount of •OH and cause marginal cell death in CDT. Much more •OH is produced via GOx-enhanced CDT, indicating that the synergistic effect of CDT/ST can effectively inhibit tumors, resulting in more cell death than single CDT. Most importantly, 100% of HeLa cells were dead after 1064 nm laser irradiation because of the synergistic PT-enhanced CDT/PDT/ST. The antitumor effect of PEG-CMS@GOx can significantly induce *in vitro*

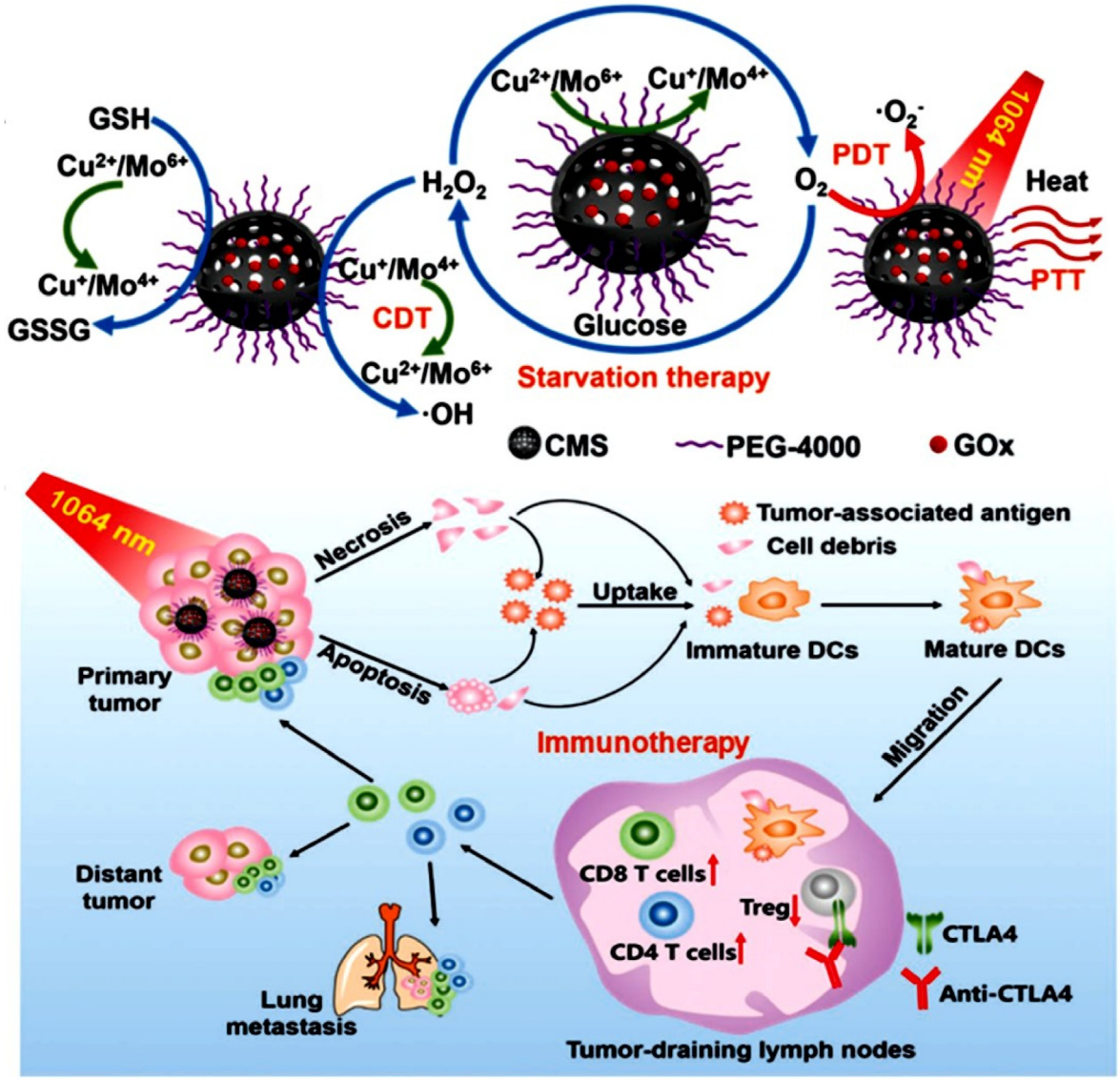


**Fig. 22.** A schematic illustration of the synthesis and working mechanisms of PEG-CMS@GOx. Reprinted with permission of Ref. [134]. Copyright 2019 Wiley.

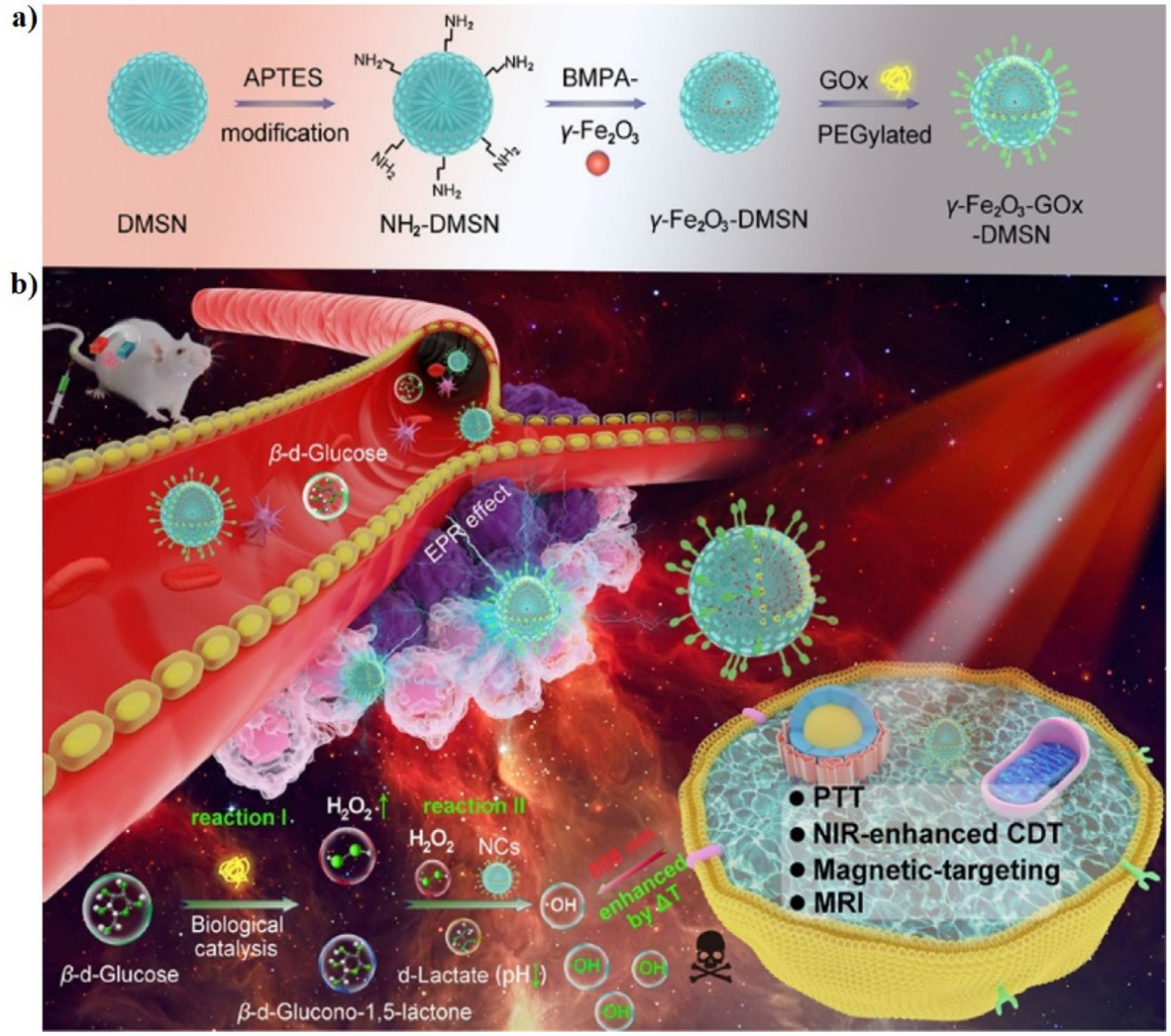


**Fig. 23.** A schematic illustration of the (a) preparation of γ-$Fe_2O_3$-GOx-DMSN NCs and (b) PT-enhanced CDT using γ-$Fe_2O_3$-GOx-DMSN NCs. Reprinted with permission of Ref. [119]. Copyright 2020 American Chemical Society.

dendritic cell (DC) maturation, suggesting that the comprehensive synergistic effect may elicit a powerful immune response. The *in vivo* synergistic therapeutic efficacy of PEG-CMS@GOx + anti-CTLA4 + 1064 nm laser irradiation almost completely inhibits tumor growth, indicating that PEG-CMS@GOx with anti-CTLA4 and laser irradiation can effectively eliminate primary and metastatic tumors via comprehensive synergistic cancer therapy [134].

By employing the characteristics of $Fe_2O_3$ NPs and GOx, Dong et al. proposed the introduction of novel ultra-small γ-$Fe_2O_3$ NPs and macromolecular GOx into dendritic mesoporous silica nanoparticles (DMSNs) as functional nanocatalysts (NCs) for PT-enhanced CDT into a single nanoplatform with superior $T_2$-weighted MRI performance (Fig. 23a, b). DMSN has an average diameter of 130 nm and the ultra-small γ-$Fe_2O_3$ NPs were ~5–6 nm in diameter. The PCE ($\eta$) of the γ-$Fe_2O_3$-GOx-DMSN NCs was 49.8%. The GOx release profile of the γ-$Fe_2O_3$-GOx-DMSN NCs exhibits temperature-dependent activity, reaching 79.24% after 10 h at 50 °C, causes a decrease in the pH value and an increase in the $H_2O_2$ levels in cancer cells, which further enhances the subsequent Fenton reaction. γ-$Fe_2O_3$ NPs can efficiently catalyze the Fenton reaction to produce •OH, inducing the apoptosis of the cancer cells. The *in vivo* $T_2$-weighted MRI effect of the γ-$Fe_2O_3$-GOx-DMSN NCs was 68.013 m $M^{-1}$ $S^{-1}$ at pH 6.0, suggesting that more γ-$Fe_2O_3$-GOx-DMSN NCs are accumulated at the tumor site. Thus, they can be employed as multifunctional nanoagents for MRI-guided PT-enhanced CDT. The *in vivo* therapeutic effect of the γ-$Fe_2O_3$-GOx-DMSN NCs exhibits the most significant inhibition of tumor growth in mice after laser irradiation, indicating that the laser irradiation of γ-$Fe_2O_3$-GOx-DMSN NCs revealed a strong capacity to induce cytotoxic heat to ablate the cancer cells, which can significantly improve the therapeutic outcome of PT-enhanced CDT [119].

In another study, by employing the unique nature of GOX and molybdenum disulfide ($MoS_2$)@manganese ferrite ($MnFe_2O_4$), Zheng et al. developed a multifunctional hybrid hydrogel (CFMG) by incorporating $MoS_2$@$MnFe_2O_4$ in chitosan-grafted-dihydrocaffeic acid (CA-DA) and Pluronic F127 loaded with GOx for PT-enhanced CDT. The $MnFe_2O_4$ NPs were uniformly distributed on the ultra-thin $MoS_2$ nanosheets, resulting in the formation of $MoS_2$@ $MnFe_2O_4$ nanocomposite. The temperature variations in the CFMG hydrogel increase rapidly up to ~49.5 °C with laser irradiation for 5 min, confirming its strong PT properties. GOx catalyzes the conversion of glucose into gluconic acid and $H_2O_2$, thereby inducing an effective reduction in the pH and production of $H_2O_2$. In addition, the low pH significantly accelerates the release of $Fe^{2+}$ and $Fe^{3+}$ from $MnFe_2O_4$ and enhances the reactivity of the subsequent Fenton reaction to generate •OH. Furthermore, the PT effect also accelerated the production of •OH, demonstrating that GOx and the PT effects were responsible for boosting •OH. The *in vitro* therapeutic effect of the CFMG hydrogel stimulated more cell death after laser irradiation with ~97.8% of cancer cells being destroyed. The *in vivo* antitumor efficacy of the CFMG hydrogel with laser irradiation almost completely inhibited tumor

growth after 15 days, demonstrating that CFMG has promising potential for use in PT-enhanced CDT [126]. In a similar study, An et al. reported a hypoxia-responsive-azo-BSA functionalized biomimetic nanoreactor (Fe(III)-GA/GOx@ZIF-Azo) encapsulating ferric-gallic acid NPs (Fe(III)-GA) and GOx into a zeolitic imidazolate framework (ZIF) for PT-enhanced CDT. The Fe(III)-GA NPs self-assembled via strong coordination bonds between $Fe^{3+}$ and GA. The Fe(III)-GA and GOx were incorporated into the zeolitic imidazolate framework (ZIF) to form a highly effective •OH generating nanoplatform (Fe(III)-GA/GOx@ZIF). The 4,4′-azobenzenecarboxylic acid moieties(Azo) can produce hypoxia-activated charge reversal from negative to positive, allowing for easier cellular uptake and tumor accumulation. Azo-BSA was prepared upon the reaction between the carboxyl and amino groups. Azo-BSA was functionalized on the surface of Fe(III)-GA/GOx@ZIF (FGGZ) to form Fe(III)-GA/GOx@ZIF-Azo (FGGZA). The Fe(III)-GA NPs have an average diameter of ~3 nm, and the PCE ($\eta$) of Fe(III)-GA was 66.5%, implying that Fe(III)-GA exhibits outstanding PT performance. The PT conversion of Fe(III)-GA and the acidic pH caused by the gluconic acid and $H_2O_2$ produced by GOx, can efficiently improve the Fenton reaction, leading to the production of •OH for PT-enhanced CDT. The *in vitro* therapeutic effect of FGGZ + NIR toward MCF-7 cells shows a higher •OH generation efficacy, indicating that FGGZ can serve as a Fenton agent for highly effective ferroptosis therapy. The *in vivo* therapeutic efficiency of FGGZA + NIR exhibits a high tumor inhibition rate of 78%, implying that Fe(III)-GA/GOx@ZIF-Azo has great therapeutic potential as an effective ferroptosis-inducing nanoagent [129].

More recently, based on the same principles, Yang et al. developed GOx-functionalized ancient pigment (strontium copper tetrasilicate ($SrCuSi_4O_{10}$), SC) nanosheets (NSs) for NIR-II PT-enhanced CDT. The SC was prepared using a conventional solid-state reaction method and then covalently functionalized with GOx via EDC/NHS chemistry to form the GOx-loaded SC NSs (denoted as SC@G NSs). The particle size of the SC@G NSs was ~60.94 nm and the calculated PCE ($\eta$) was 46.3% at 1064 nm, indicating that the SC@G NSs have great potential as PT agents for NIR-II PT-enhanced CDT. GOx was capable of converting glucose in the mildly acidic TME into gluconic acid and $H_2O_2$ to promote cytotoxic •OH, resulting in its enhanced CDT efficacy. The SC@G NSs sequentially release $Cu^{2+}$ and $Sr^{2+}$ ions, which can further catalyze the decomposition of the *in situ* generated $H_2O_2$ into cytotoxic •OH and depleted GSH. In addition, the Fenton-like reaction was significantly improved under laser irradiation, which confirmed the temperature-dependent GOx activity under laser irradiation. The *in vitro* synergistic PT- and ST-enhanced CDT effect of the SC@G NSs significantly inhibits the cellular viabilities under 808 and 1064 nm laser irradiation. 4T1 tumor-bearing mice were intravenously (i.v.) injected with the SC@G NSs to study their synergistic antitumor therapeutic efficacy. The tumor temperature of the SC@G NSs was elevated up to 47 °C under laser irradiation for 5 min, implying that the SC@G NSs can significantly suppress tumor growth. In addition, the SC@G NSs were intravenously injected into mice for *in vivo* PAI and the PA signals at the tumor site gradually increase post-injection, indicating that the SC@G NSs were accumulated in the tumor area. Furthermore, the PT effect can effectively improve the GOx activity and accelerate the intratumoral Fenton-like process, thereby achieving the synergistic effect of PAI-guided PT-enhanced CDT to combat cancer [131].

## 5. Conclusions and future perspectives

To date, the development of multifunctional nanomaterials for PT-enhanced Fenton-based nanocatalytic tumor therapy has aroused a lot of interest and has become promising toward the discovery of more effective cancer treatment. CDT has recently emerged as a new tumor-specific therapy based on Fenton or Fenton-like reactions, has gained a lot of interest from researchers because of its high specificity and sensitivity of the clinical transformation potential. However, major scientific progress is still required to improve therapeutic outcomes and reduce side effects. Numerous highly specific and selective nanomaterials have been prepared as CDT agents to promote *in situ* Fenton and Fenton-like reactions to destroy tumors, which have potential therapeutic applications for the treatment of cancer. This strategy utilizes pH-independent Fenton or Fenton-like reactions to effectively boost the generation of •OH for CDT, which is only efficient in a narrow pH range between 3.0 and 5.0, whereas ineffective Fenton or Fenton-like reactions occur under the neutral and mildly acidic pH conditions (pH 5.6–6.8) of the TME. However, the slow formation of •OH in the mildly acidic TME limits the therapeutic efficacy of CDT. Thus, enhancing the speed of •OH production in the mildly acidic TME will be critical for the further improvement of CDT. Inspired by the basic principle that an increase in the local temperature at the tumor site can significantly increase the therapeutic efficacy of the Fenton reactions with an increased yield of •OH, which provides promising integration potential for PTT with CDT. As previously reported, PTT commonly employs PT agents to convert light to heat for tumor ablation, significantly improving CDT in target tissues and controlling the release of therapeutic agents. Recently, synergistic PT-enhanced CDT has received an increasing amount of research interest for clinical application because of its high therapeutic efficacy, minimal side effects, and excellent biosafety when compared to monotherapy. It has been recognized that the integration of multimodal therapies such as PT-enhanced CDT with CHT, PDT, SDT, IMT, and ST and multimodal imaging techniques such as PAI, FLI, MRI, and CT into one nanoplatform will further improve the tumor suppression efficacy because of their synergistic effects. In this review, we have outlined the recent progress and development of multifunctional nanomaterials for PT-enhanced chemodynamic synergetic therapy. However, PT-enhanced CDT is still at an early stage of development and it is still highly challenging for researchers to achieve catalytic efficacy with biosafety. There are still many challenges that should be addressed before PT-enhanced CDT is ready for clinical application in the future (Fig. 24).

First, the biosafety and biomedical effect of multifunctional nanomaterials with PT and chemodynamic properties are extremely important and urgent for its pre-clinical studies. The selectivity, biocompatibility, biodegradability, and biosafety of multifunctional nanomaterials are the most important factors affecting their clinical translation. Although the reported multifunctional nanomaterials have outstanding biosafety, selectivity, biocompatibility, and biodegradability *in vivo*, their long-term toxicity and side effects must be further investigated. Furthermore, a lot of multifunctional nanomaterials still have low toxicity and excellent biocompatibility but many additional factors, including metabolism, distribution, and immune response should be carefully considered. Additionally, most of the nanomaterials have demonstrated low degradability, raising concerns about long-term toxicity *in vivo*. Based on this, it is a very urgent need to synthesis ultra-small or biodegradable multifunctional nanomaterials to realize the rapid metabolism, degradation of nanomaterials, and remove them from the body while minimizing long-term toxicity concerns, which could be developed to improve biosafety. Therefore, it is of great importance to balance biosafety and PT-enhanced CDT therapeutic effect.

Second, the large-scale synthesis of high-quality multifunctional nanomaterials with PT and chemodynamic properties is also essential for clinical translation. Although the successful synthesis of multifunctional nanomaterials for mass production has been reported, these methods are still in the laboratory stage, and their industrialization is urgent. Furthermore, it is still a challenge to be industrialized due to the introduction of various functional components on the surface of nanomaterials to make them highly solubility, biocompatibility, and biodegradability.

Third, the therapeutic effect of PT-enhanced CDT can be further improved. To this aim, an in-depth investigation of the therapeutic pathway of PT-enhanced CDT using molecular and genetic approaches is essential for the further optimization of PT-enhanced CDT and its clinical applications. The actual mechanisms behind Fenton-based nanocatalytic tumor therapy and •OH generation in the TME are still unclear. To improve the efficacy of CDT, we much focus on their capabilities of

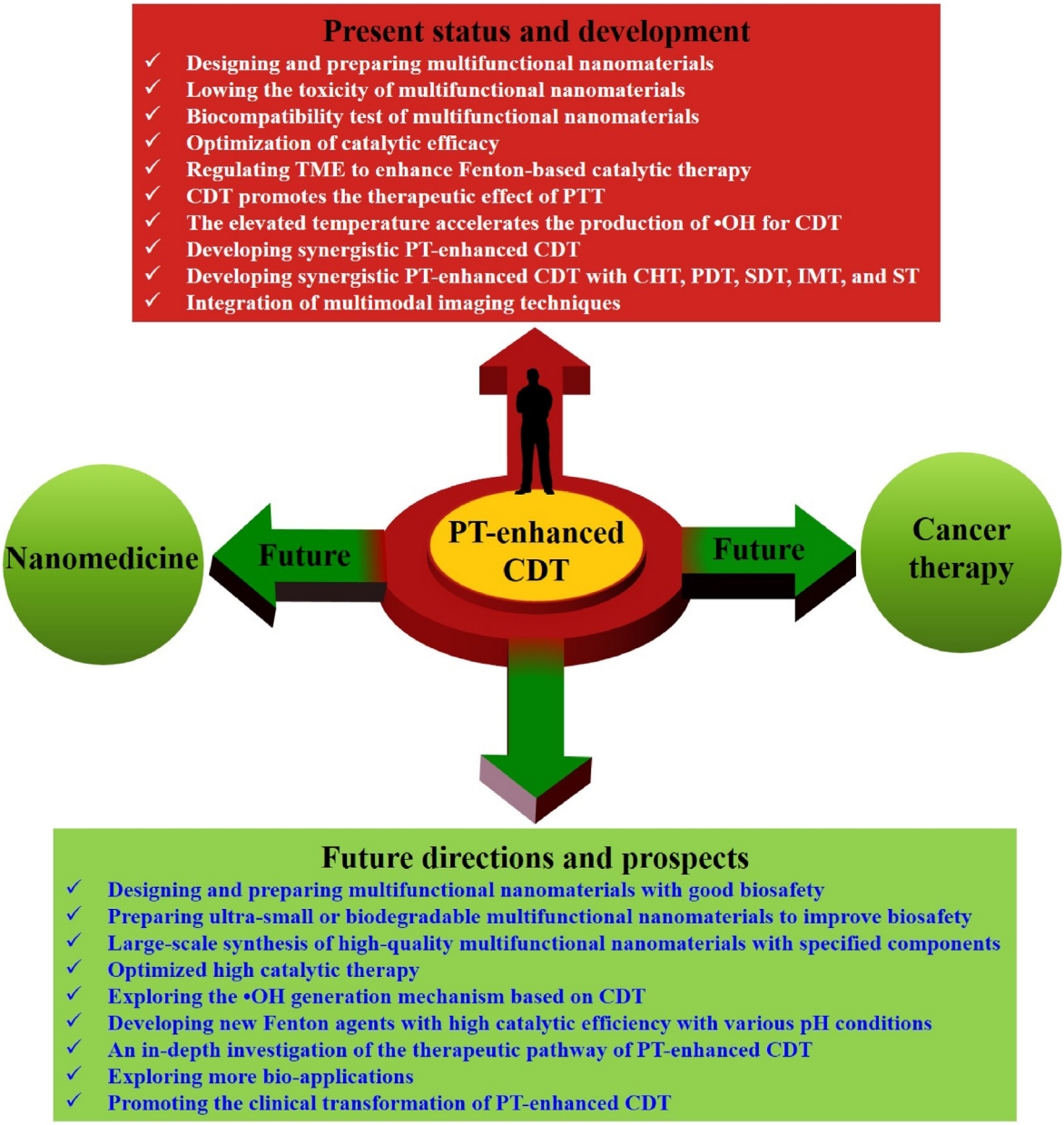


**Fig. 24.** The summative scheme of the present status/development and future directions/prospects of PT-enhanced CDT.

Fenton-catalytic efficiency, including optimizing its physical and chemical properties as well as regulating the TME. The mechanisms of •OH generation based on CDT must be further investigated. Additionally, the mildly acidic TME (pH 5.6–6.8) has a significantly less effective role in the Fenton or Fenton-like reaction and there is also an urgent need to develop new Fenton agents with high catalytic efficiency under neutral and mildly acidic pH conditions.

Fourth, the lysosomal pH and $H_2O_2$ concentration in healthy cells are also low and induce •OH production, the biocompatibility and specificity of multifunctional nanomaterials for PT-enhanced CDT urgently need to be further improved to avoid potential damage to healthy cells. Therefore, the effective tumor targeting of nanomaterials for cancer therapy remains a challenge for researchers to improve the accumulation of drugs and nanomaterials in tumors. Furthermore, there is also an urgent need to accelerate the development of diagnostic methods for PT-enhanced CDT.

Fifth, a reasonable combination of various therapeutic modalities using multifunctional nanomaterials to achieve excellent tumor treatment efficacy is still a major challenge. Although combination cancer therapy showed significantly killing efficiency of tumors, the research on combination cancer therapy is still in its infancy, and many issues still need to be further improved. Therefore, there is an urgent need to develop nanomaterials with specified components to achieve strong therapeutic effects.

Finally, the current treatment of PT-enhanced CDT has limited to the mice or other small rodents subcutaneous transplantation tumor models. Up to now, there are no reports of clinical trials involving PT-enhanced CDT. In general, PT-enhanced CDT using multifunctional nanomaterials has made significant progress and achievement in recent years. Although the emerging PT-enhanced CDT faced several problems and challenges and further development of science and technology may promote its clinical translation of PT-enhanced CDT.

After addressing several challenges, multifunctional nanomaterials

for PT-enhanced CDT may show great promise for more effective cancer treatment in future clinical applications and will pave the way for new concepts in cancer therapy.

## Declaration of competing interest

The authors declare that they have no known competing financial interests or personal relationships that could have appeared to influence the work reported in this paper.

## Acknowledgments

This research was supported by the Basic Science Research Program (2016R1D1A3B02011756) through the National Research Foundation (NRF) of Korea funded by the Ministry of Science, ICT & Future Planning and the Ministry of Science, ICT, and Future Planning (MSIP), Korea under the Information Technology Research Center (ITRC) support program (IITP-2016-H8601-16-1011) supervised by the Institute for Information & Communications Technology Promotion (IITP). This work was supported by the Global Research Laboratory Program (2014K1A1A2043032) through the National Research Foundation of Korea (NRF) grants funded by the Korean government Ministry of Science and ICT (MSIT). This work was also supported by the Korea Institute of Energy Technology Evaluation and Planning (KETEP) and the Ministry of Trade, Industry & Energy (MOTIE) of the Republic of Korea (No. 20142020200980 & 20182010600430). Prof. Eue-Soon Jang specially thanks a research grant from the Korean Ministry of Education, Science & Technology (2016R1D1A3B0201175615) and the Grand Information Technology Research Center Program (IITP-2021-2020-0-01612) through the Institute of Information & Communications Technology Planning & Evaluation (IITP) funded by the Ministry of Science and ICT (MSIT), Korea. Deanship of Scientific Research (RGP:1/275/1442) from King Khalid University, Abha, Saudi Arabia.

## References

[1] A.S. Cleary, T.L. Leonard, S.A. Gestl, E.J. Gunther, Tumour cell heterogeneity maintained by cooperating subclones in Wnt-driven mammary cancers, Nature 508 (7494) (2014) 113–117.
[2] J.L. Counihan, E.A. Grossman, D.K. Nomura, Cancer metabolism: current understanding and therapies, Chem. Rev. 118 (14) (2018) 6893–6923.
[3] P. Anand, A.B. Kunnumakara, C. Sundaram, K.B. Harikumar, S.T. Tharakan, O.S. Lai, B. Sung, B.B. Aggarwal, Cancer is a preventable disease that requires major lifestyle changes, Pharm. Res. 25 (9) (2008) 2097–2116.
[4] D. Trachootham, J. Alexandre, P. Huang, Targeting cancer cells by ROS-mediated mechanisms: a radical therapeutic approach, Nat. Rev. Drug Discov. 8 (7) (2009) 579–591.
[5] J.A. Moscow, T. Fojo, R.L. Schilsky, The evidence framework for precision cancer medicine, Nat. Rev. Clin. Oncol. 15 (3) (2018) 183–192.
[6] B. Yang, Y. Chen, J. Shi, Reactive oxygen species (ROS)-based nanomedicine, Chem. Rev. 119 (8) (2019) 4881–4985.
[7] Z. Zhang, L.M. Bragg, M.R. Servos, J. Liu, Gold nanoparticles as dehydrogenase mimicking nanozymes for estradiol degradation, Chin. Chem. Lett. 30 (9) (2019) 1655–1658.
[8] S. Yang, L. Zhou, Y. Su, R. Zhang, C.-M. Dong, One-pot photoreduction to prepare NIR-absorbing plasmonic gold nanoparticles tethered by amphiphilic polypeptide copolymer for synergistic photothermal-chemotherapy, Chin. Chem. Lett. 30 (1) (2019) 187–191.
[9] H. He, L. Liu, E.E. Morin, M. Liu, A. Schwendeman, Survey of clinical translation of cancer nanomedicines—lessons learned from successes and failures, Acc. Chem. Res. 52 (9) (2019) 2445–2461.
[10] H. Sun, Y. Dong, J. Feijen, Z. Zhong, Peptide-decorated polymeric nanomedicines for precision cancer therapy, J. Contr. Release 290 (2018) 11–27.
[11] J. Shi, P.W. Kantoff, R. Wooster, O.C. Farokhzad, Cancer nanomedicine: progress, challenges and opportunities, Nat. Rev. Cancer 17 (1) (2017) 20–37.
[12] R.S. Riley, C.H. June, R. Langer, M.J. Mitchell, Delivery technologies for cancer immunotherapy, Nat. Rev. Drug Discov. 18 (3) (2019) 175–196.
[13] L. Milling, Y. Zhang, D.J. Irvine, Delivering safer immunotherapies for cancer, Adv. Drug Deliv. Rev. 114 (2017) 79–101.
[14] J. Zhou, L. Rao, G. Yu, T.R. Cook, X. Chen, F. Huang, Supramolecular cancer nanotheranostics, Chem. Soc. Rev. 50 (4) (2021) 2839–2891.
[15] K. Ulbrich, K. Hola, V. Subr, A. Bakandritsos, J. Tucek, R. Zboril, Targeted drug delivery with polymers and magnetic nanoparticles: covalent and noncovalent approaches, release control, and clinical studies, Chem. Rev. 116 (9) (2016) 5338–5431.
[16] M.P. Stewart, A. Sharei, X. Ding, G. Sahay, R. Langer, K.F. Jensen, In vitro and ex vivo strategies for intracellular delivery, Nature 538 (7624) (2016) 183–192.
[17] T. Sabri, P.D. Pawelek, J.A. Capobianco, Dual activity of rose bengal functionalized to albumin-coated lanthanide-doped upconverting nanoparticles: targeting and photodynamic therapy, ACS Appl. Mater. Interfaces 10 (32) (2018) 26947–26953.
[18] T. Gu, L. Cheng, F. Gong, J. Xu, X. Li, G. Han, Z. Liu, Upconversion composite nanoparticles for tumor hypoxia modulation and enhanced near-infrared-triggered photodynamic therapy, ACS Appl. Mater. Interfaces 10 (18) (2018) 15494–15503.
[19] L. Cheng, C. Wang, L. Feng, K. Yang, Z. Liu, Functional nanomaterials for phototherapies of cancer, Chem. Rev. 114 (21) (2014) 10869–10939.
[20] X. Pan, H. Wang, S. Wang, X. Sun, L. Wang, W. Wang, H. Shen, H. Liu, Sonodynamic therapy (SDT): a novel strategy for cancer nanotheranostics, Sci. China Life Sci. 61 (4) (2018) 415–426.
[21] X. Dong, J. Liang, A. Yang, Z. Qian, D. Kong, F. Lv, Fluorescence imaging guided CpG nanoparticles-loaded IR820-hydrogel for synergistic photothermal immunotherapy, Biomaterials 209 (2019) 111–125.
[22] R. Liang, Y. Li, M. Huo, H. Lin, Y. Chen, Triggering sequential catalytic fenton reaction on 2D MXenes for hyperthermia-augmented synergistic nanocatalytic cancer therapy, ACS Appl. Mater. Interfaces 11 (46) (2019) 42917–42931.
[23] Q. Guo, D. Wang, G. Yang, Photoacoustic imaging guided photothermal and chemodynamic combined therapy for cancer using, J. Biomed. Nanotechnol. 15 (10) (2019) 2090–2099.
[24] P. Liu, Y. Wang, L. An, Q. Tian, J. Lin, S. Yang, Ultrasmall WO3–x@ γ-poly-l-glutamic acid nanoparticles as a photoacoustic imaging and effective photothermal-enhanced chemodynamic therapy agent for cancer, ACS Appl. Mater. Interfaces 10 (45) (2018) 38833–38844.
[25] X. Liu, Y. Liu, J. Wang, T. Wei, Z. Dai, Mild hyperthermia-enhanced enzyme-mediated tumor cell chemodynamic therapy, ACS Appl. Mater. Interfaces 11 (26) (2019) 23065–23071.
[26] W. Fan, B. Yung, P. Huang, X. Chen, Nanotechnology for multimodal synergistic cancer therapy, Chem. Rev. 117 (22) (2017) 13566–13638.
[27] Z. Tang, H. Zhang, Y. Liu, D. Ni, H. Zhang, J. Zhang, Z. Yao, M. He, J. Shi, W. Bu, Antiferromagnetic pyrite as the tumor microenvironment-mediated nanoplatform for self-enhanced tumor imaging and therapy, Adv. Mater. 29 (47) (2017) 1701683.
[28] G. Ni, G. Yang, Y. He, X. Li, T. Du, L. Xu, S. Zhou, Uniformly sized hollow microspheres loaded with polydopamine nanoparticles and doxorubicin for local chemo-photothermal combination therapy, Chem. Eng. J. 379 (2020) 122317.
[29] Z. Zheng, Q. Chen, S. Rong, R. Dai, Z. Jia, X. Peng, R. Zhang, Two-stage activated nano-truck enhanced specific aggregation and deep delivery for synergistic tumor ablation, Nanoscale 12 (29) (2020) 15845–15856.
[30] P. Lei, R. An, P. Zhang, S. Yao, S. Song, L. Dong, X. Xu, K. Du, J. Feng, H. Zhang, Ultrafast synthesis of ultrasmall poly (Vinylpyrrolidone)-protected Bismuth Nanodots as a multifunctional theranostic agent for in vivo dual-modal CT/Photothermal-imaging-guided photothermal therapy, Adv. Funct. Mater. 27 (35) (2017) 1702018.
[31] X. Wang, X. Zhong, Z. Liu, L. Cheng, Recent progress of chemodynamic therapy-induced combination cancer therapy, Nano Today 35 (2020) 100946.
[32] Y. Cheng, F. Yang, K. Zhang, Y. Zhang, Y. Cao, C. Liu, H. Lu, H. Dong, X. Zhang, Non-Fenton-type hydroxyl radical generation and photothermal effect by mitochondria-targeted WSSe/MnO2 nanocomposite loaded with isoniazid for synergistic anticancer treatment, Adv. Funct. Mater. 29 (45) (2019) 1903850.
[33] L.S. Lin, J. Song, L. Song, K. Ke, Y. Liu, Z. Zhou, Z. Shen, J. Li, Z. Yang, W. Tang, Simultaneous Fenton-like ion delivery and glutathione depletion by MnO2-based nanoagent to enhance chemodynamic therapy, Angew. Chem. 130 (18) (2018) 4996–5000.
[34] L. Lin, S. Wang, H. Deng, W. Yang, L. Rao, R. Tian, Y. Liu, G. Yu, Z. Zhou, J. Song, Endogenous labile iron pool-mediated free radical generation for cancer chemodynamic therapy, J. Am. Chem. Soc. 142 (36) (2020) 15320–15330.
[35] J. Yao, F. Zheng, C. Yao, X. Xu, O.U. Akakuru, T. Chen, F. Yang, A. Wu, Rational design of nanomedicine for photothermal-chemodynamic bimodal cancer therapy, WIRES Nanomed. Nanobi. 13 (3) (2021), e1682.
[36] Z. Tang, Y. Liu, M. He, W. Bu, Chemodynamic therapy: tumour microenvironment-mediated Fenton and Fenton-like reactions, Angew. Chem. Int. Ed. 58 (4) (2019) 946–956.
[37] B. Yang, Y. Chen, J. Shi, Nanocatalytic medicine, Adv. Mater. 31 (39) (2019) 1901778.
[38] L.-S. Lin, T. Huang, J. Song, X.-Y. Ou, Z. Wang, H. Deng, R. Tian, Y. Liu, J.-F. Wang, Y. Liu, Synthesis of copper peroxide nanodots for H2O2 self-supplying chemodynamic therapy, J. Am. Chem. Soc. 141 (25) (2019) 9937–9945.
[39] Z. Wang, X. Zhen, P.K. Upputuri, Y. Jiang, J. Lau, M. Pramanik, K. Pu, B. Xing, Redox-activatable and acid-enhanced nanotheranostics for second near-infrared photoacoustic tomography and combined photothermal tumor therapy, ACS Nano 13 (5) (2019) 5816–5825.
[40] Y. Hao, Z. Dong, M. Chen, Y. Chao, Z. Liu, L. Feng, Y. Hao, Z. Dong, M. Chen, Y. Chao, Near-infrared light and glucose dual-responsive cascading hydroxyl radical generation for in situ gelation and effective breast cancer treatment, Biomaterials 228 (2020) 119568.
[41] X. Wang, X. Zhong, H. Lei, Y. Geng, Q. Zhao, F. Gong, Z. Yang, Z. Dong, Z. Liu, L. Cheng, Hollow $Cu_2Se$ nanozymes for tumor photothermal-catalytic therapy, Chem. Mater. 31 (16) (2019) 6174–6186.
[42] X. Wang, X. Zhong, Z. Zha, G. He, Z. Miao, H. Lei, Q. Luo, R. Zhang, Z. Liu, L. Cheng, Biodegradable $CoS_2$ nanoclusters for photothermal-enhanced chemodynamic therapy, Appl. Mater. Today 18 (2020) 100464.

[43] H. Wang, L. An, C. Tao, Z. Ling, J. Lin, Q. Tian, S. Yang, A smart theranostic platform for photoacoustic and magnetic resonance dual-imaging-guided photothermal-enhanced chemodynamic therapy, Nanoscale 12 (8) (2020) 5139–5150.
[44] R. Han, S. Wu, Y. Yan, W. Chen, K. Tang, Construction of ferrocene modified and indocyanine green loaded multifunctional mesoporous silica nanoparticle for simultaneous chemodynamic/photothermal/photodynamic therapy, Mater. Today Commun. 26 (2021) 101842.
[45] X. Wang, L. Cheng, Multifunctional Prussian blue-based nanomaterials: preparation, modification, and theranostic applications, Coord. Chem. Rev. 419 (2020) 213393.
[46] P. An, Z. Gao, K. Sun, D. Gu, H. Wu, C. You, Y. Li, K. Cheng, Y. Zhang, Z. Wang, Photothermal-enhanced inactivation of glutathione peroxidase for ferroptosis sensitized by an autophagy promotor, ACS Appl. Mater. Interfaces 11 (46) (2019) 42988–42997.
[47] F. Jiang, B. Ding, S. Liang, Y. Zhao, Z. Cheng, B. Xing, J. Lin, Intelligent MoS2–CuO heterostructures with multiplexed imaging and remarkably enhanced antitumor efficacy via synergetic photothermal therapy/chemodynamic therapy/immunotherapy, Biomaterials 268 (2020) 120545.
[48] Y. Liu, W. Zhen, Y. Wang, J. Liu, L. Jin, T. Zhang, S. Zhang, Y. Zhao, S. Song, C. Li, One-dimensional $Fe_2P$ acts as a Fenton agent in response to NIR II light and ultrasound for deep tumor synergetic theranostics, Angew. Chem. 131 (8) (2019) 2429–2434.
[49] B. Poinard, S.Z.Y. Neo, E.L.L. Yeo, H.P.S. Heng, K.G. Neoh, J.C.Y. Kah, Polydopamine nanoparticles enhance drug release for combined photodynamic and photothermal therapy, ACS Appl. Mater. Interfaces 10 (25) (2018) 21125–21136.
[50] Y. Cao, X. Meng, D. Wang, K. Zhang, W. Dai, H. Dong, X. Zhang, Intelligent MnO2/Cu2–x S for multimode imaging diagnostic and advanced single-laser irradiated photothermal/photodynamic therapy, ACS Appl. Mater. Interfaces 10 (21) (2018) 17732–17741.
[51] R. Lv, P. Yang, F. He, S. Gai, C. Li, Y. Dai, G. Yang, J. Lin, A yolk-like multifunctional platform for multimodal imaging and synergistic therapy triggered by a single near-infrared light, ACS Nano 9 (2) (2015) 1630–1647.
[52] Y. Liu, P. Bhattarai, Z. Dai, X. Chen, Photothermal therapy and photoacoustic imaging via nanotheranostics in fighting cancer, Chem. Soc. Rev. 48 (7) (2019) 2053–2108.
[53] X. Huang, W. Zhang, G. Guan, G. Song, R. Zou, J. Hu, Design and functionalization of the NIR-responsive photothermal semiconductor nanomaterials for cancer theranostics, Acc. Chem. Res. 50 (10) (2017) 2529–2538.
[54] M. Abbas, Q. Zou, S. Li, X. Yan, Self-assembled peptide-and protein-based nanomaterials for antitumor photodynamic and photothermal therapy, Adv. Mater. 29 (12) (2017) 1605021.
[55] Y. Liu, W. Zhen, L. Jin, S. Zhang, G. Sun, T. Zhang, X. Xu, S. Song, Y. Wang, J. Liu, All-in-one theranostic nanoagent with enhanced reactive oxygen species generation and modulating tumor microenvironment ability for effective tumor eradication, ACS Nano 12 (5) (2018) 4886–4893.
[56] Y. Han, S. Gao, Y. Zhang, Q. Ni, Z. Li, X.-J. Liang, J. Zhang, Metal-based nanocatalyst for combined cancer therapeutics, Bioconjugate Chem. 31 (5) (2020) 1247–1258.
[57] H. Chen, Z. Gu, H. An, C. Chen, J. Chen, R. Cui, S. Chen, W. Chen, X. Chen, X. Chen, Precise nanomedicine for intelligent therapy of cancer, Sci. China Chem. 61 (12) (2018) 1503–1552.
[58] G. Guan, X. Wang, B. Li, W. Zhang, Z. Cui, X. Lu, R. Zou, J. Hu, "Transformed" Fe 3 S 4 tetragonal nanosheets: a high-efficiency and body-clearable agent for magnetic resonance imaging guided photothermal and chemodynamic synergistic therapy, Nanoscale 10 (37) (2018) 17902–17911.
[59] W. Feng, X. Han, R. Wang, X. Gao, P. Hu, W. Yue, Y. Chen, J. Shi, Nanocatalysts-augmented and photothermal-enhanced tumor-specific sequential nanocatalytic therapy in both NIR-I and NIR-II biowindows, Adv. Mater. 31 (5) (2019) 1805919.
[60] J. Cui, R. Jiang, C. Guo, X. Bai, S. Xu, L. Wang, Fluorine grafted Cu7S4–Au heterodimers for multimodal imaging guided photothermal therapy with high penetration depth, J. Am. Chem. Soc. 140 (18) (2018) 5890–5894.
[61] S. Liu, X. Pan, H. Liu, Two-dimensional nanomaterials for photothermal therapy, Angew. Chem. 132 (15) (2020) 5943–5953.
[62] X. Wang, Q. Shi, Z. Zha, D. Zhu, L. Zheng, L. Shi, X. Wei, L. Lian, K. Wu, L. Cheng, Copper single-atom catalysts with photothermal performance and enhanced nanozyme activity for bacteria-infected wound therapy, Bioact. Mater. 6 (12) (2021) 4389–4401.
[63] X. Wang, L. Fan, L. Cheng, Y. Sun, X. Wang, X. Zhong, Q. Shi, F. Gong, Y. Yang, Y. Ma, Biodegradable nickel disulfide nanozymes with GSH-depleting function for high-efficiency photothermal-catalytic antibacterial therapy, iScience 23 (7) (2020) 101281.
[64] Y. Wang, L. An, J. Lin, Q. Tian, S. Yang, A hollow $Cu_9S_8$ theranostic nanoplatform based on a combination of increased active sites and photothermal performance in enhanced chemodynamic therapy, Chem. Eng. J. 385 (2020) 123925.
[65] X. Wang, Z. Miao, Y. Ma, H. Chen, H. Qian, Z. Zha, One-pot solution synthesis of shape-controlled copper selenide nanostructures and their potential applications in photocatalysis and photothermal therapy, Nanoscale 9 (38) (2017) 14512–14519.
[66] H.S. Jung, P. Verwilst, A. Sharma, J. Shin, J.L. Sessler, J.S. Kim, Organic molecule-based photothermal agents: an expanding photothermal therapy universe, Chem. Soc. Rev. 47 (7) (2018) 2280–2297.
[67] A.G. Denkova, R.M. de Kruijff, P. Serra-Crespo, Combined photo-therapies: nanocarrier-mediated photochemotherapy and photoradiotherapy, Adv. Health. Mater. 7 (8) (2018) 1870033.
[68] Z. Gu, S. Zhu, L. Yan, F. Zhao, Y. Zhao, Graphene-based smart platforms for combined Cancer therapy, Adv. Mater. 31 (9) (2019) 1800662.
[69] X. Yang, X. Cheng, A.A. Elzatahry, J. Chen, A. Alghamdi, Y. Deng, Recyclable Fenton-like catalyst based on zeolite Y supported ultrafine, highly-dispersed Fe2O3 nanoparticles for removal of organics under mild conditions, Chin. Chem. Lett. 30 (2) (2019) 324–330.
[70] Q. Tian, M. Tang, Y. Sun, R. Zou, Z. Chen, M. Zhu, S. Yang, J. Wang, J. Wang, J. Hu, Hydrophilic flower-like CuS superstructures as an efficient 980 nm laser-driven photothermal agent for ablation of cancer cells, Adv. Mater. 23 (31) (2011) 3542–3547.
[71] F. Jiang, Q. Tian, M. Tang, Z. Chen, J. Yang, J. Hu, One-pot synthesis of large-scaled Janus Ag–Ag 2 S nanoparticles and their photocatalytic properties, CrystEngComm 13 (24) (2011) 7189–7193.
[72] P. An, F. Fan, D. Gu, Z. Gao, A.M.S. Hossain, B. Sun, Photothermal-reinforced and glutathione-triggered in Situ cascaded nanocatalytic therapy, J. Contr. Release 321 (2020) 734–743.
[73] S. He, J. Song, J. Qu, Z. Cheng, Crucial breakthrough of second near-infrared biological window fluorophores: design and synthesis toward multimodal imaging and theranostics, Chem. Soc. Rev. 47 (12) (2018) 4258–4278.
[74] X. Qian, J. Zhang, Z. Gu, Y. Chen, Nanocatalysts-augmented Fenton chemical reaction for nanocatalytic tumor therapy, Biomaterials 211 (2019) 1–13.
[75] K. Fan, C. Cao, Y. Pan, D. Lu, D. Yang, J. Feng, L. Song, M. Liang, X. Yan, Magnetoferritin nanoparticles for targeting and visualizing tumour tissues, Nat. Nanotechnol. 7 (7) (2012) 459–464.
[76] L. Gao, J. Zhuang, L. Nie, J. Zhang, Y. Zhang, N. Gu, T. Wang, J. Feng, D. Yang, S. Perrett, Intrinsic peroxidase-like activity of ferromagnetic nanoparticles, Nat. Nanotechnol. 2 (9) (2007) 577–583.
[77] Z. Shen, J. Song, B.C. Yung, Z. Zhou, A. Wu, X. Chen, Emerging strategies of cancer therapy based on ferroptosis, Adv. Mater. 30 (12) (2018) 1704007.
[78] M. Saeed, W. Ren, A. Wu, Therapeutic applications of iron oxide based nanoparticles in cancer: basic concepts and recent advances, Biomater. Sci. 6 (4) (2018) 708–725.
[79] Z. Shen, T. Liu, Y. Li, J. Lau, Z. Yang, W. Fan, Z. Zhou, C. Shi, C. Ke, V.I. Bregadze, Fenton-reaction-acceleratable magnetic nanoparticles for ferroptosis therapy of orthotopic brain tumors, ACS Nano 12 (11) (2018) 11355–11365.
[80] C.C. Winterbourn, Toxicity of iron and hydrogen peroxide: the Fenton reaction, Toxicol. Lett. 82 (1995) 969–974.
[81] M. Liu, B. Liu, Q. Liu, K. Du, Z. Wang, N. He, Nanomaterial-induced ferroptosis for cancer specific therapy, Coord. Chem. Rev. 382 (2019) 160–180.
[82] S.J. Dixon, B.R. Stockwell, The role of iron and reactive oxygen species in cell death, Nat. Chem. Biol. 10 (1) (2014) 9–17.
[83] J.X. Fan, M.Y. Peng, H. Wang, H.R. Zheng, Z.L. Liu, C.X. Li, X.N. Wang, X.H. Liu, S.X. Cheng, X.Z. Zhang, Engineered bacterial bioreactor for tumor therapy via Fenton-like reaction with localized H2O2 generation, Adv. Mater. 31 (16) (2019) 1808278.
[84] X. Yao, P. Yang, Z. Jin, Q. Jiang, R. Guo, R. Xie, Q. He, W. Yang, Multifunctional nanoplatform for photoacoustic imaging-guided combined therapy enhanced by CO induced ferroptosis, Biomaterials 197 (2019) 268–283.
[85] P. Zhao, Z. Tang, X. Chen, Z. He, X. He, M. Zhang, Y. Liu, D. Ren, K. Zhao, W. Bu, Ferrous-cysteine–phosphotungstate nanoagent with neutral pH fenton reaction activity for enhanced cancer chemodynamic therapy, Mater. Horiz. 6 (2) (2019) 369–374.
[86] H. Ranji-Burachaloo, P.A. Gurr, D.E. Dunstan, G.G. Qiao, Cancer treatment through nanoparticle-facilitated fenton reaction, ACS Nano 12 (12) (2018) 11819–11837.
[87] C. Zhang, W. Bu, D. Ni, S. Zhang, Q. Li, Z. Yao, J. Zhang, H. Yao, Z. Wang, J. Shi, Synthesis of iron nanometallic glasses and their application in cancer therapy by a localized Fenton reaction, Angew. Chem. Int. Ed. 55 (6) (2016) 2101–2106.
[88] Y. Zhu, R. Zhu, Y. Xi, J. Zhu, G. Zhu, H. He, Strategies for enhancing the heterogeneous Fenton catalytic reactivity: a review, Appl. Catal. B Environ. 255 (2019) 117739.
[89] W. Wu, L. Yu, Q. Jiang, M. Huo, H. Lin, L. Wang, Y. Chen, J. Shi, Enhanced tumor-specific disulfiram chemotherapy by in situ Cu2+ chelation-initiated nontoxicity-to-toxicity transition, J. Am. Chem. Soc. 141 (29) (2019) 11531–11539.
[90] X. Meng, X. Zhang, M. Liu, B. Cai, N. He, Z. Wang, Fenton reaction-based nanomedicine in cancer chemodynamic and synergistic therapy, Appl. Mater. Today 21 (2020) 100864.
[91] S. Anandan, M. Miyauchi, Ce-doped ZnO (Ce x Zn 1− x O) becomes an efficient visible-light-sensitive photocatalyst by co-catalyst (Cu 2+) grafting, Phys. Chem. Chem. Phys. 13 (33) (2011) 14937–14945.
[92] T. Rae, P. Schmidt, R. Pufahl, V. Culotta, T. O'halloran, Undetectable intracellular free copper: the requirement of a copper chaperone for superoxide dismutase, Science 284 (5415) (1999) 805–808.
[93] C. Yao, W. Wang, P. Wang, M. Zhao, X. Li, F. Zhang, Near-infrared upconversion mesoporous cerium oxide hollow biophotocatalyst for concurrent pH-/H2O2-responsive O2-evolving synergetic cancer therapy, Adv. Mater. 30 (7) (2018) 1704833.
[94] M. Umar, H.A. Aziz, M.S. Yusoff, Trends in the use of Fenton, electro-Fenton and photo-Fenton for the treatment of landfill leachate, Waste Manag. 30 (11) (2010) 2113–2121.
[95] Z. Lei, X. Zhang, X. Zheng, S. Liu, Z. Xie, Porphyrin–ferrocene conjugates for photodynamic and chemodynamic therapy, Org. Biomol. Chem. 16 (44) (2018) 8613–8619.
[96] J. Kim, H.R. Cho, H. Jeon, D. Kim, C. Song, N. Lee, S.H. Choi, T. Hyeon, Continuous O2-evolving MnFe2O4 nanoparticle-anchored mesoporous silica

nanoparticles for efficient photodynamic therapy in hypoxic cancer, J. Am. Chem. Soc. 139 (32) (2017) 10992–10995.
[97] X. Wu, H. Zhang, Y. Li, D. Zhang, X. Li, Factorial design analysis for COD removal from landfill leachate by photoassisted Fered-Fenton process, Environ. Sci. Pollut. Res. 21 (14) (2014) 8595–8602.
[98] Y. Liu, D. Tu, H. Zhu, X. Chen, Lanthanide-doped luminescent nanoprobes: controlled synthesis, optical spectroscopy, and bioapplications, Chem. Soc. Rev. 42 (16) (2013) 6924–6958.
[99] Y.-N. Hao, W.-X. Zhang, Y.-R. Gao, Y.-N. Wei, Y. Shu, J.-H. Wang, State-of-the-art advances of copper-based nanostructures in the enhancement of chemodynamic therapy, J. Mater. Chem. B 9 (2) (2021) 250–266.
[100] S. Khan, M. Sharifi, S.H. Bloukh, Z. Edis, R. Siddique, M. Falahati, In vivo guiding inorganic nanozymes for biosensing and therapeutic potential in cancer, inflammation and microbial infections, Talanta 224 (2020) 121805.
[101] K.-T. Lee, Y.-J. Lu, F.-L. Mi, T. Burnouf, Y.-T. Wei, S.-C. Chiu, E.-Y. Chuang, S.-Y. Lu, Catalase-modulated heterogeneous Fenton reaction for selective cancer cell eradication: SnFe2O4 nanocrystals as an effective reagent for treating lung cancer cells, ACS Appl. Mater. Interfaces 9 (2) (2017) 1273–1279.
[102] X. Wang, X. Zhong, L. Cheng, Titanium-based nanomaterials for cancer theranostics, Coord. Chem. Rev. 430 (2021) 213662.
[103] W. Wang, Y. Jin, Z. Xu, X. Liu, S.Z. Bajwa, W.S. Khan, H. Yu, Stimuli-activatable nanomedicines for chemodynamic therapy of cancer, WIRES Nanomed. Nanobi. 12 (4) (2020) e1614.
[104] T. Xue, C. Xu, Y. Wang, Y. Wang, H. Tian, Y. Zhang, Doxorubicin-loaded nanoscale metal–organic framework for tumor-targeting combined chemotherapy and chemodynamic therapy, Biomater. Sci. 7 (11) (2019) 4615–4623.
[105] B. Yang, Y. Chen, J. Shi, Nanocatalytic medicine, Adv. Mater. 31 (39) (2019) 1901778.
[106] Z. Yang, Y. Dai, C. Yin, Q. Fan, W. Zhang, J. Song, G. Yu, W. Tang, W. Fan, B.C. Yung, Activatable semiconducting theranostics: simultaneous generation and ratiometric photoacoustic imaging of reactive oxygen species in vivo, Adv. Mater. 30 (23) (2018) 1707509.
[107] A.D. Bokare, W. Choi, Review of iron-free Fenton-like systems for activating H2O2 in advanced oxidation processes, J. Hazard Mater. 275 (2014) 121–135.
[108] E. Neyens, J. Baeyens, A review of classic Fenton's peroxidation as an advanced oxidation technique, J. Hazard Mater. 98 (1–3) (2003) 33–50.
[109] Q. Chen, Y. Luo, W. Du, Z. Liu, S. Zhang, J. Yang, H. Yao, T. Liu, M. Ma, H. Chen, Clearable theranostic platform with a pH-independent chemodynamic therapy enhancement strategy for synergetic photothermal tumor therapy, ACS Appl. Mater. Interfaces 11 (20) (2019) 18133–18144.
[110] Q. Tian, L. An, J. Lin, S. Yang, Ellagic acid-Fe@ BSA nanoparticles for endogenous H2S accelerated Fe (III)/Fe (II) conversion and photothermal synergistically enhanced chemodynamic therapy, Theranostics 10 (9) (2020) 4101–4115.
[111] F. Liu, L. Lin, Y. Zhang, Y. Wang, S. Sheng, C. Xu, H. Tian, X. Chen, A tumor-microenvironment-activated nanozyme-mediated theranostic nanoreactor for imaging-guided combined tumor therapy, Adv. Mater. 31 (40) (2019) 1902885.
[112] Y. Wang, J. Zhao, Z. Chen, F. Zhang, Q. Wang, W. Guo, K. Wang, H. Lin, F. Qu, Construct of MoSe2/Bi2Se3 nanoheterostructure: multimodal CT/PT imaging-guided PTT/PDT/chemotherapy for cancer treating, Biomaterials 217 (2019) 119282.
[113] Z. Xie, S. Liang, X. Cai, B. Ding, S. Huang, Z. Hou, P.a. Ma, Z. Cheng, J. Lin, O2-Cu/ZIF-8@ Ce6/ZIF-8@ F127 composite as a tumor microenvironment-responsive nanoplatform with enhanced photo-/chemodynamic antitumor efficacy, ACS Appl. Mater. Interfaces 11 (35) (2019) 31671–31680.
[114] W. Zhou, H. Guan, K. Sun, Y. Xing, J. Zhang, FeOOH/polypyrrole nanocomposites with an islands-in-sea structure toward combined photothermal/chemodynamic therapy, ACS Appl. Bio Mater. 2 (7) (2019) 2708–2714.
[115] G. Zhao, H. Wu, R. Feng, D. Wang, P. Xu, P. Jiang, K. Yang, H. Wang, Z. Guo, Q. Chen, Novel metal polyphenol framework for MR imaging-guided photothermal therapy, ACS Appl. Mater. Interfaces 10 (4) (2018) 3295–3304.
[116] M. Huo, L. Wang, Y. Wang, Y. Chen, J. Shi, Nanocatalytic tumor therapy by single-atom catalysts, ACS Nano 13 (2) (2019) 2643–2653.
[117] S. Gao, X. Lu, P. Zhu, H. Lin, L. Yu, H. Yao, C. Wei, Y. Chen, J. Shi, Self-evolved hydrogen peroxide boosts photothermal-promoted tumor-specific nanocatalytic therapy, J. Mater. Chem. B 7 (22) (2019) 3599–3609.
[118] F. Liu, L. Lin, S. Sheng, C. Xu, Y. Wang, Y. Zhang, D. Wang, J. Wu, Y. Li, H. Tian, A glutathione-depleting chemodynamic therapy agent with photothermal and photoacoustic properties for tumor theranostics, Nanoscale 12 (3) (2020) 1349–1355.
[119] S. Dong, Y. Dong, T. Jia, F. Zhang, Z. Wang, L. Feng, Q. Sun, S. Gai, P. Yang, Sequential catalytic, magnetic targeting nanoplatform for synergistic photothermal and NIR-enhanced chemodynamic therapy, Chem. Mater. 32 (23) (2020) 9868–9881.
[120] S. Xiao, Y. Lu, M. Feng, M. Dong, Z. Cao, X. Zhang, Y. Chen, J. Liu, Multifunctional $FeS_2$ theranostic nanoparticles for photothermal-enhanced chemodynamic/photodynamic cancer therapy and photoacoustic imaging, Chem. Eng. J. 396 (2020) 125294.
[121] S. Wang, L. Yang, H.-Y. Cho, S.-T.D. Chueng, H. Zhang, Q. Zhang, K.-B. Lee, Programmed degradation of a hierarchical nanoparticle with redox and light responsivity for self-activated photo-chemical enhanced chemodynamic therapy, Biomaterials 224 (2019) 119498.
[122] D. She, S. Peng, L. Liu, H. Huang, Y. Zheng, Y. Lu, D. Geng, B. Yin, Biomimic FeS2 nanodrug with hypothermal photothermal effect by clinical approved NIR-II light for augmented chemodynamic therapy, Chem. Eng. J. 400 (2020) 125933.
[123] Y. Shi, J. Zhang, H. Huang, C. Cao, J. Yin, W. Xu, W. Wang, X. Song, Y. Zhang, X. Dong, Fe-Doped polyoxometalate as acid-aggregated nanoplatform for NIR-II photothermal-enhanced chemodynamic therapy, Adv. Health. Mater. 9 (9) (2020) 2000005.
[124] Z. Hu, S. Wang, Z. Dai, H. Zhang, X. Zheng, A novel theranostic nano-platform (PB@ FePt–HA-g-PEG) for tumor chemodynamic–photothermal co-therapy and triple-modal imaging (MR/CT/PI) diagnosis, J. Mater. Chem. B 8 (24) (2020) 5351–5360.
[125] Y. Chen, M. Gao, L. Zhang, E. Ha, X. Hu, R. Zou, L. Yan, J. Hu, Tumor microenvironment responsive biodegradable Fe-doped MoOx nanowires for magnetic resonance imaging guided photothermal-enhanced chemodynamic synergistic antitumor therapy, Adv. Health. Mater. 10 (2020) 2001665.
[126] H. Zheng, S. Wang, L. Zhou, X. He, Z. Cheng, F. Cheng, Z. Liu, X. Wang, Y. Chen, Q. Zhang, Injectable multi-responsive micelle/nanocomposite hybrid hydrogel for bioenzyme and photothermal augmented chemodynamic therapy of skin cancer and bacterial infection, Chem. Eng. J. 404 (2020) 126439.
[127] S. Zhang, L. Jin, J. Liu, Y. Liu, T. Zhang, Y. Zhao, N. Yin, R. Niu, X. Li, D. Xue, Boosting chemodynamic therapy by the synergistic effect of Co-catalyze and photothermal effect triggered by the second near-infrared light, Nano-Micro Lett. 12 (1) (2020) 1–13.
[128] Y. Zhao, B. Ding, X. Xiao, F. Jiang, M. Wang, Z. Hou, B. Xing, B. Teng, Z. Cheng, P.a. Ma, Virus-like Fe3O4@ Bi2S3 nanozymes with resistance-free apoptotic hyperthermia-augmented nanozymitic activity for enhanced synergetic cancer therapy, ACS Appl. Mater. Interfaces 12 (10) (2020) 11320–11328.
[129] P. An, D. Gu, Z. Gao, F. Fan, Y. Jiang, B. Sun, Hypoxia-augmented and photothermally-enhanced ferroptotic therapy with high specificity and efficiency, J. Mater. Chem. B 8 (1) (2020) 78–87.
[130] Y. Liu, J. Wu, Y. Jin, W. Zhen, Y. Wang, J. Liu, L. Jin, S. Zhang, Y. Zhao, S. Song, Copper (I) phosphide nanocrystals for in situ self-generation magnetic resonance imaging-guided photothermal-enhanced chemodynamic synergetic therapy resisting deep-seated tumor, Adv. Funct. Mater. 29 (50) (2019) 1904678.
[131] C. Yang, M.R. Younis, J. Zhang, J. Qu, J. Lin, P. Huang, Programmable NIR-II photothermal-enhanced starvation-primed chemodynamic therapy using glucose oxidase-functionalized ancient pigment nanosheets, Small 16 (25) (2020) 2001518.
[132] W. Li, S. Wang, C. Ren, P. Liu, Q. Lu, L. Yang, Y. Song, M. Xu, F. Tan, M. Yu, Exo/endogenous dual-augmented chemodynamic therapy based on bio-reducible and bio-breakable copper (II)-based truncated octahedron, Chem. Eng. J. 396 (2020) 125280.
[133] F. Jiang, B. Ding, Y. Zhao, S. Liang, Z. Cheng, B. Xing, B. Teng, J. Lin, Biocompatible CuO-decorated carbon nanoplatforms for multiplexed imaging and enhanced antitumor efficacy via combined photothermal therapy/chemodynamic therapy/chemotherapy, Sci. China Mater. 63 (9) (2020) 1818–1830.
[134] M. Chang, M. Wang, M. Wang, M. Shu, B. Ding, C. Li, M. Pang, S. Cui, Z. Hou, J. Lin, A multifunctional Cascade bioreactor based on hollow-structured Cu2MoS4 for synergetic cancer chemo-dynamic therapy/starvation therapy/phototherapy/immunotherapy with remarkably enhanced efficacy, Adv. Mater. 31 (51) (2019) 1905271.
[135] H. Sun, Y. Zhang, S. Chen, R. Wang, Q. Chen, J. Li, Y. Luo, X. Wang, H. Chen, Photothermal fenton nanocatalysts for synergetic cancer therapy in the second near-infrared window, ACS Appl. Mater. Interfaces 12 (27) (2020) 30145–30154.
[136] G. Qi, Y. Zhang, J. Wang, D. Wang, B. Wang, H. Li, Y. Jin, Smart plasmonic nanozyme enhances combined chemo-photothermal cancer therapy and reveals tryptophan metabolic apoptotic pathway, Anal. Chem. 91 (19) (2019) 12203–12211.
[137] L. Fan, X. Xu, C. Zhu, J. Han, L. Gao, J. Xi, R. Guo, Tumor catalytic–photothermal therapy with yolk–shell gold@ carbon nanozymes, ACS Appl. Mater. Interfaces 10 (5) (2018) 4502–4511.
[138] M. Wang, M. Chang, Q. Chen, D. Wang, C. Li, Z. Hou, J. Lin, D. Jin, B. Xing, Au2Pt-PEG-Ce6 nanoformulation with dual nanozyme activities for synergistic chemodynamic therapy/phototherapy, Biomaterials 252 (2020) 120093.
[139] Y. Dong, S. Dong, Z. Wang, L. Feng, Q. Sun, G. Chen, F. He, S. Liu, W. Li, P. Yang, Multimode imaging-guided photothermal/chemodynamic synergistic therapy nanoagent with a tumor microenvironment responded effect, ACS Appl. Mater. Interfaces 12 (47) (2020) 52479–52491.
[140] J. Gao, H. Gu, B. Xu, Multifunctional magnetic nanoparticles: design, synthesis, and biomedical applications, Acc. Chem. Res. 42 (8) (2009) 1097–1107.
[141] V.I. Shubayev, T.R. Pisanic II, S. Jin, Magnetic nanoparticles for theragnostics, Adv. Drug Deliv. Rev. 61 (6) (2009) 467–477.
[142] A.H. Lu, E.e.L. Salabas, F. Schüth, Magnetic nanoparticles: synthesis, protection, functionalization, and application, Angew. Chem. Int. Ed. 46 (8) (2007) 1222–1244.
[143] S. Laurent, D. Forge, M. Port, A. Roch, C. Robic, L. Vander Elst, R.N. Muller, Magnetic iron oxide nanoparticles: synthesis, stabilization, vectorization, physicochemical characterizations, and biological applications, Chem. Rev. 108 (6) (2008) 2064–2110.
[144] D.E. Dolmans, D. Fukumura, R.K. Jain, Photodynamic therapy for cancer, Nat. Rev. Cancer 3 (5) (2003) 380–387.
[145] H. Xu, X. Zhang, R. Han, P. Yang, H. Ma, Y. Song, Z. Lu, W. Yin, X. Wu, H. Wang, Nanoparticles in sonodynamic therapy: state of the art review, RSC Adv. 6 (56) (2016) 50697–50705.
[146] C. Corot, P. Robert, J.-M. Idée, M. Port, Recent advances in iron oxide nanocrystal technology for medical imaging, Adv. Drug Deliv. Rev. 58 (14) (2006) 1471–1504.
[147] C. Klenk, R. Gawande, L. Uslu, A. Khurana, D. Qiu, A. Quon, J. Donig, J. Rosenberg, S. Luna-Fineman, M. Moseley, Ionising radiation-free whole-body MRI versus 18F-fluorodeoxyglucose PET/CT scans for children and young adults with cancer: a prospective, non-randomised, single-centre study, Lancet Oncol. 15 (3) (2014) 275–285.

[148] C. Ansari, G.A. Tikhomirov, S.H. Hong, R.A. Falconer, P.M. Loadman, J.H. Gill, R. Castaneda, F.K. Hazard, L. Tong, O.D. Lenkov, Development of novel tumor-targeted theranostic nanoparticles activated by membrane-type matrix metalloproteinases for combined cancer magnetic resonance imaging and therapy, Small 10 (3) (2014) 566–575.
[149] S. Fütterer, I. Andrusenko, U. Kolb, W. Hofmeister, P. Langguth, Structural characterization of iron oxide/hydroxide nanoparticles in nine different parenteral drugs for the treatment of iron deficiency anaemia by electron diffraction (ED) and X-ray powder diffraction (XRPD), J. Pharm. Biomed. Anal. 86 (2013) 151–160.
[150] B. Du, X. Jiang, A. Das, Q. Zhou, M. Yu, R. Jin, J. Zheng, Glomerular barrier behaves as an atomically precise bandpass filter in a sub-nanometre regime, Nat. Nanotechnol. 12 (11) (2017) 1096–1102.
[151] B. Du, M. Yu, J. Zheng, Transport and interactions of nanoparticles in the kidneys, Nat. Rev. Mater. 3 (10) (2018) 358–374.
[152] G. Guo, H. Zhang, H. Shen, C. Zhu, R. He, J. Tang, Y. Wang, X. Jiang, J. Wang, W. Bu, Space-selective chemodynamic therapy of CuFe5O8 nanocubes for implant-related infections, ACS Nano 14 (10) (2020) 13391–13405.
[153] T. Liu, B. Xiao, F. Xiang, J. Tan, Z. Chen, X. Zhang, C. Wu, Z. Mao, G. Luo, X. Chen, Ultrasmall copper-based nanoparticles for reactive oxygen species scavenging and alleviation of inflammation related diseases, Nat. Commun. 11 (1) (2020) 1–16.
[154] Z.C. Wu, W.P. Li, C.H. Luo, C.H. Su, C.S. Yeh, Rattle-type Fe3O4@ CuS developed to conduct magnetically guided photoinduced hyperthermia at first and second NIR biological windows, Adv. Funct. Mater. 25 (41) (2015) 6527–6537.
[155] C.-C. Huang, P.-Y. Chang, C.-L. Liu, J.-P. Xu, S.-P. Wu, W.-C. Kuo, New insight on optical and magnetic Fe 3 O 4 nanoclusters promising for near infrared theranostic applications, Nanoscale 7 (29) (2015) 12689–12697.
[156] S.L. Li, P. Jiang, F.L. Jiang, Y. Liu, Recent advances in nanomaterial-based nanoplatforms for chemodynamic cancer therapy, Adv. Funct. Mater. 31 (22) (2021) 2100243.
[157] J.Y. Uriu-Adams, C.L. Keen, Copper, oxidative stress, and human health, Mol. Aspect. Med. 26 (4–5) (2005) 268–298.
[158] M.P. Rayman, Selenium in cancer prevention: a review of the evidence and mechanism of action, Proc. Nutr. Soc. 64 (4) (2005) 527–542.
[159] X. Ding, C.H. Liow, M. Zhang, R. Huang, C. Li, H. Shen, M. Liu, Y. Zou, N. Gao, Z. Zhang, Surface plasmon resonance enhanced light absorption and photothermal therapy in the second near-infrared window, J. Am. Chem. Soc. 136 (44) (2014) 15684–15693.
[160] A. Li, X. Li, X. Yu, W. Li, R. Zhao, X. An, D. Cui, X. Chen, W. Li, Synergistic thermoradiotherapy based on PEGylated Cu3BiS3 ternary semiconductor nanorods with strong absorption in the second near-infrared window, Biomaterials 112 (2017) 164–175.
[161] X. Zhao, Z. Bao, C. Sun, D. Xue, Polymorphology formation of Cu2O: a microscopic understanding of single crystal growth from both thermodynamic and kinetic models, J. Cryst. Growth 311 (3) (2009) 711–715.
[162] H. Zheng, L. Qin, H. Lin, M. Nie, Y. Li, Q. Li, Convenient route to well-dispersed Cu2O nanospheres and their use as photocatalysts, J. Nanosci. Nanotechnol. 15 (8) (2015) 6063–6068.
[163] L. Gou, C.J. Murphy, Controlling the size of Cu 2 O nanocubes from 200 to 25 nm, J. Mater. Chem. 14 (4) (2004) 735–738.
[164] M. Sharifi, S.H. Hosseinali, P. Yousefvand, A. Salihi, M.S. Shekha, F.M. Aziz, A. JouyaTalaei, A. Hasan, M. Falahati, Gold nanozyme: biosensing and therapeutic activities, Mater. Sci. Eng. C 108 (2020) 110422.
[165] M. Hu, J. Chen, Z.-Y. Li, L. Au, G.V. Hartland, X. Li, M. Marquez, Y. Xia, Gold nanostructures: engineering their plasmonic properties for biomedical applications, Chem. Soc. Rev. 35 (11) (2006) 1084–1094.
[166] Y. Huang, P. Huang, J. Lin, Plasmonic gold nanovesicles for biomedical applications, Small Methods 3 (3) (2019) 1800394.
[167] D. Hernández-Sánchez, G. Villabona-Leal, I. Saucedo-Orozco, V. Bracamonte, E. Pérez, C. Bittencourt, M. Quintana, Stable graphene oxide–gold nanoparticle platforms for biosensing applications, Phys. Chem. Chem. Phys. 20 (3) (2018) 1685–1692.
[168] M.M. Phiri, D.W. Mulder, B.C. Vorster, Seedless gold nanostars with seed-like advantages for biosensing applications, R. Soc. Open Sci. 6 (2) (2019) 181971.
[169] A. Hasan, M. Nurunnabi, M. Morshed, A. Paul, A. Polini, T. Kuila, M. Al Hariri, Y.-k. Lee, A.A. Jaffa, Recent advances in application of biosensors in tissue engineering, BioMed Res. Int. 2014 (2014) 1–18.
[170] J.R. Ashton, K.D. Castle, Y. Qi, D.G. Kirsch, J.L. West, C.T. Badea, Dual-energy CT imaging of tumor liposome delivery after gold nanoparticle-augmented radiation therapy, Theranostics 8 (7) (2018) 1782–1797.
[171] H. Wei, E. Wang, Nanomaterials with enzyme-like characteristics (nanozymes): next-generation artificial enzymes, Chem. Soc. Rev. 42 (14) (2013) 6060–6093.
[172] J. Wu, S. Li, H. Wei, Multifunctional nanozymes: enzyme-like catalytic activity combined with magnetism and surface plasmon resonance, Nanoscale Horizon 3 (4) (2018) 367–382.
[173] J. Feng, P. Huang, S. Shi, K.-Y. Deng, F.-Y. Wu, Colorimetric detection of glutathione in cells based on peroxidase-like activity of gold nanoclusters: a promising powerful tool for identifying cancer cells, Anal. Chim. Acta 967 (2017) 64–69.
[174] A.N. Koo, K.H. Min, H.J. Lee, S.-U. Lee, K. Kim, I.C. Kwon, S.H. Cho, S.Y. Jeong, S.C. Lee, Tumor accumulation and antitumor efficacy of docetaxel-loaded core-shell-corona micelles with shell-specific redox-responsive cross-links, Biomaterials 33 (5) (2012) 1489–1499.
[175] L. Wen, L. Chen, S. Zheng, J. Zeng, G. Duan, Y. Wang, G. Wang, Z. Chai, Z. Li, M. Gao, Ultrasmall biocompatible WO3− x nanodots for multi-modality imaging and combined therapy of cancers, Adv. Mater. 28 (25) (2016) 5072–5079.
[176] Z. Zhou, B. Kong, C. Yu, X. Shi, M. Wang, W. Liu, Y. Sun, Y. Zhang, H. Yang, S. Yang, Tungsten oxide nanorods: an efficient nanoplatform for tumor CT imaging and photothermal therapy, Sci. Rep. 4 (1) (2014) 1–10.
[177] Y. Bu, Z. Chen, C. Sun, Highly efficient Z-Scheme Ag3PO4/Ag/WO3− x photocatalyst for its enhanced photocatalytic performance, Appl. Catal., B 179 (2015) 363–371.
[178] F. Gong, L. Cheng, N. Yang, Q. Jin, L. Tian, M. Wang, Y. Li, Z. Liu, Bimetallic oxide MnMoOX nanorods for in vivo photoacoustic imaging of GSH and tumor-specific photothermal therapy, Nano Lett. 18 (9) (2018) 6037–6044.
[179] L. Gong, L. Yan, R. Zhou, J. Xie, W. Wu, Z. Gu, Two-dimensional transition metal dichalcogenide nanomaterials for combination cancer therapy, J. Mater. Chem. B 5 (10) (2017) 1873–1895.
[180] C. Wang, W. Fan, Z. Zhang, Y. Wen, L. Xiong, X. Chen, Advanced nanotechnology leading the way to multimodal imaging-guided precision surgical therapy, Adv. Mater. 31 (49) (2019) 1904329.
[181] M. Sun, L. Xu, W. Ma, X. Wu, H. Kuang, L. Wang, C. Xu, Hierarchical plasmonic nanorods and upconversion core–satellite nanoassemblies for multimodal imaging-guided combination phototherapy, Adv. Mater. 28 (5) (2016) 898–904.
[182] R. Pushpalatha, S. Selvamuthukumar, D. Kilimozhi, Cross-linked, cyclodextrin-based nanosponges for curcumin delivery-Physicochemical characterization, drug release, stability and cytotoxicity, J. Drug Deliv. Sci. Technol. 45 (2018) 45–53.
[183] S. Wang, Z. Wang, G. Yu, Z. Zhou, O. Jacobson, Y. Liu, Y. Ma, F. Zhang, Z.Y. Chen, X. Chen, Tumor-specific drug release and reactive oxygen species generation for cancer chemo/chemodynamic combination therapy, Adv. Sci. 6 (5) (2019) 1801986.
[184] S.-Y. Qin, A.-Q. Zhang, S.-X. Cheng, L. Rong, X.-Z. Zhang, Drug self-delivery systems for cancer therapy, Biomaterials 112 (2017) 234–247.
[185] W.-H. Lee, C.-Y. Loo, D. Traini, P.M. Young, Inhalation of nanoparticle-based drug for lung cancer treatment: advantages and challenges, Asian J. Pharm. Sci. 10 (6) (2015) 481–489.
[186] Q. Wu, Z. Yang, Y. Nie, Y. Shi, D. Fan, Multi-drug resistance in cancer chemotherapeutics: mechanisms and lab approaches, Cancer Lett. 347 (2) (2014) 159–166.
[187] K. Islam, T. Anggondowati, P. Deviany, J. Ryan, A. Fetrick, D. Bagenda, M. Copur, A. Tolentino, I. Vaziri, H. McKean, Patient preferences of chemotherapy treatment options and tolerance of chemotherapy side effects in advanced stage lung cancer, BMC Cancer 19 (1) (2019) 1–9.
[188] T. Mikoshiba, H. Ozawa, S. Saito, Y. Ikari, N. Nakahara, F. Ito, Y. Watanabe, M. Sekimizu, Y. Imanishi, K. Ogawa, Usefulness of hematological inflammatory markers in predicting severe side-effects from induction chemotherapy in head and neck cancer patients, Anticancer Res. 39 (6) (2019) 3059–3065.
[189] V. Schirrmacher, From chemotherapy to biological therapy: a review of novel concepts to reduce the side effects of systemic cancer treatment, Int. J. Oncol. 54 (2) (2019) 407–419.
[190] Y.Y. Su, Z. Teng, H. Yao, S.J. Wang, Y. Tian, Y.L. Zhang, W.F. Liu, W. Tian, L.J. Zheng, N. Lu, A multifunctional PB@ mSiO2–PEG/DOX nanoplatform for combined photothermal–chemotherapy of tumor, ACS Appl. Mater. Interfaces 8 (27) (2016) 17038–17046.
[191] B. Kim, E. Lee, Y. Kim, S. Park, G. Khang, D. Lee, Dual acid-responsive micelle-forming anticancer polymers as new anticancer therapeutics, Adv. Funct. Mater. 23 (40) (2013) 5091–5097.
[192] R.K. Kankala, C.-G. Liu, A.-Z. Chen, S.-B. Wang, P.-Y. Xu, L.K. Mende, C.-L. Liu, C.-H. Lee, Y.-F. Hu, Overcoming multidrug resistance through the synergistic effects of hierarchical pH-sensitive, ROS-generating nanoreactors, ACS Biomater. Sci. Eng. 3 (10) (2017) 2431–2442.
[193] Y. Dai, Z. Yang, S. Cheng, Z. Wang, R. Zhang, G. Zhu, Z. Wang, B.C. Yung, R. Tian, O. Jacobson, Toxic reactive oxygen species enhanced synergistic combination therapy by self-assembled metal-phenolic network nanoparticles, Adv. Mater. 30 (8) (2018) 1704877.
[194] A.A. Karyakin, Advances of Prussian blue and its analogues in (bio) sensors, Curr. Opin. Electrochem. 5 (1) (2017) 92–98.
[195] P. Huang, X. Qian, Y. Chen, L. Yu, H. Lin, L. Wang, Y. Zhu, J. Shi, Metalloporphyrin-encapsulated biodegradable nanosystems for highly efficient magnetic resonance imaging-guided sonodynamic cancer therapy, J. Am. Chem. Soc. 139 (3) (2017) 1275–1284.
[196] X. Wang, X. Zhong, L. Bai, J. Xu, F. Gong, Z. Dong, Z. Yang, Z. Zeng, Z. Liu, L. Cheng, Ultrafine titanium monoxide (TiO1+ x) nanorods for enhanced sonodynamic therapy, J. Am. Chem. Soc. 142 (14) (2020) 6527–6537.
[197] X. Cui, X. Han, L. Yu, B. Zhang, Y. Chen, Intrinsic chemistry and design principle of ultrasound-responsive nanomedicine, Nano Today 28 (2019) 100773.
[198] K. Lin, Z. Lin, Y. Li, Y. Zheng, D. Zhang, Ultrasound-induced reactive oxygen species generation and mitochondria-specific damage by sonodynamic agent/metal ion-doped mesoporous silica, RSC Adv. 9 (68) (2019) 39924–39931.
[199] I. Rosenthal, J.Z. Sostaric, P. Riesz, Sonodynamic therapy—a review of the synergistic effects of drugs and ultrasound, Ultrason. Sonochem. 11 (6) (2004) 349–363.
[200] Y. Zhao, B.-Q. Chen, R.K. Kankala, S.-B. Wang, A.-Z. Chen, Recent advances in combination of copper chalcogenide-based photothermal and reactive oxygen species-related therapies, ACS Biomater. Sci. Eng. 6 (9) (2020) 4799–4815.
[201] Y. Cao, T. Wu, W. Dai, H. Dong, X. Zhang, TiO2 nanosheets with the Au nanocrystal-decorated edge for mitochondria-targeting enhanced sonodynamic therapy, Chem. Mater. 31 (21) (2019) 9105–9114.
[202] W. Yue, L. Chen, L. Yu, B. Zhou, H. Yin, W. Ren, C. Liu, L. Guo, Y. Zhang, L. Sun, Checkpoint blockade and nanosonosensitizer-augmented noninvasive sonodynamic therapy combination reduces tumour growth and metastases in mice, Nat. Commun. 10 (1) (2019) 1–15.

[203] D. Costley, C. Mc Ewan, C. Fowley, A.P. McHale, J. Atchison, N. Nomikou, J.F. Callan, Treating cancer with sonodynamic therapy: a review, Int. J. Hyperther. 31 (2) (2015) 107–117.
[204] X.-Y. Dong, J.-T. Cheng, Y.-F. Zhang, Z.-L. Li, T.-Y. Zhan, J.-J. Chen, F.-L. Wang, N.-Y. Yang, L. Ye, Q.-S. Gu, Copper-catalyzed asymmetric radical 1, 2-carboalkynylation of alkenes with alkyl halides and terminal alkynes, J. Am. Chem. Soc. 142 (20) (2020) 9501–9509.
[205] G. Lan, K. Ni, S.S. Veroneau, X. Feng, G.T. Nash, T. Luo, Z. Xu, W. Lin, Titanium-based nanoscale metal–organic framework for type I photodynamic therapy, J. Am. Chem. Soc. 141 (10) (2019) 4204–4208.
[206] V.N. Nguyen, Y. Yim, S. Kim, B. Ryu, K. Swamy, G. Kim, N. Kwon, C.Y. Kim, S. Park, J. Yoon, Molecular design of highly efficient heavy-atom-free triplet BODIPY derivatives for photodynamic therapy and bioimaging, Angew. Chem. Int. Ed. 59 (23) (2020) 8957–8962.
[207] X. Wang, X. Zhong, J. Li, Z. Liu, L. Cheng, Inorganic nanomaterials with rapid clearance for biomedical applications, Chem. Soc. Rev. 50 (15) (2021) 8669–8742.
[208] E. Paszko, C. Ehrhardt, M.O. Senge, D.P. Kelleher, J.V. Reynolds, Nanodrug applications in photodynamic therapy, Photodiagnosis Photodyn. Ther. 8 (1) (2011) 14–29.
[209] D. Bechet, P. Couleaud, C. Frochot, M.-L. Viriot, F. Guillemin, M. Barberi-Heyob, Nanoparticles as vehicles for delivery of photodynamic therapy agents, Trends Biotechnol. 26 (11) (2008) 612–621.
[210] G. Lan, K. Ni, Z. Xu, S.S. Veroneau, Y. Song, W. Lin, Nanoscale metal–organic framework overcomes hypoxia for photodynamic therapy primed cancer immunotherapy, J. Am. Chem. Soc. 140 (17) (2018) 5670–5673.
[211] C. Yao, W. Wang, P. Wang, M. Zhao, X. Li, F. Zhang, Near-infrared upconversion mesoporous cerium oxide hollow biophotocatalyst for concurrent pH-/H2O2-responsive O2-evolving synergetic cancer therapy, Adv. Mater. 30 (7) (2018) 1704833.
[212] R.S. Riley, C.H. June, R. Langer, M.J. Mitchell, Delivery technologies for cancer immunotherapy, Nat. Rev. Drug Discov. 18 (3) (2019) 175–196.
[213] J. Nam, S. Son, K.S. Park, W. Zou, L.D. Shea, J.J. Moon, Cancer nanomedicine for combination cancer immunotherapy, Nat. Rev. Mater. 4 (6) (2019) 398–414.
[214] L. Rao, S.K. Zhao, C. Wen, R. Tian, L. Lin, B. Cai, Y. Sun, F. Kang, Z. Yang, L. He, Activating macrophage-mediated cancer immunotherapy by genetically edited nanoparticles, Adv. Mater. 32 (47) (2020) 2004853.
[215] Q. Fan, Z. Chen, C. Wang, Z. Liu, Toward biomaterials for enhancing immune checkpoint blockade therapy, Adv. Funct. Mater. 28 (37) (2018) 1802540.
[216] X. Duan, C. Chan, W. Lin, Nanoparticle-mediated immunogenic cell death enables and potentiates cancer immunotherapy, Angew. Chem. Int. Ed. 58 (3) (2019) 670–680.
[217] K. Lu, C. He, N. Guo, C. Chan, K. Ni, R.R. Weichselbaum, W. Lin, Chlorin-based nanoscale metal–organic framework systemically rejects colorectal cancers via synergistic photodynamic therapy and checkpoint blockade immunotherapy, J. Am. Chem. Soc. 138 (38) (2016) 12502–12510.
[218] C. Xu, K. Pu, Second near-infrared photothermal materials for combinational nanotheranostics, Chem. Soc. Rev. (2021).
[219] J. Michot, C. Bigenwald, S. Champiat, M. Collins, F. Carbonnel, S. Postel-Vinay, A. Berdelou, A. Varga, R. Bahleda, A. Hollebecque, Immune-related adverse events with immune checkpoint blockade: a comprehensive review, Eur. J. Cancer 54 (2016) 139–148.
[220] Z. Zhou, J. Song, L. Nie, X. Chen, Reactive oxygen species generating systems meeting challenges of photodynamic cancer therapy, Chem. Soc. Rev. 45 (23) (2016) 6597–6626.
[221] Q. Fu, Z. Li, J. Ye, Z. Li, F. Fu, S.-L. Lin, C.A. Chang, H. Yang, J. Song, Magnetic targeted near-infrared II PA/MR imaging guided photothermal therapy to trigger cancer immunotherapy, Theranostics 10 (11) (2020) 4997–5010.
[222] L.-H. Fu, C. Qi, J. Lin, P. Huang, Catalytic chemistry of glucose oxidase in cancer diagnosis and treatment, Chem. Soc. Rev. 47 (17) (2018) 6454–6472.
[223] J. Marx, A boost for tumor starvation, Science 301 (5632) (2003) 452–454.
[224] N.C. Denko, Hypoxia, HIF1 and glucose metabolism in the solid tumour, Nat. Rev. Cancer 8 (9) (2008) 705–713.
[225] H. Zhu, Y. Li, Z. Ming, W. Liu, Glucose oxidase-mediated tumor starvation therapy combined with photothermal therapy for colon cancer, Biomater. Sci. 9 (2021) 5577–5587.
[226] J. Li, Y. Li, Y. Wang, W. Ke, W. Chen, W. Wang, Z. Ge, Polymer prodrug-based nanoreactors activated by tumor acidity for orchestrated oxidation/chemotherapy, Nano Lett. 17 (11) (2017) 6983–6990.
[227] T. He, H. Xu, Y. Zhang, S. Yi, R. Cui, S. Xing, C. Wei, J. Lin, P. Huang, Glucose oxidase-instructed traceable self-oxygenation/hyperthermia dually enhanced cancer starvation therapy, Theranostics 10 (4) (2020) 1544–1554.
[228] W. Fan, N. Lu, P. Huang, Y. Liu, Z. Yang, S. Wang, G. Yu, Y. Liu, J. Hu, Q. He, Glucose-responsive sequential generation of hydrogen peroxide and nitric oxide for synergistic cancer starving-like/gas therapy, Angew. Chem. 129 (5) (2017) 1249–1253.
[229] R. Zhang, L. Zhang, H. Ran, P. Li, J. Huang, M. Tan, Y. Yang, Z. Wang, A mitochondria-targeted anticancer nanoplatform with deep penetration for enhanced synergistic sonodynamic and starvation therapy, Biomater. Sci. 8 (16) (2020) 4581–4594.
[230] S.-Y. Li, H. Cheng, B.-R. Xie, W.-X. Qiu, J.-Y. Zeng, C.-X. Li, S.-S. Wan, L. Zhang, W.-L. Liu, X.-Z. Zhang, Cancer cell membrane camouflaged cascade bioreactor for cancer targeted starvation and photodynamic therapy, ACS Nano 11 (7) (2017) 7006–7018.
[231] L. Zhang, S.-S. Wan, C.-X. Li, L. Xu, H. Cheng, X.-Z. Zhang, An adenosine triphosphate-responsive autocatalytic fenton nanoparticle for tumor ablation with self-supplied H2O2 and acceleration of Fe (iii)/Fe (ii) conversion, Nano Lett. 18 (12) (2018) 7609–7618.
[232] J. Chen, L. Mohrhusen, G. Ali, S. Li, K.Y. Chung, K. Al-Shamery, P.S. Lee, Electrochemical mechanism investigation of Cu2MoS4 hollow nanospheres for fast and stable sodium ion storage, Adv. Funct. Mater. 29 (7) (2019) 1807753.